Chapter 3
Ceramic Powder Synthesis

3.1 Introduction

The processing of any ceramics is started from their precursor powders, which are then consolidated into green bodies, followed by sintering at high temperature [1–5]. Of course, there are various other steps that also play significant roles in determining the performance of the final ceramic products. As a result, properties of the powder pose a direct effect on microstructure and thus performance of the final ceramics. The properties of a powder are closely related to the way the powder is synthesized. According to properties and applications, ceramics can be classified into traditional ceramics and advanced ceramics. The functionalities of traditional ceramics are less sensitive to chemical compositions, which usually consist of multiple components, with clays as the main component and various additives [6]. In contrast, the properties and performances of advanced ceramics are very sensitive to their compositions and microstructures. Therefore, they must meet very specific requirements in terms of properties, compositions, and microstructures. Transparent ceramics belong to the category of advanced ceramics. As stated previously, special carefulness is necessary in processing of transparent ceramics, because optical properties are even more sensitive than other properties.

For good control the chemical composition and microstructure of transparent ceramics, the availability of high quality starting powders is a pre-requirement. For starting powders, important characteristics include grain/particle size, size distribution, shape, morphology, degree and state of agglomeration, chemical composition, phase composition, and purity. Physical and chemical properties of surface of the particles also play an important role. Both the powder consolidation and the microstructure development are influenced by the size, size distribution, shape, and state of agglomeration. The size of particle/grain has a specific effect sintering. It is well known that the densification rate increases with decreasing particle/grain size.

According to sizes and size distributions, powders can be classified into two types: (i) polydispersed and (ii) monodispersed powder [7–15]. Polydisperse means

L.B. Kong et al., *Transparent Ceramics*, Topics in Mining,
Metallurgy and Materials Engineering, DOI 10.1007/978-3-319-18956-7_3

that the powder has a wide particle size distribution, while a monodispersed powder has one particle size, but most likely, it means a very narrow size distribution. Polydispersed powders could offer high packing density of green bodies, while there is a negative effect on densification behavior and microstructure development during the sintering. This is because large grains grow much faster by consuming smaller grains surrounding them. In this respect, homogeneous packing of powders with a narrow size distribution is preferred, to from the control of microstructure point of view. Additionally, powders consisting of spherical or near-spherical particles are desirable to have a uniform packing. However, until now, synthesis of monodispersed fine powders is still a challenge of ceramic processing [8, 16–23].

Another challenge of powder processing is the addressing of agglomeration [24–26]. The direct consequence of the presence of agglomeration is the heterogeneity of the packed green bodies, which will result in a phenomenon known as differential sintering [27, 28]. Differential sintering means that different regions of the bodies have different densification behaviors, due to the inhomogeneity. In this case, the final ceramics will likely to have large pores and crack-like voids. Therefore, agglomeration must be avoided in order to fabricate ceramics with high density and homogeneous microstructure. Two types of agglomerations have been observed in ceramic powders: (i) soft agglomerates and (ii) hard agglomerates. Soft agglomerates are made of the particles due to the weak van der Waals forces, while hard agglomerates are formed by chemical bonding. As a result, the negative effect of soft agglomeration is much less than that of hard agglomeration.

Other factors that have significant effects on sintering of a powder include surface characteristics, incomplete chemical reactions, polymorphic phase transformations, and so on. Surface properties affect the dispersion behavior of a powder, thus influencing its sintering efficiency. The unreacted components will react during the sintering, which usually leads to inhomogeneity. Phase transformation could have serious negative effect on microstructure.

In summary, an ideal ceramic starting powder should a small size, e.g., <1 μm or at the scale of nm, a narrow particle or grain size distribution, i.e., monodisperse or near monodisperse, a spherical or near-spherical particle/grain shape, no agglomeration or only soft agglomeration, completed chemical reaction, single phase and high purity. To achieve this, it is important to select the synthesis methods.

Various methods have been developed to synthesize ceramic powders, including physical and chemical methods [29, 30]. The simplest physical method is mechanical milling, in which mechanical action is used to refine the powders [31–33]. Other physical methods include vacuum vapor condensation (VVC) and physical vapor deposition (PVD), and so on. Milling is a general step in the preparation of ceramic powders for the purpose of mixing, if refining is not expected. Physical condensation or deposition is not suitable to produce powders with large quantities. In comparison, chemical methods, such as solid-state reaction and various wet-chemical solution routes are the most widely employed to fabricate advanced ceramics in general and transparent ceramics in particular [34, 35]. In

solid-state reaction methods, the use of high-energy milling in recent years has shown certain advantages in reducing the phase formation temperatures of ceramic materials, because transparent ceramics usually have relatively high reaction temperatures [36, 37].

3.2 Synthesis of Precursor Powders

3.2.1 Solid-State Reaction Methods

There are three types of solid-state reaction: (i) chemical decomposition, (ii) chemical reaction between solids, and (iii) chemical reduction. The first two reactions will be introduced, while the third one is commonly used for nonoxides which thus are not included.

Chemical decomposition is usually observed in solid reactions, such as carbonate, hydroxides, nitrate, acetate, oxalates, alkoxides and so on, when they are heated at a certain temperature. The decomposition leads to the formation of a new solid product, together with one or more gaseous phases, which is usually used to produce powders of simple oxides in most cases and complex oxides sometimes. Although this method has not been widely reported for the synthesis of transparent ceramic powders, it could be a potential technique for such a purpose, due to its various advantages, such as simple processing, inexpensive raw materials, and capability of large scale production. In fact, the calcination step involved in most wet-chemical processing routes, especially chemical precipitation or co-precipitation, is chemical decomposition, either from carbonates or hydroxides, as discussed later.

A representative example of chemical decomposition is the formation of magnesia (MgO) from magnesium carbonate ($MgCO_3$). When it is heated, magnesium carbonate decomposes into magnesium oxide and carbon dioxide gas, with reaction equation as follows:

$$MgCO_3\,(s) \rightarrow MgO\,(s) + CO_2\,(g). \tag{3.1}$$

Chemical reactions between solids are used to synthesize mixed powders or complex oxides. The reactants are usually simple oxides, carbonates, nitrates, sulfates, oxalates or acetates, which are mixed according to a target compound with a given stoichiometric composition. An example is the reaction between magnesia and alumina to form magnesium aluminate or spinel, with the following reaction equation:

$$MgO\,(s) + Al_2O_3\,(s) \rightarrow MgAl_2O_4\,(s). \tag{3.2}$$

These methods, involving decomposition of solids and then chemical reaction between solids, are referred to as calcination or pre-sintering in ceramic processing.

3.2.1.1 Decomposition Methods

The principles, kinetics and chemistry of decomposition reactions, such as carbonates and hydroxides, have been extensively studied in the open literature [38–42]. Basic thermodynamics, reaction kinetics and mechanism, as well as closely related process parameters regarding the production of powders, will be elaborated in this subsection.

According to thermodynamics, the decomposition of $MgCO_3$ that is defined by Eq. (3.1), is a strongly endothermic reaction, since ΔH_R^0 is positive, which is similar to most decomposition reactions [43–45]. Therefore, the decomposition is only sustained when the reactant is constantly heated. In thermodynamics, the Gibbs free energy change of a chemical reaction is given by:

$$\Delta G_R = \Delta G_R^0 + RT \ln K, \tag{3.3}$$

where ΔG_R^0 is the free energy change for the reaction when the reactants are in standard state, R is the gas constant, T is the absolute temperature, and K is the equilibrium constant of the reaction. For the reaction defined by Eq. (3.1), there is:

$$K = \frac{a_{MgO} a_{CO_2}}{a_{MgCO_3}} = p_{CO_2}, \tag{3.4}$$

where a_{MgO} and a_{MgCO_3} are the activities of pure solids, MgO and $MgCO_3$, respectively, which can be treated as unity, while a_{CO_2} is the activity of CO_2, which is actually the partial pressure of the gas. Therefore, at equilibrium state, $\Delta G_R = 0$, by combining Eqs. (3.3) and (3.4), there is:

$$\Delta G_R^0 = -RT \ln p_{CO_2}. \tag{3.5}$$

The standard Gibbs free energies for the decomposition of various carbonates and hydroxides, as a function of temperature, as well as the equilibrium partial pressure of the gas for each of the reactions, have been well documented as a database, which can be found in the open literature [46].

In thermodynamics, as the partial pressure of the gaseous product above the solid of a compound is equal to the partial pressure of the gas in the surrounding atmosphere, the compound will become unstable, when it is heated in air. This unstable temperature can be estimated. Thermodynamics predict that the partial pressure of the gas products of many salts, such as acetates, sulfates, oxalates and nitrates, is almost zero, which means that they are unstable at room temperature. However, the fact is that these compounds are stable up to quite high temperatures. Therefore, the decomposition of these compounds is controlled by kinetics, instead of thermodynamics [43–45].

Kinetic studies have been conducted to elucidate the reaction mechanisms and identify the influences of process parameters on the decomposition reactions, such as reaction temperature, particle size of the compound, quantity of the reactant and

surrounding environment. These studies can be carried out either isothermally or at a fixed heating rate. Under isothermal conditions, it is impossible to maintain a constant temperature, because heating the sample to a given temperature requires an infinite time. In spite of this, it is easier to analyze the kinetics of isothermal decompositions.

Progress of the reaction is usually measured by monitoring the weight loss, which is plotted as the fraction of the reactant that has decomposed, as a function of time t, defined as:

$$\alpha = \frac{\Delta W}{\Delta W_{\max}}, \tag{3.6}$$

where W and $W_{\max}$ are the weight loss at time t and the maximum weight loss after the decomposition reaction is entirely completed, respectively.

Although no general theory has been available to describe the decomposition reactions, a general trend can often be observed. At the initial stage of reaction, decomposition of impurities or unstable superficial items most likely occurs. It then enters an induction period, which is then quickly terminated, due to the development of stable nuclei. After that, the nuclei starts to grow at an accelerated rate, together with further nucleation in some cases. After that, the reaction reaches the maximum rate. With the progress of the reaction, the expansion of nuclei gradually slows down and eventually stops, indicating the starting of a decay period, which continues until the reaction is completed.

Because the molar volume of the solid product is usually smaller than that of the reactant, the product is present as a porous layer covering the nonporous core of the reactant, as shown schematically for the decomposition of $CaCO_3$ in Fig. 3.1 [47]. Therefore, it is a heterogeneous reaction occurring at a sharply defined interface. In this case, there are three processes: (i) reaction at the interface between the reactant and the solid product, (ii) heat transfer to the reaction surface from outside of the particle and (iii) gas diffusion out or permeation from the reaction surface through the porous layer of the product. Any of them could be the controlling factor of kinetics of the decomposition reaction. Generally, it is assumed that the interface moves inward at a constant rate. Therefore, for a spherical reactant with an initial radius r_0, the radius of the unreacted core at time t is given by:

$$r = r_0 - Kt, \tag{3.7}$$

where K is a constant.

One of the parameters that characterize the kinetics of chemical reactions is known as reaction orders. In the simplest case, a reactant A decomposes to a product (P), the reaction equation is written as:

$$A \rightarrow P. \tag{3.8}$$

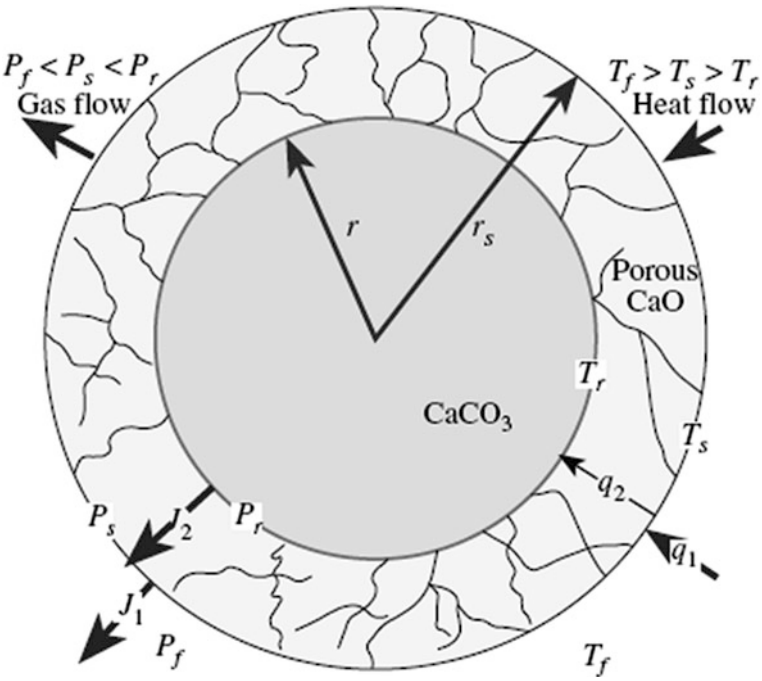

Fig. 3.1 Schematic of the decomposition of calcium carbonate. Reproduced with permission from [47]. Copyright © 2007, Springer

The rate of the reaction can be written as:

$$-\frac{\mathrm{d}C}{\mathrm{d}t} = KC^{\beta}, \tag{3.9}$$

where C is the concentration of the reactant A at time t, K is called the reaction rate constant, and β is an exponent that defines the order of the reaction. The reaction is characterized as first order if $\beta = 1$, second order if $\beta = 2$, and third order if $\beta = 3$. In practice, very high orders of reactions are rarely observed. The orders can be zero or factions.

Several parameters have their influences on the rate of decomposition and the characteristics of the powders produced by the decomposition reaction. These parameters include chemical properties of the reactants, initial particle size and size distribution of the reactants, atmospheric conditions, reaction temperature, and time duration. According to the Arrhenius relation, the rate constant K in the kinetic equation is given by:

$$K = A \exp\left[\frac{-Q}{RT}\right], \tag{3.10}$$

where A is a constant which is known as the pre-exponential coefficient or frequency factor, Q is the activation energy, R is the gas constant, and T is the absolute temperature.

Microstructure and morphology of the solid product particles are also affected by the decomposition conditions. Therefore, by controlling the decomposition conditions, it is possible to obtain product powders with fine particles and narrow particle size distribution [48]. The principles of the decomposition method are applicable, when precipitation or co-precipitation methods are used to synthesize oxide powders, where hydroxides or carbonates are formed as precipitates. Decomposition of the hydroxides and carbonates results in oxide powders.

3.2.1.2 Chemical Reaction Methods

The simplest reaction occurs between two solid phases, A and B, to form a solid solution C. A and B are usually polycrystalline compounds. Once the reaction is started, A and B will be separated by the product C. Further reaction is facilitated by the transport of atoms, ions or molecules, which are governed by several possible mechanisms through the phase boundaries and the products of the reaction. Single crystals are generally used to study such reaction mechanisms, because of the simple geometry and the clearly defined boundaries, as shown in Fig. 3.2 [47].

The formation reaction of spinel, $AO + B_2O_3 = AB_2O_4$, is used as an example. Figure 3.3 shows some of the most possible mechanisms involved in the reaction [47]. The first type of mechanism is shown in Fig. 3.3a, b, in which O_2 molecules are transported through the gaseous phase, while the electroneutrality is maintained by electron transport through the layer of the product. In mechanism (ii), i.e., Figure 3.3c, counterdiffusion of the cations with oxygen ions takes place, which has remained stationary. Mechanisms (iii) are shown in Fig. 3.3d, e, in which O_2 ions diffuse through the product layer. Due to their intrinsic properties, the diffusion coefficients of different ions could be significantly different. In spinels, the diffusion of large-sized O_2 ions is much slower than that of cations. As a result, the mechanisms in Fig. 3.3d, e are not dominant. Futhermore, if the phase boundaries have ideal contacts, the transport of O_2 molecules is very slow, so that it is not necessary to consider the mechanisms in Fig. 3.3a, b.

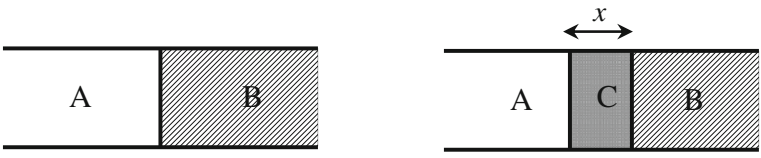

Fig. 3.2 Schematic of solid-state reaction between two single crystals (*A* and *B*). Reproduced with permission from [47]. Copyright © 2007, Springer

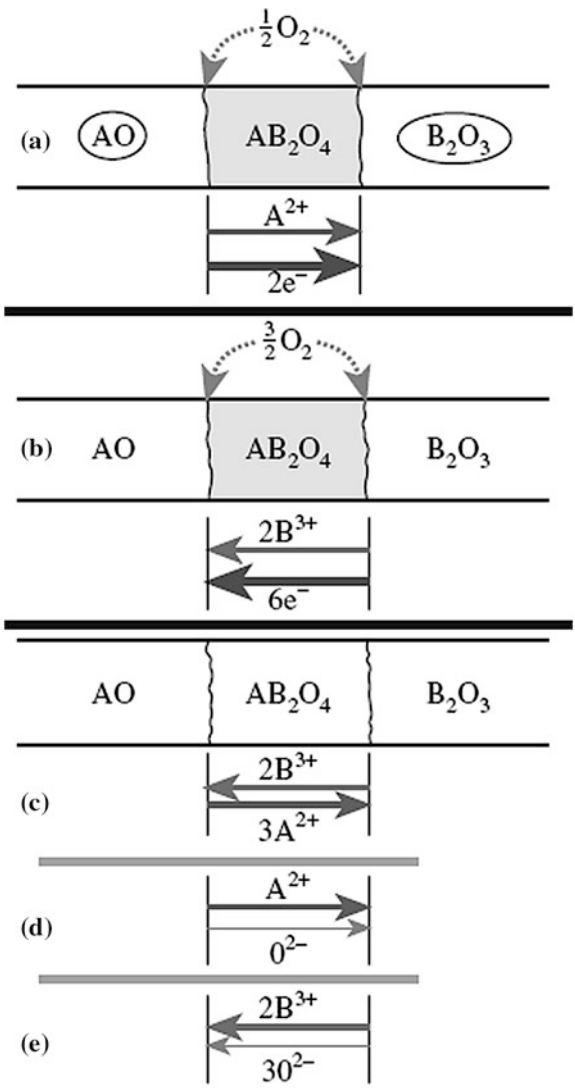

Fig. 3.3 Reaction mechanisms and corresponding net phase boundary reactions for the spinel formation reaction AO B_2O_3 = AB_2O_4. Reproduced with permission from [47]. Copyright © 2007, Springer

In this case, the most likely mechanism is the counterdiffusion of cations, i.e., the mechanism of Fig. 3.3c, where the electroneutrality is maintained by the coupling of flux of the cations. When the formation rate of the product is controlled by diffusion through the layer of the product, the thickness of the product layer will follow a parabolic growth law, which is given by:

$$x^2 = Kt, \tag{3.11}$$

where K is a rate constant that can be described by the Arrhenius equation.

Because there are several parameters that should be taken into account to describe the reaction kinetics of reactions in the form of powder mixture, the analysis could be quite complicated. As a result, various assumptions have been made to simplify the analysis models, in order to derive appropriate kinetic equations. For isothermal reactions, it is generally assumed that the particles of reactant A are equal-sized spheres, which are embedded in a quasi-continuous medium of reactant B, so that the reaction product is formed coherently and uniformly on the surface of the A particles [49, 50]. In this case, the volume of the unreacted components at time t is given by:

$$V = \frac{4}{3}\pi(r - y)^3, \tag{3.12}$$

where r is the initial radius of the spherical particles of reactant A and y is the thickness of the product layer. The volume of the unreacted phases can also be expressed as:

$$V = \frac{4}{3}\pi r^3(1 - \alpha), \tag{3.13}$$

where α is the fraction of the volume of the reactants that has already consumed due to the reaction. Combining Eqs. (3.12) and (3.13) yields:

$$y = r[1 - (1 - \alpha)]^{1/3}. \tag{3.14}$$

If it is assumed that y follows the parabolic relationship given by Eq. (3.11), the rate of the reaction becomes:

$$[1 - (1 - \alpha)^{1/3}]^2 = \frac{Kt}{r^2}. \tag{3.15}$$

This is known as Jander equation, which has two oversimplifications that limit its applicability and the capability to predict the rates of most chemical reactions. Firstly, the parabolic growth law for the thickness of the product layer is only valid for one-dimensional reaction across a planar boundary, but not sufficient for the reactions involving spherical particles. In other words, this assumption is only valid for the initial stage of the reaction when $y \ll r$. Second, the changes in molar volumes of the reactants and the products are not taken into account. To address this problem, a more comprehensive equation should be used, which is [51, 52]:

$$[1 + (Z - 1)\alpha]^{2/3} + (Z - 1)(1 - \alpha)^{2/3} = Z + (1 - Z)\frac{Kt}{r^2}, \tag{3.16}$$

where Z is the volume of the product formed from unit volume of the reactant A. This equation is known as the Carter equation, which is applicable to predict the formation of complex oxides.

In practice, the reaction rate decreases with increasing particle size of the reactants due to the increase in the average diffusion distance. According to the Arrhenius relation, the reaction rate increases with increasing temperature. Also, the homogeneity of mixing is an important parameter that determines reaction rate of a reaction involving powder mixtures. This is because it influences the diffusion distance between the reactants and the number of contacts between the reactant particles. It also plays a significant role in ensuring the homogeneity and single-phase product powders. The most effective strategy that can be used to increase the homogeneity of a powder mixture is mechanical milling, which will be discussed in the following subsection.

Solid-state reaction method has been used to fabricate various transparent ceramics, including YAG, LuAG, $MgAl_2O_4$, doped simple oxides and AlON [53–69]. Usually, commercial powders, most likely oxides and sometimes carbonates or hydroxides, are directly used without any special treatment. In some studies, calcination or pre-sintering step is used to form the compounds of interest. Sometimes, this pre-sintering step can be skipped. In this case, it is also called as reactive sintering, simply because the reaction will take place during the sintering process.

The first YAG transparent ceramics for laser applications was made by using solid-state reaction [53]. However, in this report, Al_2O_3 and Y_2O_3 were pre-synthesized through alkoxide precipitation and pyrolysis of $Y_2(OH)Cl_5 \cdot nH_2O$, respectively. The two powders, with a particle size of <2 μm, were mixed according to the composition of YAG, through the following reaction:

$$3Y_2O_3 + 5Al_2O_3 \rightarrow 2Y_3Al_5O_{12}. \tag{3.17}$$

A similar approach has been reported to synthesize YAG by using pre-synthesized Y_2O_3 [54]. Yttrium nitrate was used as the source of yttrium and aqueous ammonia was used as precipitant. Fine and dendritic precipitate was obtained by adding 0.5 % ammonium sulfate into the precipitation solution. High-purity and low-agglomerated Y_2O_3 powder with spherical particles of about 60 nm in diameter was prepared by calcinating the precipitate at 1100 °C. The highly reactive Y_2O_3 powder was mixed with Al_2O_3 powder to form YAG powder after calination at relatively low temperature. The YAG powder could be sintered to transparent ceramics in vacuum at 1700 °C.

A solid-state reaction method by using commercial powers has been employed to fabricate ytterbium and chromium co-doped YAG (Yb,Cr:YAG) transparent ceramics [58]. CaO and TEOS were used as charge counter element and sintering aid, respectively. High purity Y_2O_3, Al_2O_3, Cr_2O_3, and Yb_2O_3 commercial powders were used as starting materials. CaO provided Ca^{2+} for charge balance when Cr^{3+} was oxidized to Cr^{4+}. The starting powders with a composition of 5 at% Yb, 0.025 at% Cr:YAG were mixed by using ball milling with Ø6 mm ZrO_2 balls in anhydrous alcohol for 10 h. The content of sintering aid was 0.5 wt% tetraethyl orthosilicate (TEOS). Cold isostatic pressure of 200 MPa was applied before sintering. Highly transparent Yb,Cr:YAG ceramics were developed after sintering at 1770 °C for 10 h in vacuum, followed by annealing at 1450 °C for 20 h in air. No

calcination or pre-sintering step was involved in this study, so that is reactive sintering, as mentioned earlier.

It has been found that pretreatment could play a significant role in promoting the efficiency of sintering for the fabrication of transparent ceramics. One example has been demonstrated when Y_2O_3 was used to react with Al_2O_3 to form YAG [70]. Commercially available high-purity α-Al_2O_3 (99.98 %), Y_2O_3 (99.99 %) and Nd_2O_3 powders (99.99 %) were used as starting materials. All the raw powders were baked at 200 °C for 24 h and stored in a dry box to prevent water absorption. In addition, the commercial Y_2O_3 powder was calcined in oxygen atmosphere at temperatures of 800, 1000, and 1200 °C for 2 h.

All the untreated and the pretreated Y_2O_3 powders were used to synthesize $Nd_{0.03}Y_{2.97}Al_5O_{12}$. The powder mixtures were ball milled for 12 h with high purity Al_2O_3 balls of 10 mm in diameter in ethanol. 0.1 wt% MgO (99.998 %) and 0.5 wt% tetraethyl orthosilicate (TEOS, 99.99 %) were used as sintering aids. The milled slurries were dried at 80 °C for 2 h. The dried powder mixtures were calcined at 600 °C for 4 h to remove the organic components. Then, the calcined mixtures were dry pressed under 100 MPa into Φ35 mm pellets, followed by the application of cold isostatic pressing (CIP) at pressure of 250 MPa. All the samples were finally sintered at 1745 °C for 50 h in vacuum of 10^{-3} Pa. The sintered ceramics were annealed at 1450 °C for 10 h in air to eliminate the oxygen vacancies.

Figure 3.4 shows SEM images of the untreated commercial Y_2O_3 and α-Al_2O_3 powders. The Y_2O_3 powder had agglomerations, consisting of primary particles with a diameter of about 50 nm. The nanoparticles were aggregated to form secondary particles with sizes in the range of 3–10 μm, as shown in Fig. 3.4a. In addition, the Y_2O_3 powder exhibited a microstructure that was similar to that of nanoceramics. Natural surface of the Y_2O_3 powder, as shown in Fig. 3.4b, had a dense feature formed by the primary particles due to hard aggregates. On the fractured surface, some internal pores were observed within the secondary particles, as illustrated in Fig. 3.4c. The sizes of the primary and secondary particles, as well as the internal porosity, determined particle size distribution and specific surface of the powder, which thus influenced the sintering behavior of the powder and optical properties of the final ceramics. Comparatively, the α-Al_2O_3 powder was not aggregated, with an average particle size of ~260 nm, as shown in Fig. 3.4d.

Figure 3.5 shows SEM images of the untreated Y_2O_3 powder and the powders pretreated at different temperatures in oxygen for 2 h. By comparing Fig. 3.5a, b, it is found that the size of the primary particle was increased from 53 to 62 nm, after treating at 800 °C, and then to 126 nm after calcining at 1000 °C (Fig. 3.5c). 1200 °C was too high for the powder, because a significant grain growth was observed and natural surface of the powder became more rigid, as demonstrated in Fig. 3.5d.

Figure 3.6 shows a schematic illustration of the green body derived from the Y_2O_3 and Al_2O_3 powder mixture after ball milling. It has been accepted that green bodies formed by dry pressing and cold isostatic pressing have a microstructure with two types of pores, i.e., (i) interparticles pores which coexist with (ii) intra-agglomerate pores within the agglomerated Y_2O_3 powders. Because the sintering driving force and shrinkage inside the Y_2O_3 agglomerates were different from those

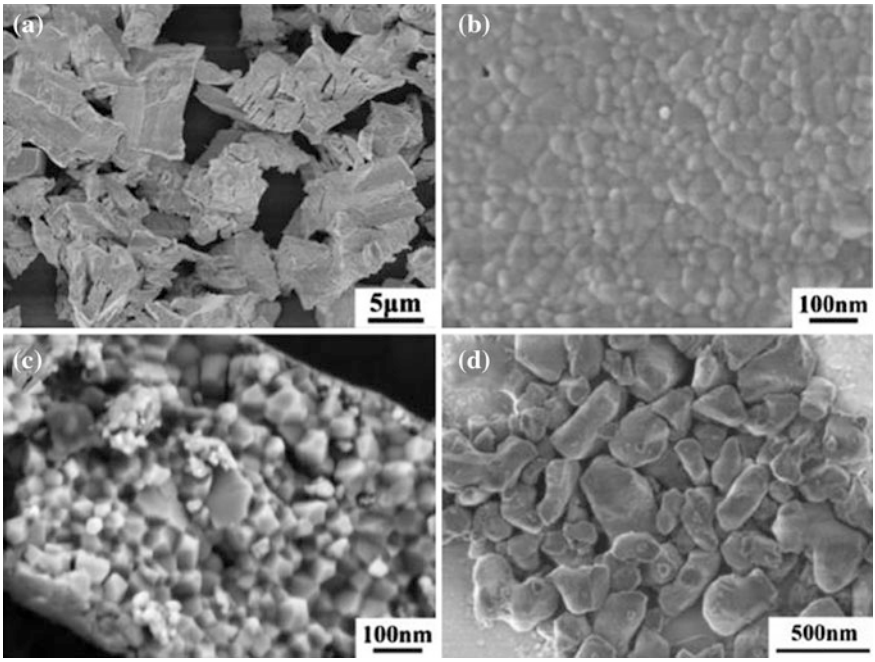

Fig. 3.4 SEM images of the raw powders: **a** untreated commercial Y_2O_3 powder, **b** natural surface of the untreated Y_2O_3 powder, **c** fractured surface of the untreated Y_2O_3 powder and **d** α-Al_2O_3 powder. Reproduced with permission from [70]. Copyright © 2014, Elsevier

in between the agglomerates and the Al_2O_3 particles, the sintering property of the powder was sensitive to the degree of agglomerates of the Y_2O_3 powders. During the sintering, the elimination of the interparticles pores needed high temperature (>1700 °C). However, due to the high sinterability of the small Y_2O_3 particles, intra-agglomerate pores within the Y_2O_3 powders were easily closed and difficult to be eliminated in the subsequent densification process at such a high temperature (>1700 °C). Therefore, eliminating the intra-agglomerate pores within the Y_2O_3 powders became important. The pretreatment of the Y_2O_3 powders at a low temperature (<1200 °C) in oxygen was beneficial to the elimination of the intra-agglomerate pores. The optimum pretreatment temperature was 1000 °C, because at this temperature there was a synergistic effect of sinterability of the powders and the reduced porosity in green body. This result could be used as a reference, because different materials should have different optimized treatment temperatures.

Besides oxides, no-oxides have also been synthesized by using solid-state reaction method. For example, phase-pure and fine γ-AlON powders have been synthesized by using a combinational method of carbothermal reduction and solid-state reaction [69]. The combined method addressed the disadvantages of the respective individual method. Sucrose was used as the reducer instead of carbon

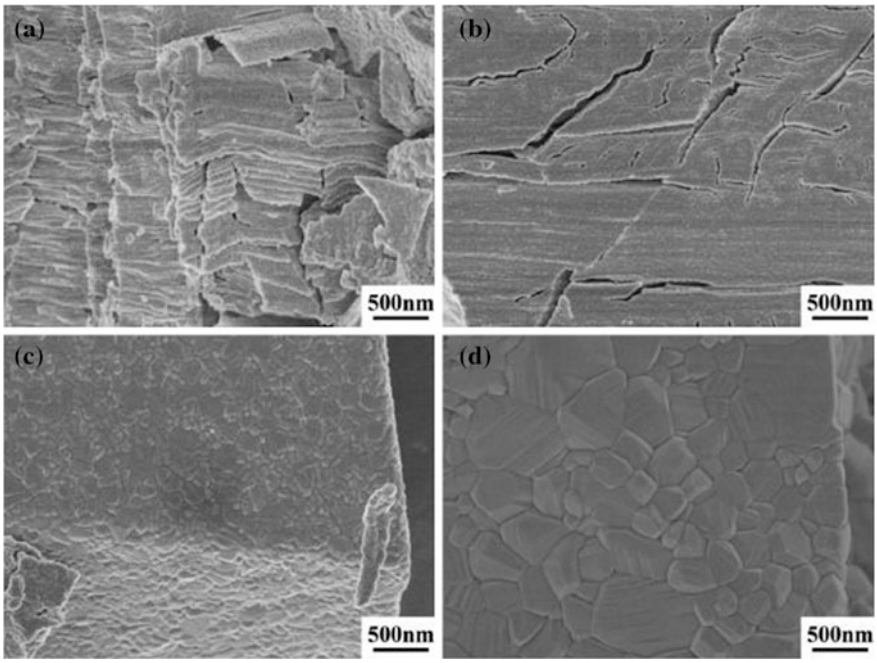

Fig. 3.5 SEM images of the Y_2O_3 powders pretreated at different temperatures for 2 h: **a** without pretreatment, **b** 800 °C, **c** 1000 °C, and **d** 1200 °C. Reproduced with permission from [70]. Copyright © 2014, Elsevier

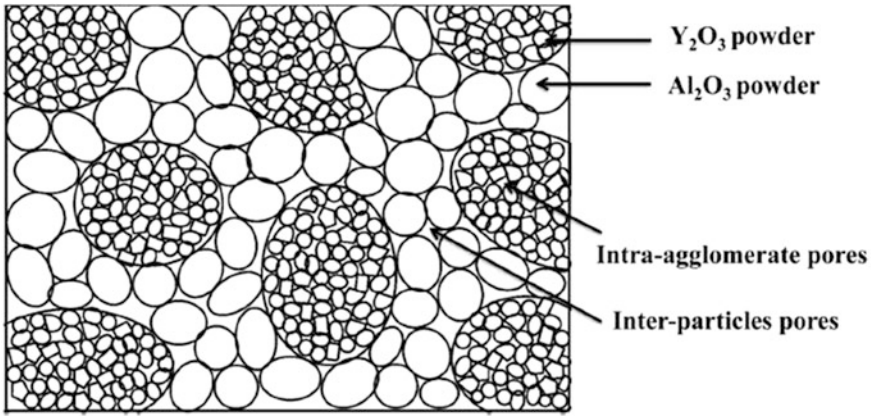

Fig. 3.6 Schematic illustration of the green body derived from the Y_2O_3 and Al_2O_3 powder mixture after ball milling. Reproduced with permission from [70]. Copyright © 2014, Elsevier

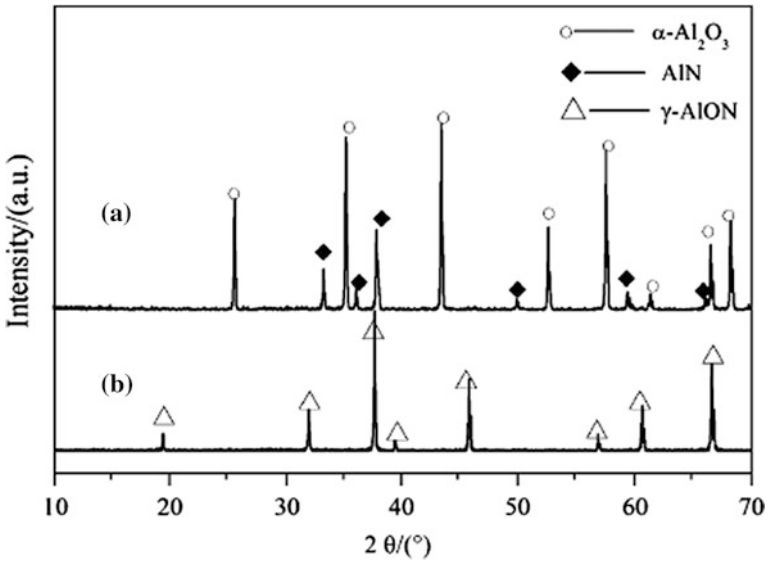

Fig. 3.7 XRD patterns of the **a** nitrided powders and **b** powders heated at 1750 °C for 4 h. Reproduced with permission from [69]. Copyright © 2010, John Wiley & Sons

black. Comparatively, sucrose was more effective in nitridation and hindering the agglomeration of powders.

Figure 3.7 shows XRD patterns of the samples after initial and final treatments [69]. After being heated at 1500 °C for 4 h, with sucrose as the reducer, partial γ-Al_2O_3 powder was nitridized into AlN and the rest was converted from γ to α phase, as shown in Fig. 3.7a. After the residual carbon has been removed, the resultant powder was gray in color, similar to that of commercial AlN powder, In contrast, if carbon black is used as the reducer, the resultant powder was brown owing to the serious carbon infiltration. Schematic diagrams for possible explanation are shown in Fig. 3.8. When sucrose was used as the reducer, Al_2O_3 powder was covered by a layer of carbon after being heated at 900 °C, as shown in Fig. 3.8a. The area for nitridation was maximized, so that nitridation was sufficient. However, if carbon black was used, the efficiency of nitridation was greatly reduced due to the poor contact between the carbon black particles and those of Al_2O_3 powder, as shown in Fig. 3.8b. Therefore, the nitridation was incomplete, thus leading to carbon infiltration.

3.2.1.3 Mechanochemical Synthesis

Mechanochemical synthesis means that chemical reactions that are usually triggered by heating or firing can be facilitated by applying mechanical actions. The most general mechanical action is milling. Various mills have been used to reduce

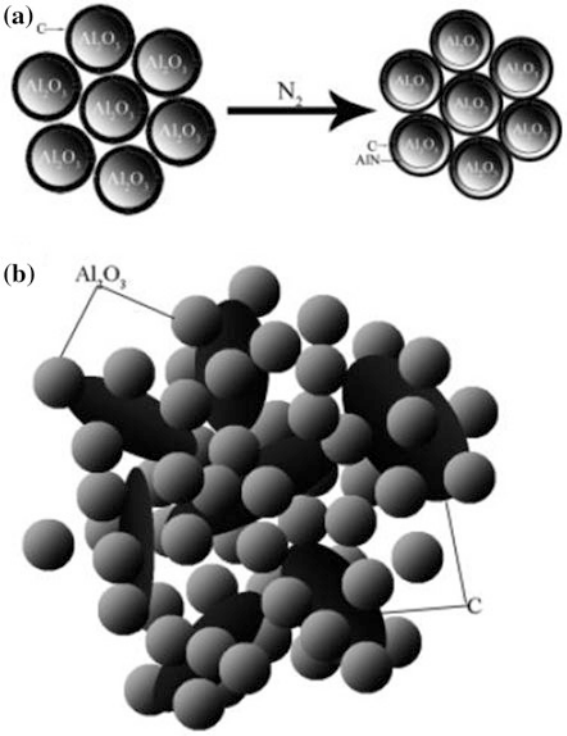

Fig. 3.8 Schematic diagrams for **a** the nitridation with sucrose as reducer and **b** the mixture of γ-Al_2O_3 and carbon black, respectively. Reproduced with permission from [69]. Copyright © 2010, John Wiley & Sons

the particle size and increase the homogeneity of the mixture of reactants for solid-state reactions, including high-compression roller mills, jet mills (also known as fluid energy mills), and ball mills [71, 72]. There are several types of ball mills, which are classified according to the method used to impart motion to the balls, such tumbling, vibration, and agitation.

The energy utilization of a mechanical milling method is defined as the ratio of the new surface area created to the total mechanical energy that has been used. The rate of milling is defined as the amount of new surface area created per unit mass of particles per unit time. Therefore, these two terms can be connected each other. The energy utilization of a mechanical milling method increases with increasing rate of milling. Higher rate of milling means that shorter time is required to achieve a desired particle size. For every method, it is important to understand the relationship between the rate of milling and various experimental parameters. It is also worth mentioning that too high rate of milling could produce high temperature, leading to damage of the milling facilities.

During a milling process, the particles experience mechanical stresses at their contact points due to compression, impact, or shear with the mill medium or with other particles. The mechanical stresses lead to elastic and inelastic deformation of the particles. Once the stress exceeds the ultimate strength of the particles, they will be fractured. Due to the application of the mechanical energy, new surfaces are

creased on the particles. At the same time, there are changes in other physical properties of the particles, such as inelastic deformation, increase in localized temperature, lattice rearrangements within the particle and creation of various defects. Changes in chemical properties, especially on the surfaces, could also occur, if a prolonged milling is applied or the milling conditions are very vigorous, such high-energy milling, as discussed later. Generally, the energy utilization of the process is not very high, ranging from <20 % for milling by compression forces to <5 % for milling by impact.

Planetary ball milling is the most widely used technique in both laboratory research and industrial production. The efficiency of milling depends on a number of factors, including the milling parameters, i.e., speed, ball size and ball-to-powder weight ratio, and so on, the properties and types of the milling media, e.g., density and hardness, and the properties of the particles to be milled. For a given size of milling medium, because the mass is proportional to the density, the milling medium should be made of materials with as high density as possible. The size of the milling medium is an important consideration. For a given volume, the number of balls increases inversely as the cube of the radius. As stated earlier, the rate of milling is dependent on the number of contact points between the balls and the powder. The number of contact points is proportional to the surface area of the balls, so that the rate of milling increases inversely as the radius of the balls. However, too small balls cannot supply sufficient mechanical energy to fracture the particles.

The rate of milling also depends on milling time. In the beginning of milling, the decrease in size of the particles is faster. Once the particles are refined to range of about 1 μm to a few micrometers, the rate decreases and further reduction in size becomes more and more difficult. A milling limit is approached, which is determined by several factors. One important factor is the increased tendency of the particles to agglomerate with decreasing particle size. A physical equilibrium is therefore established between the agglomeration and refining processes. Another factor is the decreased probability for the occurrence of a refining event with decreasing particle size.

A disadvantage of ball milling is the wear of the milling medium, which causes potential contamination. For transparent ceramics, the presence of any impurities in the starting powders could be a serious problem. The best solution is to use balls with the materials and composition that are same as the powders to be milled. However, this is only possible for some specific compounds. Therefore, use a milling medium that is chemically inert at the firing temperature of the body (e.g., ZrO_2 balls) or can be removed from the powder by washing (e.g., steel balls). If high-energy milling is required, it is necessary to use WC or at least stainless steel media. A number of commercially available milling balls and their density are listed in Table 3.1.

Tumbling ball mills are the simplest ball mills, consisting of a relatively slow rotating horizontal cylinder that is partly filled with milling balls and the particles to be ground. Besides the factors discussed above, the speed of rotation of the mill is an important parameter, because it determines the trajectory of the balls and the

Table 3.1 Commercially available milling media for ball milling

Milling media	Density (g cm^{-3})
Si_3N_3	2.3
SiC	3.1
Al_2O_3 (<95 % purity)	3.4–3.6
Al_2O_3 (>99 % purity)	3.9
MgO-stabilized ZrO_2	5.5
Y_2O_3-stabilized ZrO_2	6.0
Stainless steel	7.7
Tungsten carbide (WC)	14.5

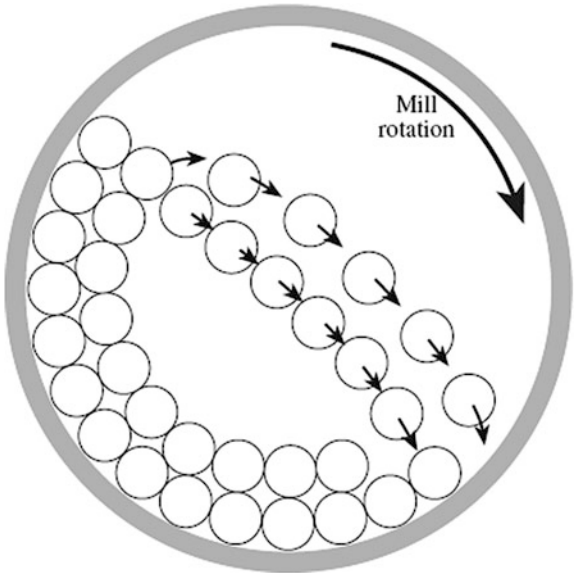

Fig. 3.9 Schematic of a ball mill in cataracting motion showing the movement of the media as the mill rotates about its axis. Reproduced with permission from [47]. Copyright © 2007, Springer

mechanical energy applied to the powders. Identifying the critical speed of rotation as the speed required to take the balls to the apex of revolution, i.e., to the top of the mill, where the centrifugal force just balances the force of gravity. It is found that the critical speed, in revolutions per unit time, is equal to $(g/a)^{1/2}/(2\pi)$, where a is the radius of the mill and g is the acceleration due to gravity. In practice, ball mills are operated at about 75 % of the critical speed so that the balls do not reach the top of the mill, as shown in Fig. 3.9 [47].

An empirical relationship for rate of milling (r_{mill}) is given by:

$$r_{\text{mill}} \approx A a_m^{1/2} \frac{\rho d}{r}, \tag{3.18}$$

where A is a numerical constant that is specific to the mill that is used and the powder that is milled, a is the radius of the mill, ρ is the density of the balls, d is the

particle size of the powder, and r is the radius of the balls. According to this relationship, the rate decreases with decreasing particle size. However, there is a practical milling limit that is reached after a certain time of milling. The variation of the rate of milling with the radius of the balls is not always valid, because too small balls cannot supply sufficient energy to fracture the particles.

The objective of the milling is to refine the powders. Therefore, the balls are expected to fall onto the particles at the bottom of the mill rather than onto the mill liner itself. To operate a mill at 75 % of its critical speed, for dry milling, the balls should be 50 % of the mill volume, while the powder filling should be about 25 % of the mill volume. For wet milling, the values should be about 50 % for balls and 40 % for the slurry. At the same time, the solid content in the slurry should be 25–40 %. Comparatively, the energy utilization of wet ball milling is higher that of dry milling by 10–20 %. Furthermore, wet milling produces powders with higher fraction of finer particles. However, wet milling has increased wear of the milling media, needs additional process to dry the powder after milling, and thus easily introduces contamination.

Another type of ball mill is vibrational ball mills or vibro-mills, which consist of a drum, filled with a well-packed arrangement of milling media and the charge of particles. The conventional vibrational mills are operated at frequencies of 10–20 Hz in three dimensions. The milling medium, usually cylindrical in shape, occupies more than 90 % of the mill volume. The amplitude of the vibrations is controlled so as not to disrupt the well-packed arrangement of the milling media. The three-dimensional motion helps the distribution of the particles. In the case of wet milling, segregation of the particles in the slurry can be minimized. The rapid vibratory motion produces an impact energy that is much greater than the energy supplied to the particles in the tumbling ball mills. Vibratory ball mills therefore provide a much more rapid refining process comparatively. They are also more energy efficient than tumbling ball mills. Currently, the vibration frequencies have been significantly increased.

Agitated ball mills, also known as attrition mills or stirred media mills, are also widely used for ceramic processing. One of the characteristics of attrition mills is that the milling chambers are not rotated during the milling. Therefore, the stock of particles and the milling medium are stirred vigorously with a stirrer rotating continuously at frequencies of 1–10 Hz. The milling chamber can be arranged either vertically, as shown in Fig. 3.10, or horizontally with the stirrer located at the center of the chamber [47]. The milling media consist of small spheres, 0.2–10 mm in diameter, which fill 60–90 % of the available volume of the mill. They can be used for either dry milling or wet milling. Agitated ball milling can be conducted in a continuous way, where the slurry of particles to be milled is fed in at one end and the milled product is released at the other end. For intensive milling, a large amount of heat will be produced, which should be taken away by cooling the milling chamber.

Agitated ball mills have a distinct advantage over tumbling ball mills and vibratory ball mills, due to their higher energy utilization. They also allow to deal with slurries with relatively higher contents of solids. The milling efficiency can be

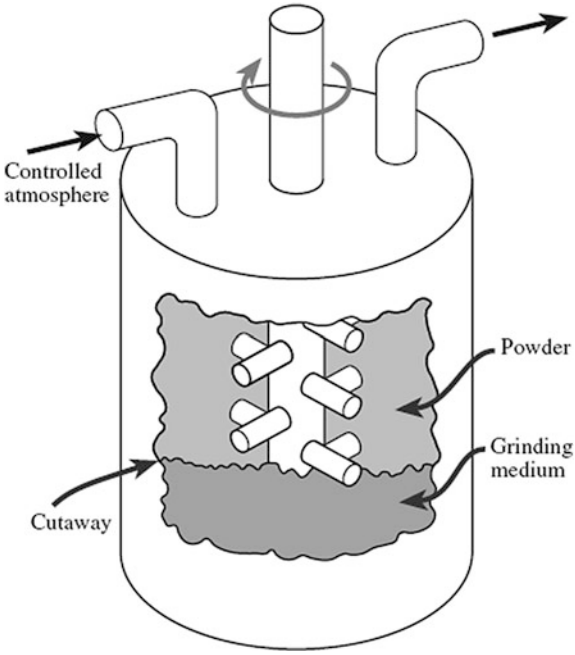

Fig. 3.10 Schematic of an attrition mill system with vertical configuration. Reproduced with permission from [47]. Copyright © 2007, Springer

further enhanced by using fine milling media. In this respect, the contamination of the milled powder is less serious, when compared with the tumbling ball mills and vibrational ball mills. Contamination in agitated ball milling can be further reduced by lining the mill chamber with ceramic materials, combined with the use of ceramic stirrers and milling media.

3.2.1.4 Mechanochemical Synthesis and Activation

The initial purpose of mechanical milling is to modify physical characteristics of ceramic powders, such as reducing the particle size and narrowing the size distribution. However, the exploitation of chemical changes during milling for the preparation of powders has received some interest in recent years. Milling enhances the chemical reactivity of powders. Rupture of the bonds during particle fracture results in surfaces with unsatisfied valences. This, combined with the high surface area favors reaction between mixed particles or between the particles and their surroundings.

Powder preparation by high-energy ball milling of elemental mixtures is referred to by various terms, including mechanochemical synthesis, mechanosynthesis, mechanical driven synthesis, mechanical alloying, and high-energy milling. While no term has received widespread acceptance, the term mechanochemical synthesis will be used in this book, unless otherwise specifically stated. The method was

initially developed for the production of powders of metals and alloys [73–76]. While less attention has been paid to inorganic systems, the method has been investigated for the preparation of a variety of nonmetallic powders, either directly synthesized or highly activated [36, 71, 77–87].

Mechanochemical synthesis can be carried out in small mills, such as the Spex mill, for synthesizing a few grams of powder or in attrition mills for larger quantities. In the Spex mill, a cylindrical vial containing the milling balls and the charge of particles undergoes large amplitude vibrations in three dimensions at frequencies of up to 1 kHz. The charge occupies about 20 % of the volume of the vial, and the amount of milling media (in the form of balls 5–10 mm in diameter) makes up 2–10 times the mass of the charge. The milling is normally carried out for a few tens of hours for the set of conditions indicated here. The method therefore involves high-intensity vibratory milling for very prolonged time periods.

One of the most distinctive advantages of mechanochemical synthesis is the ease of preparation of powders that can otherwise be difficult to produce, such as those of YAG and spinel. One of the most serious disadvantages is the introduction of impurities from the mill and milling medium into the powders.

The mechanism of mechanochemical synthesis is still not clarified. First, it could be due to the occurrence of the reaction by a solid-state diffusion mechanism. Since diffusion is thermally activated, it would require a significant lowering of the activation energy, a considerable increase in temperature during the milling, or combination of the two. Second, although considerable heat is created, the temperature is significantly lower than that required for a solid-state reaction. Therefore, localized high temperature could trigger the reaction to occur, which then propagandas throughout the whole powder. Additionally, it is also possible that self-propagation reaction could be occurring. However, this is only possible for those highly exothermic reactions, such as the formation of silicides or carbides, not very applicable to oxides like transparent ceramics.

The fabrication of transparent ferroelectric ceramics, involving high-energy ball milling, has been demonstrated for PLZT(x/65/35) (x = 6–9), PMN, and PMN-PT [88–90]. Here, PLZT8/65/35 is used as an example [90]. Commercially available PbO, La_2O_3, ZrO_2, and TiO_2 powders were used as the starting materials with the nominal composition of $(Pb_{0.92}La_{0.08})(Zr_{0.65}Ti_{0.35})_{0.98}O_3$ (PLZT8/65/35), with 10 wt% excess PbO, used to compensate the lead evaporation during the sintering process. The milling operation was carried out by using a planetary high-energy ball milling system in air at room temperature for 36 h. A 250 ml tungsten carbide vial and 100 tungsten carbide balls with diameter of 10 mm were used as a milling medium, with a ball-to-powder weight ratio of 40:1. The milling speed was set at 200 rpm, while the milling was stopped for 5 min for every 25 min of milling to avoid the potential overheating of the system.

The milled powder was then pressed uniaxially into 10 mm diameter pellets. The green pellets of about 70 % of the theoretical density were sintered in air for 4 h at temperatures from 900 to 1000 °C, with both heating and cooling rate being 10 °C min^{-1}. Transparent PLZT ceramics could be obtained by annealing the

sintered samples at 1125 °C for 6 h. Such annealing was repeated four times, resulting in a total annealing time of 24 h.

Figure 3.11 shows XRD pattern of the oxide mixture with a composition of PLZT8/65/35, which was high-energy ball milled for 36 h. Perovskite phase of PLZT is the predominant phase, while a peak of PbO is still observed, which can be attributed to the excessive and unreacted PbO. This observation means that the high-energy ball milling can trigger the reaction of the oxide components to form the desired compound. As mentioned earlier, although localized high temperature is possible, the overall temperature of the milling system (milling media plus the milled powder) is very close the room temperature. Therefore, the phase formation mechanism triggered by the high-energy ball milling should be different from that caused by high temperature reaction [91–93]. Figure 3.12 is the SEM image of the

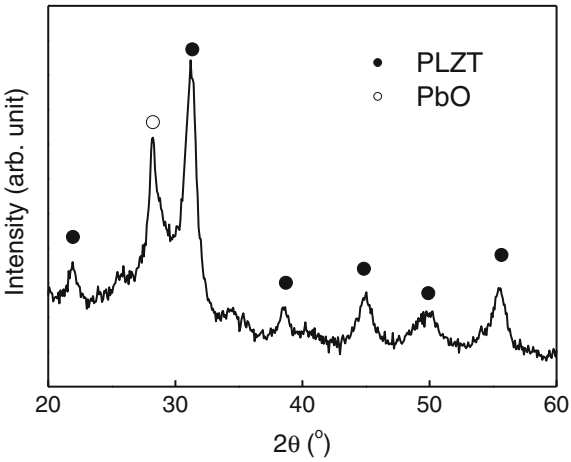

Fig. 3.11 XRD pattern of the oxide mixture with a nominal composition of PLZT8/65/35 milled for 36 h in air at room temperature. Reproduced with permission from [90]. Copyright © 2001, Elsevier

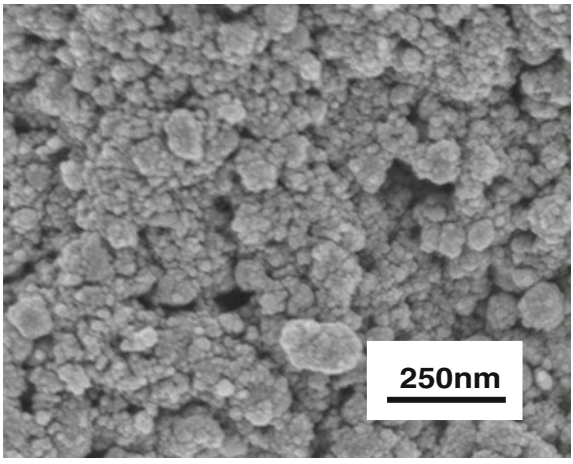

Fig. 3.12 SEM image of the milled oxide mixture. Reproduced with permission from [90]. Copyright © 2001, Elsevier

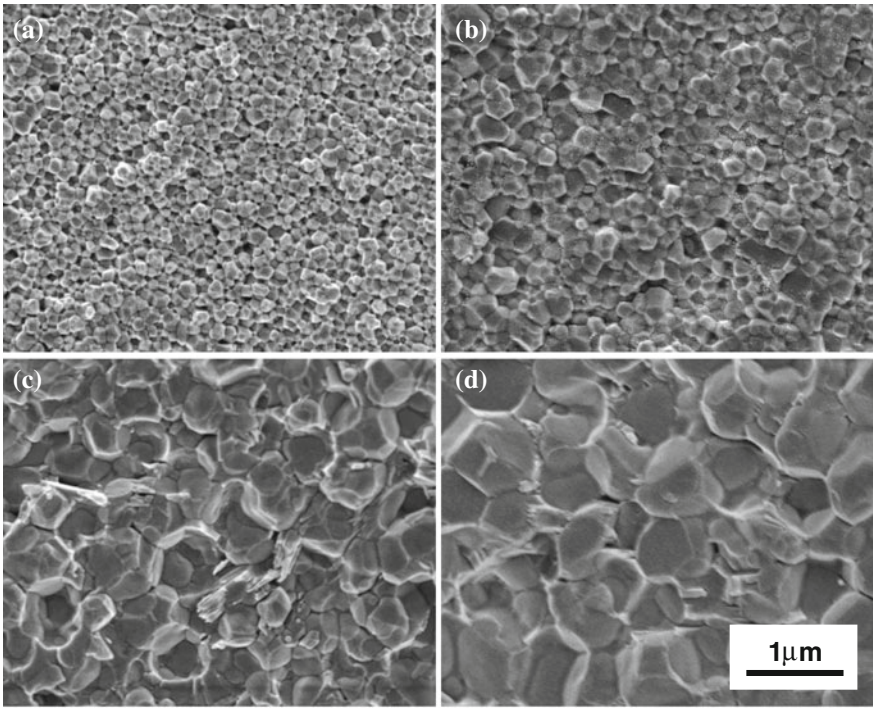

Fig. 3.13 Cross-sectional SEM images of the PLZT ceramics derived from the milled oxide mixture sintered for 4 h at different temperatures: **a** 900 °C, **b** 925 °C, **c** 950 °C and **d** 1000 °C. Reproduced with permission from [90]. Copyright © 2001, Elsevier

as-milled powder, showing that powder has a particle size at the scale of tens of nanometer. It is believed that the refined characteristic of the powders caused by the high-energy ball milling that makes it possible to obtain the fully dense PLZT ceramics at sintering temperature of as low as 1000 °C. It can be understood that the continuous milling would also prevent the growth of the particles.

Figure 3.13 shows cross-sectional SEM images of the samples sintered at different temperatures for 4 h. After sintering at 900 °C, the sample has an average grain size of only about 0.38 μm, even though the grains are well developed with clear grain boundaries. As the sintering temperature is increased to 925 °C, the average grain size slightly increases to 0.41 μm. The microstructures of the PLZT ceramics sintered at 900 and 925 °C are nearly identical. When the sintering temperature is increased to 950 °C, the average grain size of the sample is increased greatly to about 1.1 μm. Further increase in sintering temperature did not result in significant grain growth, with average grain sizes of 1.5 μm for 975 °C and 1.8 μm for 1000 °C. It means that 950 °C is a critical sintering temperature at which a sharp increment in grain size of the PLZT ceramics occurs. Figure 3.14 shows surface SEM images of the chemically etched PLZT ceramics, which were derived from the

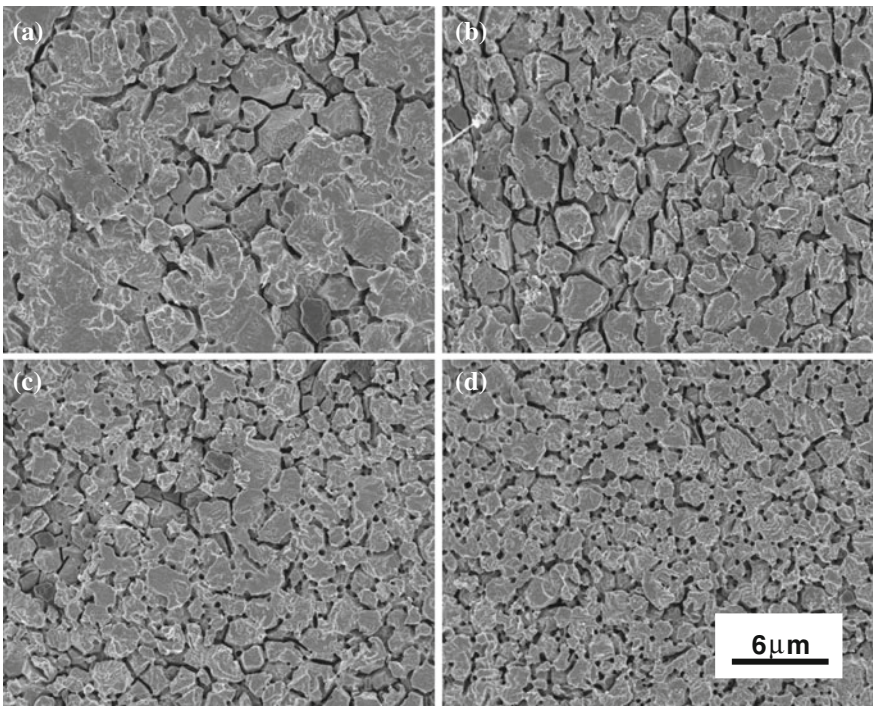

Fig. 3.14 Chemically etched surface SEM images of the 1125 °C-annealed PLZT ceramics that were previously sintered for 4 h at different temperatures: **a** 900 °C, **b** 925 °C, **c** 950 °C and **d** 1000 °C. Reproduced with permission from [90]. Copyright © 2001, Elsevier

sintered samples by repeatedly annealing at 1125 °C for 6 h for 4 times. Obviously, the grain size of the annealed samples decreases gradually with sintering temperature.

The variations of average grain size of the sintered and annealed PLZT ceramics, as a function of sintering temperature, are shown in Fig. 3.15. This observation can be explained, by considering the process as a two-step sintering. A two-step sintering process was used to control the grain growth of nanosized Y_2O_3, in which the Y_2O_3 was initially heated to 1310 °C without stop and then cooled to 1150 °C and kept at the temperature for 20 h [94]. Fully sintered Y_2O_3 ceramics without final-stage grain growth could be achieved. The suppression of the final-stage grain growth has been attributed to that the second-step sintering proceeded in a 'frozen' microstructure with slower kinetics. For the PLZT ceramics sintered at different temperatures, the 'frozen' degree in microstructure was different. The higher the sintering temperature at which the ceramics were obtained, the higher the 'frozen' degree in microstructure. Therefore, the PLZT ceramics sintered at low temperature with small grain size will lead to the annealed samples with large grain size. The annealed PLZT ceramics were all transparent, with optical properties similar to

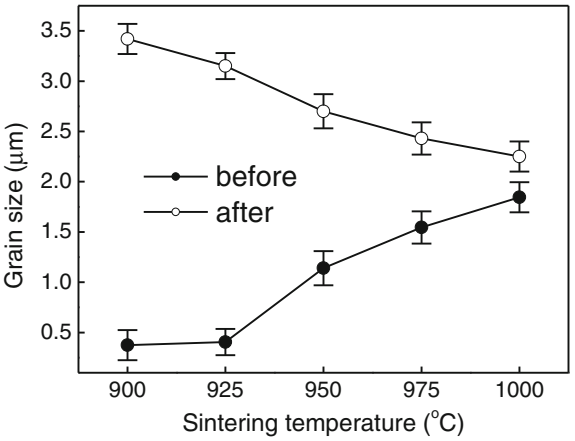

Fig. 3.15 Grain size variations as a function of sintering temperature of the PLZT ceramics before and after thermal annealing at 1125 °C. Reproduced with permission from [90]. Copyright © 2001, Elsevier

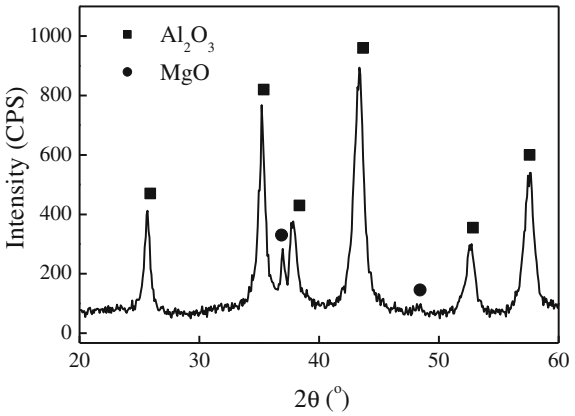

Fig. 3.16 XRD pattern of the mixture of MgO and Al_2O_3 (for $MgAl_2O_4$) milled for 12 h. Reproduced with permission from [37]. Copyright © 2002, Elsevier

those fabricated by using other methods reported in the open literature, demonstrating the efficiency and effectiveness of this mechanochemical synthesis technique.

Planetary high-energy ball milling has also been used to synthesize spinel and YAG powders [36, 37, 95]. Commercially available MgO (99.99+ % purity) and Al_2O_2 (99.9+ % purity) powders were mixed with the composition of $MgAl_2O_4$, which for 12 h, with milling parameters similar to those used for the above PLZT. Figure 3.16 shows XRD pattern of the mixture of MgO and Al_2O_3 that was milled for 12 h [37]. There is no other phase observed in the XRD pattern, which means that no reaction occurred during the milling process. However, the broadened and reduced diffraction peaks of Al_2O_3 and MgO imply that the grains of Al_2O_3 and MgO have been greatly refined as a result of the high-energy ball milling. This is evidenced by the SEM image of the milled mixture, as shown in Fig. 3.17. The milled mixture powder has grain sizes from 100 to 300 nm. Some small particles are within tens of nanometers. The refined structure of the milled mixture is directly

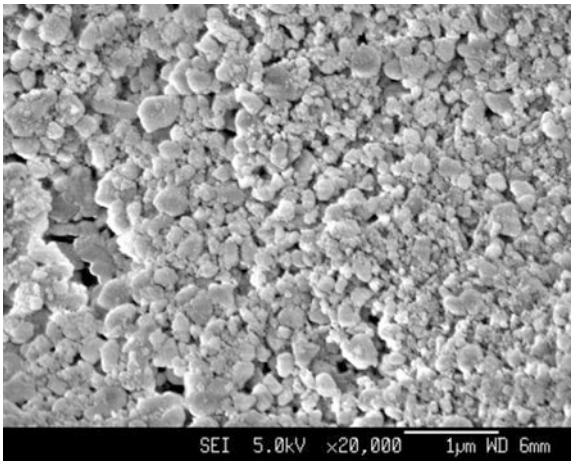

Fig. 3.17 SEM image of the mixture of MgO and Al_2O_3 (for $MgAl_2O_4$) milled for 12 h. Reproduced with permission from [37]. Copyright © 2002, Elsevier

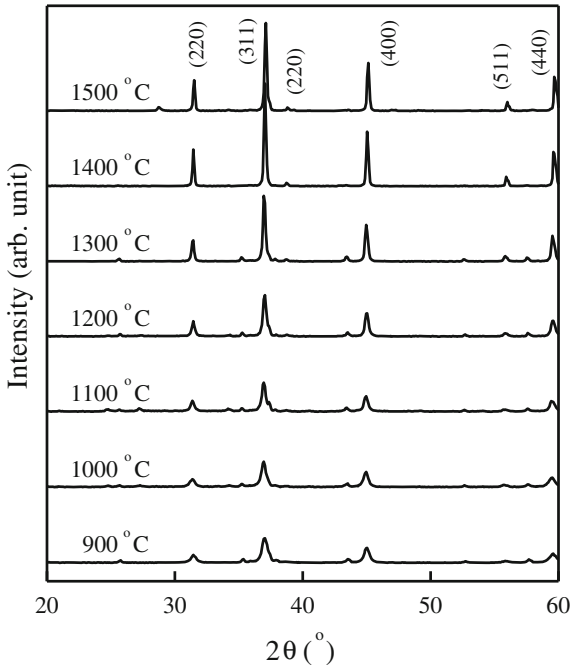

Fig. 3.18 XRD patterns of the mixture of MgO and Al_2O_3 (for $MgAl_2O_4$) milled for 12 h after calcination at various temperatures for 2 h. Reproduced with permission from [37]. Copyright © 2002, Elsevier

allows the low temperature formation of $MgAl_2O_4$ spinel phase from the mixture. In this case, the high-energy milling is not to facilitate the chemical reaction, but only to refine the powders so as to increase their reactivity and thus decrease the phase formation temperature.

Figure 3.18 shows XRD patterns of the milled mixture calcined at different temperatures for 2 h. The $MgAl_2O_4$ spinel phase was readily formed after calcining

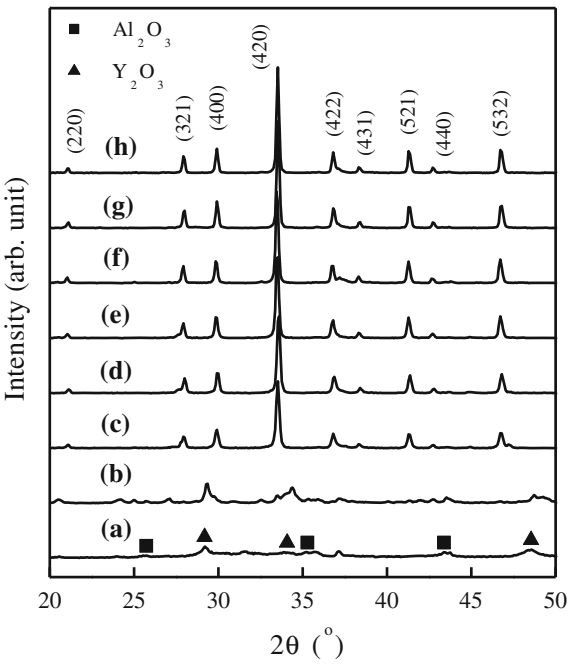

Fig. 3.19 XRD patterns of the mixture of Y_2O_3 and Al_2O_3 (for $Y_3Al_5O_{12}$) milled for 12 h after calcination at various temperatures for 2 h: **a** as-milled, **b** 900 °C, **c** 1000 °C, **d** 1100 °C, **e** 1200 °C, **f** 1300 °C, **g** 1400 °C and **h** 1500 °C. Reproduced with permission from [36]. Copyright © 2002, Elsevier

at 900 °C for 2 h, indicating the high reactivity of the MgO and Al_2O_3 mixture as a result of the high-energy ball milling. This temperature is significantly lower than required by the conventional solid-state reaction process where calcinations temperature is usually as high as 1300 °C. Therefore, this temperature (900 °C) for the phase formation of $MgAl_2O_4$ is comparable with those required by using most wet-chemical routes. However, the mechanical milling method is much simpler than the chemical ways, showing its potential application in the fabrication of transparent ceramics.

Similar results were observed for YAG [36]. Mixture of commercial Y_2O_3 and Al_2O_2 powders, with the nominal composition of $Y_3Al_5O_{12}$, was milled for 12 h. The milled mixture was then calcined for form YAG. Figure 3.19 shows XRD patterns of the milled powder which was calcined at different temperatures. YAG phase was formed after calcining at 1000 °C, which consisted of particles with an average particle size of 0.1–0.2 μm. Both the grain size and grain morphology of the YAG powders produced by using the high-energy ball milling are similar to those which were synthesized by using the chemical routes reported in the literature.

In another study, the refining effect of the high-energy milling has been confirmed by using TEM observation. Figure 3.20 shows TEM and high resolution (HR)TEM images of the Y_2O_3 and Al_2O_2 mixture ball milling for 20 h. Although agglomerated particles were formed due to the milling, they consisted of nanosized crystals, as shown in Fig. 3.20b. It is also found that there are defects, such as lattice

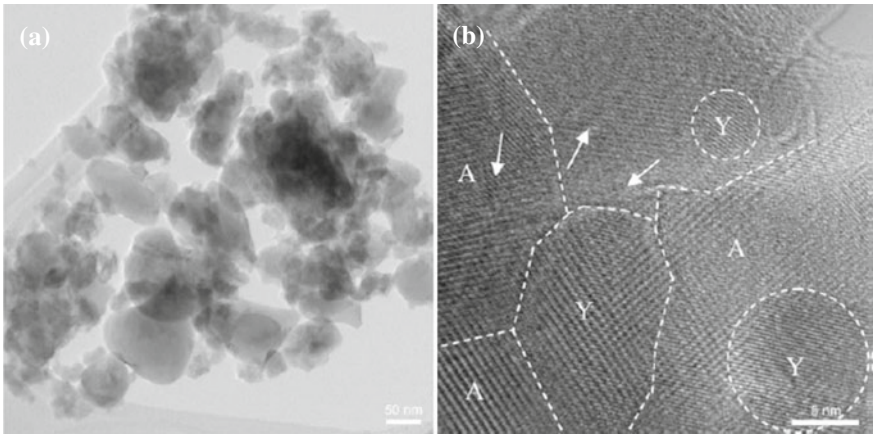

Fig. 3.20 TEM (**a**) and HRTEM (**b**) images of the mixture of Y_2O_3 and Al_2O_3 (for $Y_3Al_5O_{12}$) milled for 20 h (A for Al_2O_3 and Y for Y_2O_3). Reproduced with permission from [96]. Copyright © 2009, Elsevier

mismatch and nanocracks, at the boundaries of the small crystals. The presence of such defects, together with the nanosized crystals, has been responsible for the low temperature formation of YAG. It is expected that such powders should be suitable to produce transparent ceramics, which deserves further development.

Besides the examples discussed above, ball milling has also been used to modify or treat powders to have improved sintering behavior and thus optical properties, although the mechanisms behind are still not clearly identified [97–101].

A commercial jet mill was used to treat Yb^{3+} doped Lu_2O_3 powder that was synthesized by using co-precipitation method [97]. The effect of feed rate was specifically studied. It was found that jet milling is able to break large agglomerates without cross-contamination. Median agglomerates were refined from 8.74 to 1.06 μm, when the powder was jet milled at an optimized feed rate 0.75 lb h^{-1}. By using a sacrificial run, contamination could be effectively eliminated. The Yb:Lu_2O_3 ceramics made from the jet milled powders exhibited homogeneous microstructure and high transparency, with transmission very close to the theoretical limit. The jet mill was lined with tungsten carbide (WC).

A similar effect was observed when ball milling was used to treat commercial Lu_2O_3 powder, followed by sintering with spark plasma sintering method [98]. The application of ball milling could reduce the particle size of commercial Lu_2O_3 powder, so that the as-sintered samples derived from the milled powder had larger grain sizes than those from the unmilled powder. It was found that the former had much poorer optical transmittance, which was attributed to the assumption that ball milling introduced defects into the Lu_2O_3 powder, because no direct evidence provided in that study. However, after the two groups of samples were annealed at 1050 °C for 12 h, they became almost the same without obvious difference in appearance. Furthermore, the samples made with the milled powder had slightly

higher optical transmittance in the visible range. This is because thermal annealing eliminated the defects in the samples from the milled powder and due to their large grain sizes they possessed better optical properties. Although this effect is not very significant, it could be of interest and importance when a slight increase in transparence may lead to great improvement in performance, especially for laser applications. The milling in this study was conducted with ZrO_2 media in ethanol.

The effect of ball milling has also been demonstrated in other transparent ceramics. It was shown that, when using Y_2O_3, α-Al_2O_3, and Nd_2O_3 to prepare Nd:YAG ceramics through solid-state reaction, ball milling time had a crucial effect on particle size, densification behavior, microstructure development of the powder, and optical properties of the final transparent ceramics [99]. It was found that 12 h is the critical milling time, below which porosity of the Nd:YAG ceramics sintered at given temperatures was decreased with increasing milling time. Above this milling time, further increase in milling time had no obvious effect. The main reason is the refinement of the coarse powders due to the ball milling. A planetary ball mill, with 10 mm diameter alumina (Al_2O_3) balls, was used to mill the powders in ethanol. The disc and bottle (vial or container) rotation speeds were 130 and 260 rpm, respectively. The balls-to-powder weight ratio was 3:1, while the solid loading of the ball milled slurry was about 1.8 g ml^{-1}.

A very interesting observation on the effect of ball milling on densification and optical properties of Ho:Y_2O_3 transparent ceramics prepared by using solid-state reaction method with commercial oxide powders [101]. Commercial Y_2O_3 (>99.99 %), Ho_2O_3 (>99.99 %), and ZrO_2 (>99 %) powders were mixed, according to the stoichiometric composition of $(Ho_{0.005}Y_{0.995})_2O_3$, with 3 wt% ZrO_2 as sintering aid. A planetary milling machine was used for the ball milling experiment, with milling of 15 h, speed of 140 rpm and agate balls (5 mm in diameter) in high purity ethanol. Powder and ball filling was fixed, with the weight ratio of powder: ball of 1:2. The solid content (C_S) of the slurry, or called slurry concentration, was adjusted between 33.2 and 17.4 vol%, i.e., C_S = 33.2, 23.7, 20.7, 19.5, 18.4 and 17.4 vol%, by controlling the amount of ethanol. The slurry was then dried at 80 °C for 24 h and sieved through a 140-mesh screen. After removing organic components by calcining at 800 °C for 3 h, the powders were uniaxially pressed into pellets at 15 MPa. The pellets were then further cold isostatically pressed (CIP) at 200 MPa. After CIP, the green bodies were sintered by using a vacuum furnace under vacuum ($P \leq 10^{-3}$ Pa) for various times at temperature range of 1400–1850 °C. It was found that the slurry concentration has an obvious effect on agglomeration behaviors of the powders, which 18.4 vol% is an optimized concentration.

Figure 3.21 shows relative densities of the Ho:Y_2O_3 ceramics as a function of sintering temperature, which were made with powders corresponding to different slurry concentrations. In the range of *C*s = 33.2–18.4 vol%, the relative density of the sintered samples increased steadily with decreasing slurry concentration at every given sintering temperature. After sintering at 1850 °C for 2 h, the samples with 20.7–17.4 vol% slurry concentration were sintered to over 99 % relative density, while those with slurry concentration of 23.7 and 33.2 vol% had much lower bulk density, reaching only 98.1 and 97.3 %, respectively. This implies that

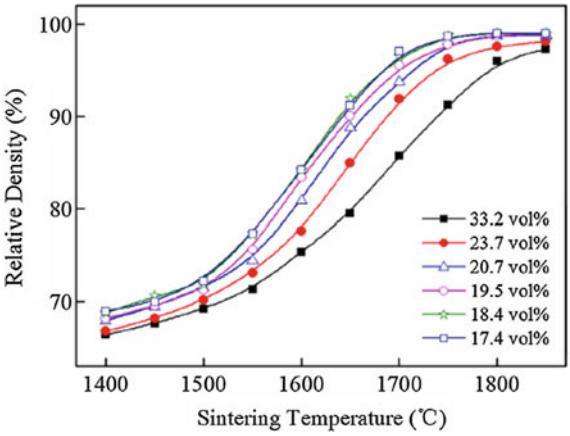

Fig. 3.21 Relative density versus sintering temperature for the ZrO_2-doped Ho:Y_2O_3 ceramics derived from the powders ball milled with different slurry concentrations. Reproduced with permission from [101]. Copyright © 2015, Elsevier

the agglomerated powders were difficult to be completely densified, as stated earlier. The solid concentration should be optimized in the range of 17.4–20.7 vol% in this case.

Figure 3.22 shows SEM images of the Ho:Y_2O_3 ceramics for different C_S values, which were sintered at 1800 °C for 2 h. Grain boundary pores can be observed in the 33.2 vol% ceramics, as shown in Fig. 3.22a. These pores could be attributed to the large pores present between the agglomerates. Pore grain boundary separation would have occurred during the sintering process, so that it was difficult to remove the pores that have been entrapped in the samples during the sintering. The presence of the residual pores embraced in the samples became the major factors that affected their optical transparency. With decreasing slurry concentration, grain growth was gradually promoted and pores were removed, as shown in Fig. 3.22b, c.

Figure 3.23 shows grain growth kinetics for the 33.2, 23.7, and 18.4 vol% samples sintered at 1800 °C for 0.25–30 h, according to grain growth kinetic rate equation. After trying n values of 2–4, it was found that $n = 3$ provided the best fitting for the data. It has been accepted that a grain growth exponent of 3 means that grain growth was controlled by either liquid phase mass transport or solute drag mechanisms in solid-state systems, if the mass migration was controlled boundary mechanism. SEM examination indicated that only a small number of isolated grain boundary pores were observed in the sample sintered at 1800 °C for 0.25 h, which suggests that the grain growth was most likely controlled by grain boundary migration instead of pore drag. Because there was no liquid phase in this case, the cubic grain growth kinetics should be due to solute drag. It also implies that agglomeration of the powders had no effect on the sintering mechanism, but greatly influenced the microstructural development.

In-line optical transmittance spectra of the ZrO_2-doped Ho:Y_2O_3 ceramics sintered at 1800 °C for 30 h, which were from the powders corresponding to different slurry concentrations, are shown in Fig. 3.24. All the absorption peaks are related to holmium ion (Ho^{3+}) absorption in the Y_2O_3 matrix. With decreasing slurry

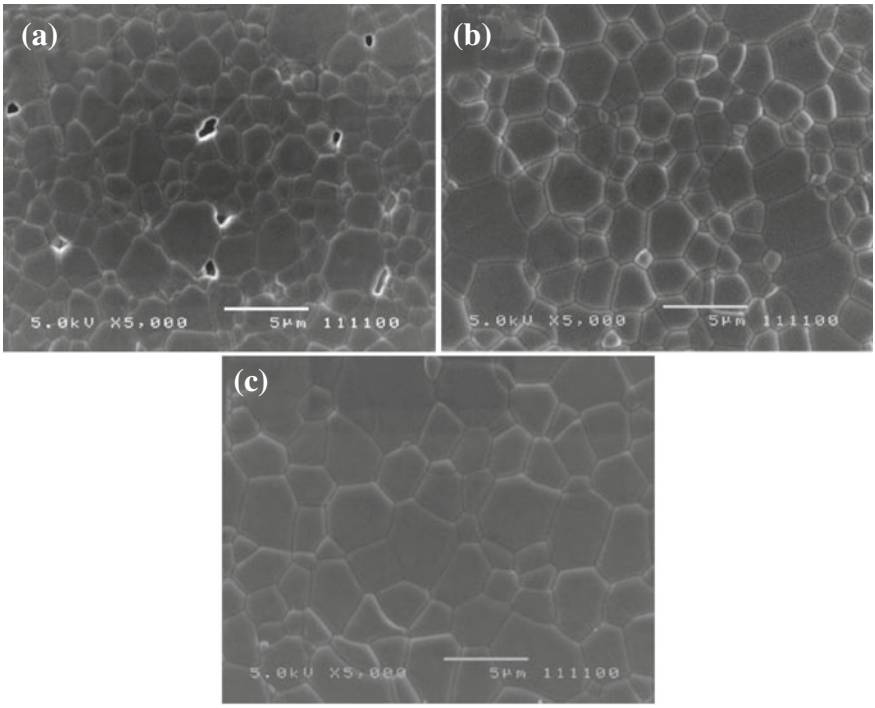

Fig. 3.22 Thermally etched surface SEM images of the ZrO_2-doped Ho:Y_2O_3 ceramics sintered at 1800 °C for 2 h in vacuum, corresponding to different slurry concentrations: **a** 33.2 vol%, **b** 23.7 vol% and **c** 18.4 vol%. Reproduced with permission from [101]. Copyright © 2015, Elsevier

concentration, transmittance steadily increased and reached the maximum in the sample with slurry concentration of 18.4 vol%. After that, it slightly dropped with further decrease in slurry concentration, implying again that the optimal slurry concentration was 18.4 vol%. It is understood that this optimization range should be different for different materials and different powder characteristics even for the same materials.

3.2.2 Wet-Chemical Routes

There are two main routes to produce ceramic powders from a solution: (i) evaporation of the liquid and (ii) precipitation by adding a chemical reagent that reacts with components in the solution. Other wet-chemical routes include: sol–gel, gel combustion, emulsion, and so on.

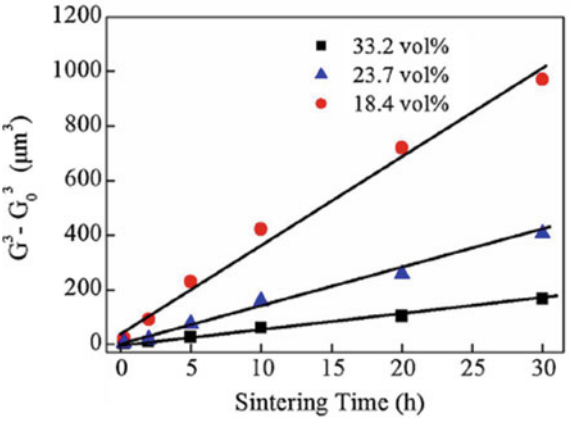

Fig. 3.23 G^3–G_0^3 vs sintering time for the ZrO_2-doped Ho:Y_2O_3 ceramics sintered at 1800 °C with different slurry concentrations. Reproduced with permission from [101]. Copyright © 2015, Elsevier

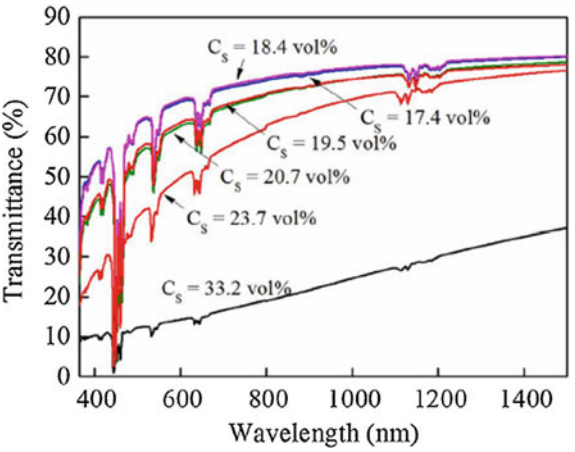

Fig. 3.24 In-line optical transmittance spectra of the ZrO_2-doped Ho:Y_2O_3 ceramics (2.14 mm thick) from the powders with different slurry concentrations. Reproduced with permission from [101]. Copyright © 2015, Elsevier

3.2.2.1 Chemical Precipitation/Co-precipitation

Mechanisms of Precipitation

The kinetics and mechanism of precipitation have been well studied and widely available in the open literature [8, 22, 23, 102–107]. Precipitation from solution involves two basic steps: (i) nucleation of fine particles and (ii) growth of the nuclei. The control of the powder characteristics is realized by controlling the reaction conditions for both nucleation and growth, as well as the extent of coupling between the two processes.

Nucleation Stage

The type of nucleation for precipitation from a solution belongs to homogeneous nucleation, because it occurs in an essentially homogeneous phase, with no foreign inclusions in the solution or on the walls of the reaction vessel. If these inclusions are present and assist the nucleation, the process is then called heterogeneous nucleation. Once heterogeneous nucleation is present, it is difficult to control the particle sizes. Therefore, heterogeneous nucleation should be avoided. However, heterogeneous nucleation can be applied to synthesize particles with desirable coatings.

The classical theories for vapor-to-liquid and vapor-to-solid transformations have been successfully used to describe the homogeneous nucleation of solid particles in solutions [108, 109]. For such a purpose, it is necessary to highlight the main features of the classical theories for vapor-to-liquid transformation. When there are random thermal fluctuations applied to a supersaturated vapor consisting of atoms or molecules, the density and free energy of the system will be fluctuated locally. Density fluctuations create clusters of atoms known as embryos, which can grow by absorbing atoms from the vapor phase. The embryos have a range of sizes in the vapor with vapor pressures that can be well described by the following Kelvin equation [110]:

$$\ln\left(\frac{p}{p_0}\right) = \frac{2\gamma v_l}{kTr}, \tag{3.19}$$

where p is the supersaturated vapor pressure, p_0 is the saturated vapor pressure, γ is the specific surface energy of the cluster, v_l is the volume of the molecule in a liquid drop that is formed by condensation of the vapor, k is the Boltzmann constant, T is the absolute temperature, and r is the radius of the embryo, which is assumed to be spherical. Due to the higher vapor pressures, small embryos evaporate back to the vapor phase. In this case, there is a critical radius r_c for the embryos. Those with radius smaller than this critical value cannot grow, while those with $r > r_c$ can grow into larger and larger ones. The formation of nuclei should overcome an energy barrier, which can be represented by the free energy change, due to the formation of a spherical nucleus with a radius r. The change in Gibbs free energy can be written as:

$$\Delta G_n = 4\pi r^2\gamma - \frac{4}{3}\pi r^3 \Delta G_v. \tag{3.20}$$

The first term on the right-hand side is the intrinsically positive contribution of the surface free energy, while the second term is due to the contribution by the bulk free energy change. With unit volume of the liquid, the free energy change G_v due to the transfer from vapor to liquid is given by [108]:

$$\Delta G_{\mathrm{n}} = \frac{kT}{v_{\mathrm{l}}} \ln\left(\frac{p}{p_0}\right), \tag{3.21}$$

where v_{l} is the volume per molecule in the liquid. Substituting for G_v in Eq. (3.20) yields:

$$\Delta G_{\mathrm{n}} = 4\pi r^2 \gamma - \frac{4}{3}\pi r^3 \frac{kT}{v_l} \ln\left(\frac{p}{p_0}\right). \tag{3.22}$$

Accordingly, if the supersaturation ratio $S = p/p_0 = 1$, the Gibbs free energy change ΔG_{n} increases monotonically as a parabola, due to the disappearance of the bulk term. For $S < 1$, the ΔG_{n} curve increases more rapidly, because a fractional S makes the second term on the right-hand side to be positive, enhancing the effect, owing to presence of the surface free energy barrier. For $S > 1$, the second term is negative, so that there is a maximum in ΔG_{n} at some critical radius r_{c}, as shown schematically in Fig. 3.25. The critical radius r_{c} is obtained by setting $\mathrm{d}(\Delta G_{\mathrm{n}})/\mathrm{d}r = 0$, which gives rise to:

$$r_{\mathrm{c}} = \frac{2\gamma v_{\mathrm{l}}}{kT \ln(p/p_0)}. \tag{3.23}$$

Putting Eq. (3.23) into Eq. (3.22), the height of the free energy activation barrier can be derived, which is:

$$\Delta G_{\mathrm{c}} = \frac{16\pi\gamma^3 v_l^2}{3[kT \ln(p/p_0)]^2} = \frac{4}{3}\pi r_c^2 \gamma. \tag{3.24}$$

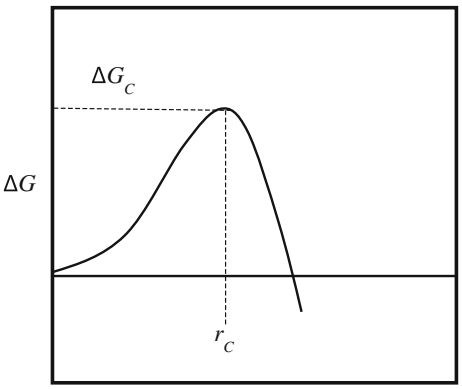

Fig. 3.25 Schematic of variation in the free energy versus radius for a spherical droplet. Some critical size must be exceeded before a nucleus becomes stable. Reproduced with permission from [111]. Copyright © 1950, American Chemical Society

Therefore, at this stage, sufficient increase in the supersaturation ratio $S = p/p_0$ results in an increase the atomic/molecular bombardment rate in the vapor, which leads to a reduction in ΔG_c and r_c, so that the probability of subcritical embryo growing to supercritical size in a short time approaches unity.

The nucleation rate I represents the rate of formation of critical nuclei, because only this kind of nuclei can grow into liquid droplets. According to the pseudo-thermodynamic treatment of vapor-to-liquid transformation, I is proportional to $\exp(-\Delta G_c/kT)$, where k is the Boltzmann constant and ΔG_c is given by Eq. (3.24). The rate of the nuclei growth is also dependent on the frequency of atoms to join it, which can be written as $v\exp(\Delta G_m/kT)$, where v is the characteristic frequency and G_m is the activation energy for atom migration. Putting $v = kT/h$, where h is Planck's constant, an approximate expression for the nucleation rate is given by [112]:

$$I \approx \frac{NkT}{h}\exp\left(\frac{-\Delta G_m}{kT}\right)\exp\left(\frac{-16\pi\gamma^3 v_l^2}{3kT[kT\ln(p/p_0)]^2}\right), \tag{3.25}$$

where N is the number of atoms per unit volume in the phase that is undergoing the transformation.

Homogeneous nucleation of particles from solution has been observed in various methods that are used to synthesize ceramic powders [113–116]. For example, in aqueous solutions, metal ions are usually hydrated [117, 118]. Embryos of hydrated metal ions are formed by progressive accumulation of ions to one another through a polymerization process. These polynuclear ions are the precursors for nucleation. When the concentration of the polynuclear ions is above some minimum supersaturation level, homogeneous nucleation starts to form solid nuclei. The nucleation rate of particles from solution can be expressed as [113]:

$$I \approx \frac{2Nv_s(kT\gamma)^{1/2}}{h}\exp\left(\frac{-\Delta G_a}{kT}\right)\exp\left(\frac{-16\pi\gamma^3 v_l^2}{3k^3T^3[\ln(C_{ss}/C_s)]^2}\right), \tag{3.26}$$

where N is the number of ions per unit volume in the solution, v_s is the volume of a molecule in the solid phase, γ is the specific energy of the solid–liquid interface, ΔG_a is the activation energy for the transport of an ion to surface of the solid, C_{ss} is the supersaturated concentration, and C_s is the saturated concentration of the ions in the solution. The nucleation rate is strongly dependent on the supersaturation ratio C_{ss}/C_s.

Particle Growth Stage

Although nuclei are very small in size, they can grow at different rates and thus have different sizes, even during the very early stage of nucleation. Therefore, the

starting point of growth of the nuclei into particles could take place at different times. Solute species, such as ions or molecules, are transported to the nuclei in a supersaturated solution, which accumulate at their surface and then are aligned with the nuclei to form particles. The rate-controlling step in the growth of the particles can be (i) diffusion toward the particle and (ii) addition of new material to the particle by surface reaction. The specific mechanisms and the coupling among them govern the final size and size distribution of the particles.

For diffusion-controlled growth, it is assumed that the nuclei are far away one another, so that each individual particle can grow at its own rate, the diffusion of solute species toward the particle can be described by Fick's first law. If the particles are assumed to be spherical with radius r, the flux J through any spherical shell of radius x is given by:

$$J = 4\pi x^2 D \frac{\mathrm{d}C}{\mathrm{d}x}, \tag{3.27}$$

where D is the diffusion coefficient for the solute through the solution and C is concentration of the solute. Assuming that the saturation concentration C_s is maintained at the particle surface and that the concentration of the solute far away from the particle is C, a concentration gradient is built up that approaches a stationary state in times of the order of r^2/D. In this stationary state, J is not dependent on x, and integration of Eq. (3.27) yields:

$$J = 4\pi r D(C_\infty - C_s). \tag{3.28}$$

The rate of increase in radius of the particle is then given by:

$$\frac{\mathrm{d}r}{\mathrm{d}t} = \frac{JV_s}{4\pi r^2} = \frac{DV_s(C_\infty - C_s)}{r}, \tag{3.29}$$

where V_s is the molar volume of the solid that is precipitating on the particle. Equation (3.28) can also be rewritten as:

$$\frac{\mathrm{d}(r^2)}{\mathrm{d}t} = 2DV_s(C_\infty - C_s). \tag{3.30}$$

This means that the square of the radius of all particles increases at the same constant rate, regardless the original size of the particles. Although the assumptions leading to Eq. (3.30) are oversimplified, it has been observed that if diffusion controlled growth is the governing mechanism, particles with different size have the same magnitude of $\mathrm{d}(r^2)/\mathrm{d}t$ [119].

If the absolute width of the particle size distribution is Δr for a mean radius r and Δr_0 for the mean radius r_0 of the system in the initial state, according to Eq. (3.30), there are:

$$\frac{\Delta r}{\Delta r_0} = \frac{r_0}{r}, \quad \frac{\Delta r}{r} = \left(\frac{r_0}{r}\right)^2 \frac{\Delta r_0}{r_0}. \tag{3.31}$$

According to Eq. (3.31), the absolute width of the size distribution becomes narrower in the ratio r_0/r and the relative width decreases even faster in the ratio $(r_0/r)^2$.

For surface-reaction-controlled growth, each new layer formed at surface of the particle has to be nucleated first by a process that is different from the homogeneous nucleation [120–124]. There are two types of growth mechanisms that have been observed: mononuclear growth and polynuclear growth. In the mononuclear growth mechanism, once a nucleation step is formed on the particle surface, there is sufficient time for the entire layer to form before a new step starts. In this case, the particles grow due to the increase in thickness of the layers on their surfaces. Due to the growth is realized layer by layer, the particle surface may have faceted appearance at the macroscopic scale. The particle growth can be described by the following equation:

$$\frac{\mathrm{d}r}{\mathrm{d}t} = K_1 r^2, \tag{3.32}$$

where K_1 is a constant. The relative width of the size distribution is given by:

$$\frac{\Delta r}{r} = \frac{r}{r_0}\frac{\Delta r_0}{r_0}, \tag{3.33}$$

which increases in the ratio r/r_0.

In the polynuclear growth mechanism, formation of nucleation steps on the particle surface is too fast, so that a new layer is created before the previous one has been completed. The growth rate is independent of the surface area of the particles, which is given by:

$$\frac{\mathrm{d}r}{\mathrm{d}t} = K_2, \tag{3.34}$$

where K_2 is a constant. In this case, the relative width of the distribution decreases according to the following equation:

$$\frac{\Delta r}{r} = \frac{r_0}{r}\frac{\Delta r_0}{r_0}. \tag{3.35}$$

Particle Size Distribution

The principles to obtain particles with a narrow size distribution by precipitation from solution have been well studied [20, 111, 125, 126]. The main features can be

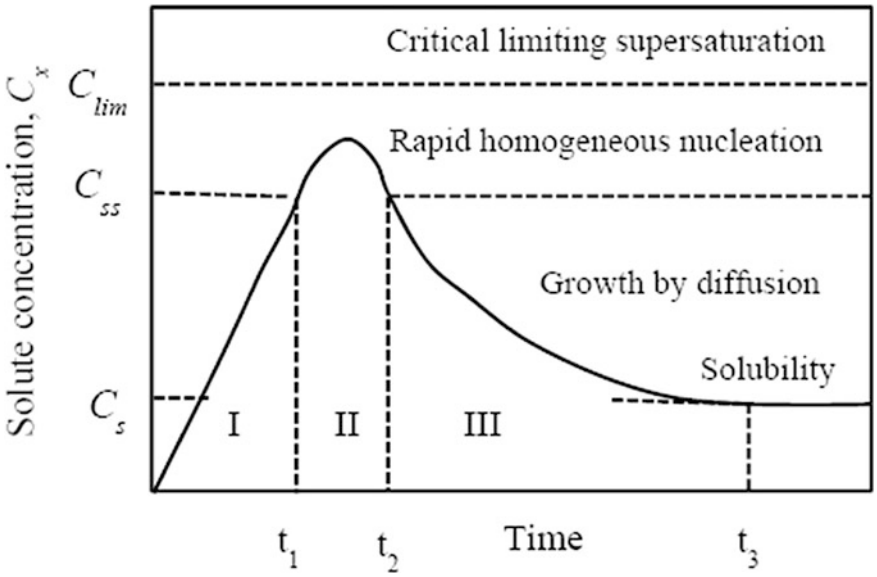

Fig. 3.26 Schematic representation of the solute concentration versus time in the nucleation and growth of particles from a solution. Reproduced with permission from [111]. Copyright © 1950, American Chemical Society

represented in the diagram shown in Fig. 3.26, which is often referred to as the LaMer diagram. With the progress of the reaction, the concentration of the solute to be precipitated, C_x, increases to or above the saturation value C_s. If the solution is assumed to be free of foreign inclusions and the container walls are clean and smooth, it is possible for C_x to largely exceed C_s, so as to form a supersaturated solution. Finally, a critical supersaturation concentration C_{ss} will be reached after some time t_1, where homogeneous nucleation and growth of solute particles will occur, leading to a decrease in C_x to a value below C_{ss} after a time t_2. Further growth of the particles continuously takes place due to diffusion of the solute through the liquid and then the precipitation onto surface of the particles. Eventually, particle growth stops after t_3 when $C_x = C_s$. To obtain particles with uniform size, the nucleation should be triggered in a short time interval, t_2–t_1. This could be achieved by using solutions with sufficiently low concentration of reactants. At the same time, the solute should be released slowly, to allow the diffusion mechanism to occur, so that solute will precipitate onto the particles without further nucleation.

Particle Aggregation

The particles synthesized by precipitation form solution could consist of aggregates of much finer primary particles [17–19, 127–132]. With DLVO theory for colloid

stability, it is found that under identical surface charge densities, the barrier to aggregation increases with the size for two equal-sized particles, so that their rate of aggregation decreases exponentially. Also, fine particles aggregate more quickly with large particles than they do with themselves. According to the model, during a precipitation reaction, the first nuclei grow rapidly by aggregation to a size that is colloidally stable. These particles then sweep through the suspension, picking up freshly formed nuclei and smaller aggregates. The formation of particles with uniform size is thus possible through the size-dependent aggregation rates.

Ostwald Ripening

The growth of particles in liquids has also been observed, through a process called dissolution–precipitation, in which the smaller particles are dissolved and the solute precipitates on larger particles. This type of growth, also called coarsening, is known as Ostwald ripening [133–137]. The coarsening of precipitates in solid media can occur by a similar process. The theory of Ostwald ripening is also known as the Lifshitz–Slyozov–Wagner (LSW) theory. Matter transport from smaller particles to larger particles can be controlled by either (i) diffusion through the liquid or (ii) interface reaction. The average radius $\langle r \rangle$ of the particles assumed to be spherical is predicted to increase with time t, according to the following equation:

$$\langle r \rangle = \langle r_0 \rangle^m + Kt, \tag{3.36}$$

where $\langle r_0 \rangle$ is average radius of the particles at the initial state, K is a constant that obeys the Arrhenius relation and m is an exponent that is dependent on the mechanisms, with $m = 2$ for interface reaction control and $m = 3$ for diffusion control. With any initial particle size distribution, the final particle size distribution always approaches a self-similar distribution, because it is dependent only on $r/\langle r \rangle$ and independent on time. The maximum radius of the distribution is $2\langle r \rangle$ for the interface reaction mechanism and $(3/2)\langle r \rangle$ for the diffusion mechanism. Therefore, Ostwald ripening alone cannot be used to obtain monodispersed powders.

Chemical Precipitation

Various powders for transparent ceramics have been synthesized by using chemical precipitation methods [138–154]. Chemical precipitation starts when a metal salt solution is mixed with a precipitant solution. Metal salts that can be used to prepare solutions mainly include chlorides, nitrates sulfates and acetates, as well as alkoxides or other forms. The most widely used precipitants are ammonia water ($NH_3 \cdot H_2O$), ammonia carbonate ($(NH_4)_2CO_3$), ammonia bicarbonate (NH_4HCO_3), sodium carbonate (Na_2CO_3), potassium carbonate (K_2CO_3), sodium hydroxide (NaOH), potassium hydroxide (KOH), urea ($CO(NH_2)_2$), hydrazine (N_2H_4), ammonium oxalate ($(NH_4)_2C_2O_4$), ammonium citrate ($(NH_4)_2C_6H_6O_7$), and so on.

The mixing of the precipitated solutions and the precipitant solutions can be conducted in various ways. Therefore, chemical precipitation is a very feasible synthesis method, which can be carried out through various combinations of the ion salts and precipitants, as well as those processing parameters. However, only limited ways have been used in the open literature.

The products or precipitates are not oxides, instead, they are most likely hydroxides or carbonates, depending on the properties of the salts and the precipitants. The ionic reactions for precipitation of Mg^{2+} and Al^{3+} are as follows:

$$Mg^{2+} + 2OH^- \rightarrow Mg(OH)_2 \downarrow, \tag{3.37}$$

$$Al^{3+} + 3OH^- \rightarrow Al(OH)_3 \downarrow, \tag{3.38}$$

$$Mg^{2+} + CO_3^{2-} \rightarrow MgCO_3 \downarrow, \tag{3.39}$$

$$2Al^{3+} + 3CO_3^{2-} + 3H_2O \rightarrow 2Al(OH)_3 \downarrow + 3CO_2 \uparrow . \tag{3.40}$$

The precipitants are filtered, washed, and dried to make oxide powders. Oxide powders can be obtained by calcining the precipitants at a suitable temperature. Properties of the final oxide powders are determined by the properties of the precipitants, including particle size, size distribution, morphology, and so on. The properties of the precipitants can be controlled by various conditions, such as type of the metallic ions, concentration of the solutions, pH value, temperature, the way of mixing, and use of additives. Particle size of the derived powders sometimes is dependent on calcination temperature.

The precipitation of magnesium carbonate, from reaction of $MgCl_2$ with Na_2CO_3, with the presence of polyacrylamide (PAM), has been studied [155]. It was found that, various factors, such as such as PAM concentration, reaction temperature, and stirring speed, could affect the precipitation behavior of magnesium carbonate. The product weight increased slightly with increasing content of PAM, but decreased slightly with increasing temperature, while the stirring speed exhibited almost no effect. The precipitants obtained at 25 and 50 °C were nesquehonite, i.e., $MgCO_3 \cdot 3H_2O$. At 75 °C, the final product was an unidentified amorphous phase. Morphology of the magnesium carbonate was determined by the concentration of the polymer. Figure 3.27 shows SEM images of the precipitates, showing the effect of PAM content on the morphology of the precipitation products. With increasing PAM concentration, particle morphology of the precipitates was changed from plate block shape to fan-like shape. This effect of PAM was attributed to the adsorption of the polymer on surface of the precipitates during the precipitation. Obviously, $MgCO_3$ powders with such morphologies are not suitable to be used for fabrication of MgO transparent ceramics.

Another example is the synthesis of MgO nanoparticles from hydroxide precipitation in aqueous solutions [156]. The precipitation was conducted at a controlled temperature, while $MgCl_2$ solution at a concentration of 1 mol L^{-1} was mixed with NaOH solution with a concentration of 2 mol L^{-1}. The two solutions

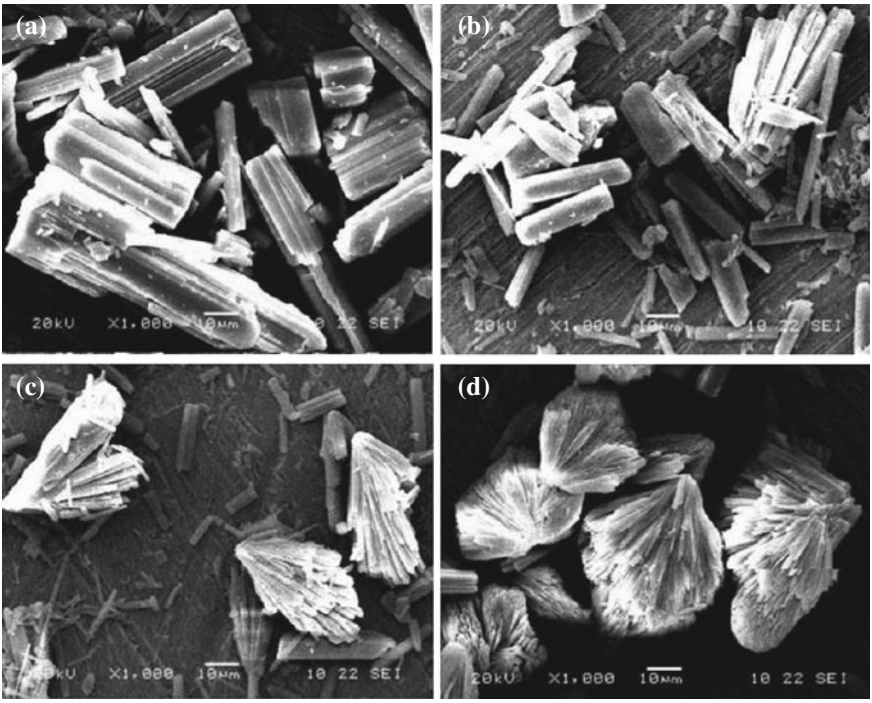

Fig. 3.27 SEM images of the powders made with different PAM concentrations (mg L^{-1}): **a** 0.2, **b** 0.4, **c** 0.6 and **d** 0.8. Reaction temperature was 25 °C, with stirring speed of 500 rpm. Reproduced with permission from [155]. Copyright © 2010, Elsevier

were mixed by simultaneously pouring into a 100 mL cylindrical container in a bath at 80 °C for 2 h. Vigorous stirring was applied during the mixing of the two solutions, while the stirring was continued during the aging of the precipitate. The suspension was aged at the reaction temperature for 2 h and then at room temperature for 1 day. The solid phase obtained was recovered by filtration, which was washed with deionized water and absolute alcohol and then air-dried at 60 °C for 4 h. The powders were finally subject to a hydrothermal treatment at 250 °C for 1 h, 370 °C for 2 h and 435 °C for 3 h, successively. Figure 3.28 shows SEM image of the MgO powder. Although the MgO powder was used for sorption of uranium, it is believed to be suitable as precursor powder transparent MgO ceramics.

There has been a report on the synthesis of nanocrystalline α-alumina powders, with a primary mean particle diameter of 10 nm, by using chemical precipitation from aluminum nitrate and ammonia solution [157]. The presence of ammonium nitrate, which was the by-product of the precipitation reaction in the $Al(OH)_3$ dry gel, was found to be able to decrease the formation temperatures of γ-, δ-, θ-, and α-Al_2O_3 during heating. With the presence of 5 wt% α-alumina seed crystals, with an average diameter of 100 nm, together with 44 % ammonium nitrate, the θ-Al_2O_3 → α-Al_2O_3 conversion temperature was decreased from 1200 to 900 °C.

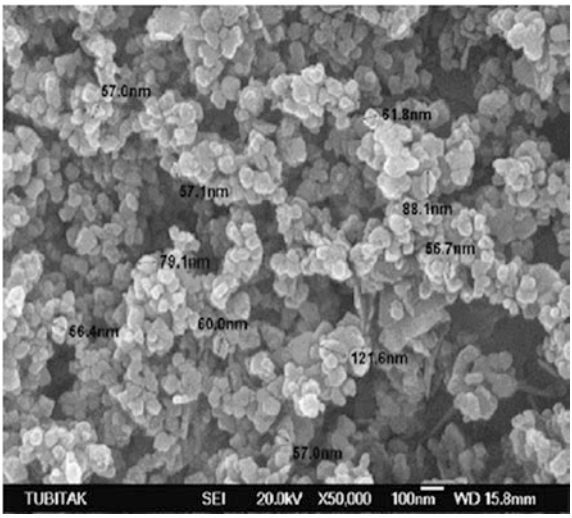

Fig. 3.28 SEM image of the MgO powders. Reproduced with permission from [156]. Copyright © 2012, John Wiley & Sons

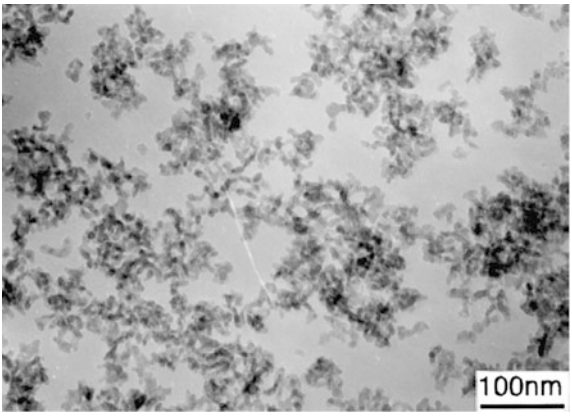

Fig. 3.29 TEM image of the α-Al_2O_3 powders before ball milling. Reproduced with permission from [157]. Copyright © 2000, Elsevier

The α-Al_2O_3 powder milled in anhydrous alcohol has an agglomeration strength of 76 MPa, which was soft agglomerate, whereas the sample milled in deionized water exhibited an agglomeration strength of 234 MPa, which belonged to hard agglomerate. Regardless to the state of agglomeration, the initial stage sintering of the two powders was controlled by grain boundary diffusion, with activation energies of 365 and 492 kJ mol^{-1}, respectively. The alumina ceramic produced by sintering the soft agglomerated powder at 1400 °C for 2 h showed a mean grain size of 0.93 μm, a mean flexural strength of 700 MPa, and a fracture toughness of 4.75 MPa $m^{1/2}$.

Figure 3.29 shows a TEM image of the as-synthesized α-Al_2O_3 powder, indicating that the diameter of the primary particles before milling is about 10 nm. Figure 3.30 shows SEM images of the α-Al_2O_3 powders milled in anhydrous

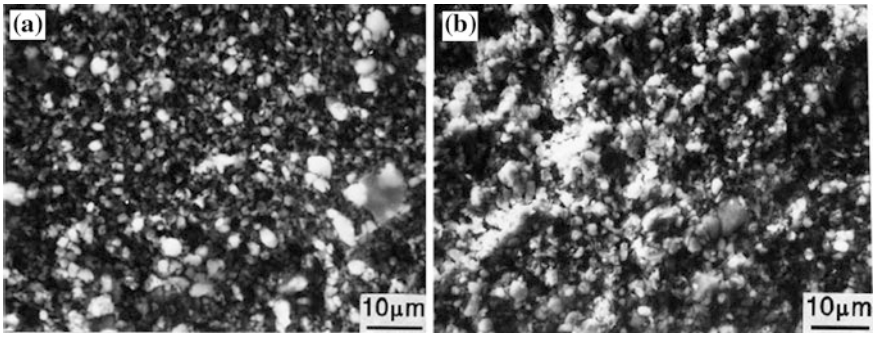

Fig. 3.30 SEM images of the α-Al_2O_3 powders milled in different solvents: **a** anhydrous alcohol and **b** deionized water. Reproduced with permission from [157]. Copyright © 2000, Elsevier

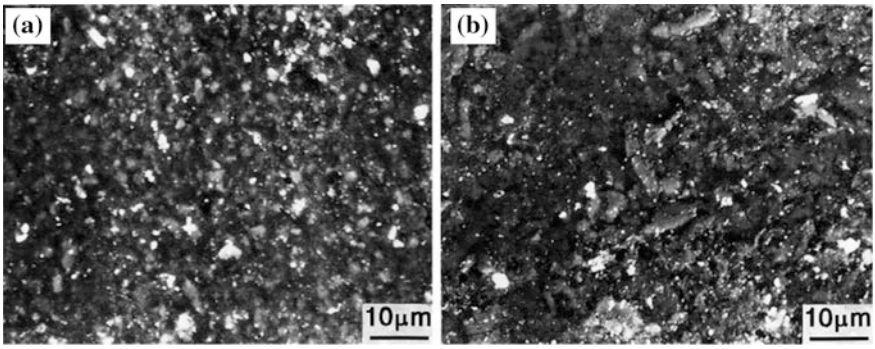

Fig. 3.31 SEM images of the green bodies from the α-Al_2O_3 powders with different agglomerations: **a** soft and **b** hard. Reproduced with permission from [157]. Copyright © 2000, Elsevier

alcohol and deionized water. After ball milling, both powders were agglomerated, with agglomerate diameters in the range from less than 0.1 μm to about 7 μm. For both powders, the green density versus compaction pressure curves consisted of two straight lines but with different slopes. By assuming that the change in slope is related to agglomeration strength, the agglomeration strengths of the two powders were estimated to be 76 and 234 MPa, for anhydrous alcohol and deionized water, respectively.

It has been accepted that the microstructural homogeneity of the green bodies is determined by the strength of agglomerates. Figure 3.31 shows SEM images of the green bodies from the two α-Al_2O_3 powders. Obviously, the sample from the powder milled in anhydrous alcohol more homogeneous than the one from the powder milled in deionized water. This is because the compaction pressure of $\sim$200 MPa was higher than the agglomeration strength of the powder milled in anhydrous alcohol, so that the agglomerates could be broken. As stated above, this

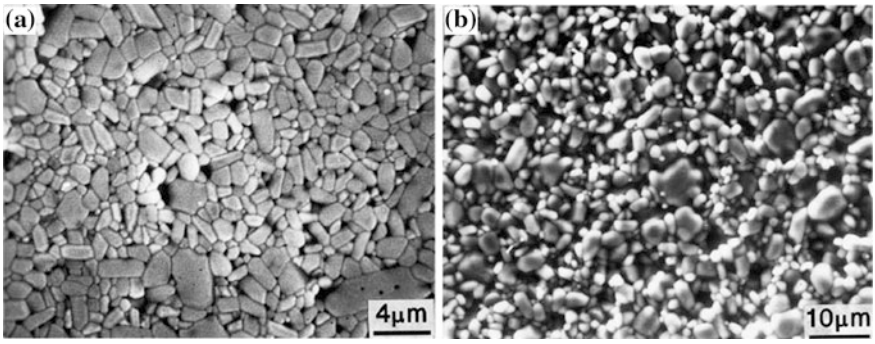

Fig. 3.32 SEM images of the final ceramics sintered at 1400 °C for 2 h from the α-Al_2O_3 powders with different agglomerations: **a** soft and **b** hard. Reproduced with permission from [157]. Copyright © 2000, Elsevier

powder was soft agglomerated. In contrast, the powder milled in deionized water had hard agglomerates, which could not be crashed down. Relative densities of the green bodies for the soft and hard agglomerated powders were 36.62 and 28.94 %, respectively. The two green bodies showed different linear shrinkage behaviors, implying their different sintering behaviors due to the different agglomeration properties.

SEM images of the final ceramics derived from the two powders are shown in Fig. 3.32 [157]. The soft agglomerated powder led to a green body with homogeneous microstructure. The final ceramics reached a relative density of 99 %, with an average grain size of 0.93 μm. Due to the inhomogeneous green body, the sample with hard agglomeration experienced a differential sintering and a different internal stresses in the compact. Comparatively, the hard agglomerated powder could only be sintered to a relative density of 73.06 %. This study provided an important reference to the development of transparent ceramics.

Monodispersed porous α-Al_2O_3 nanoparticles with controllable sizes have been prepared by using a homogeneous precipitation method [158]. The precipitation solutions were prepared with $Al(NO_3)_3{\cdot}9H_2O$ and $Al_2(SO_4)_3{\cdot}18H_2O$ in distilled water. The Al^{3+} concentration in the solutions were 10 and 0.5 mmol L^{-1}. Precipitant was urea ($CO(NH_2)_2$), with a mole ratio of $CO(NH_2)_2/Al^{3+}$ to be 100. After vigorous stirring for 0.5 h, the reaction mixtures were heated to 95 °C at a constant heating rate of 2 °C min^{-1} and then kept at the temperature for 3 h for precipitation. The precipitates obtained were thoroughly washed and then dried at 60 °C. The dried precipitates were then calcined at different temperatures for 2 h at a heating rate of 5 °C min^{-1}. α-Al_2O_3 nanoparticles could be obtained after calcination at 1200 °C. Diameters of the porous α-Al_2O_3 nanoparticles obtained with an Al^{3+} concentration of 10 mmol L^{-1} were in the range of 200–500 nm, while diameters of those with an Al^{3+} concentration of 0.5 mmol L^{-1} were in the range of 40–70 nm. The porosity developed during the heating process was due to phase transformation and shrinkage of precursor particles. Figure 3.33 shows

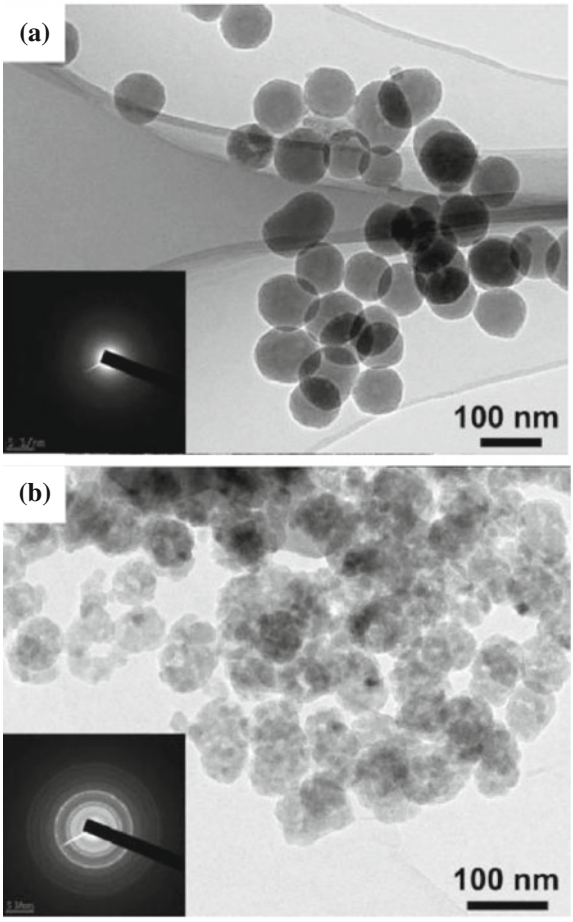

Fig. 3.33 TEM images of **a** amorphous $Al(OH)_3$ nanoparticles and **b** α-Al_2O_3 nanoparticles after a calcination at 1200 °C for 2 h. Reproduced with permission from [158]. Copyright © 2012, Elsevier

representative TEM images of the as-synthesized amorphous precipitate and nanoparticles after annealing at 1200 °C by using the precipitation method.

Ultrafine yttria particles with near-monodispersed size were synthesized solution by using a homogeneous precipitation method with urea as precipitant [159]. The effects of four experimental variables, including concentrations of yttrium ion and urea, reaction temperature, and solution pH value, on morphology of the particles and the reaction kinetics, have been studied in the system. It was found that the concentration of yttrium ion, which was varied in the range of 0.005–0.04 M, showed a significant effect on the average size of the particles, which monotonically increased from 65 nm to over 220 nm. Moreover, with increasing concentration of yttrium ion, the size distribution was gradually broadened and the particles started to form agglomeration at concentrations of 0.025 M and above, which was attributed to the reduction of zeta potential of the solutions. However, the yttrium ion concentration had no obvious effect on the rate of precipitation reaction. TEM

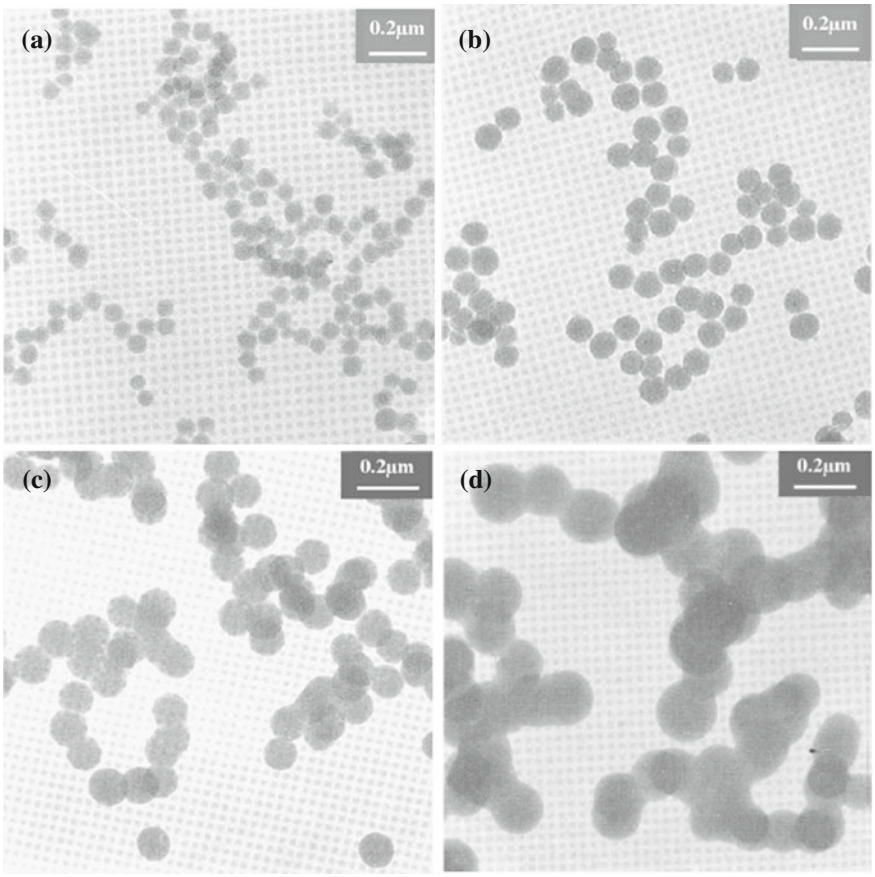

Fig. 3.34 TEM images of the precipitates from the solutions with different $Y(NO_3)_3$ concentrations: **a** 0.005 M, **b** 0.015 M, **c** 0.025 M and **d** 0.04 M. The urea concentration and pH were fixed at 1.0 and 6.0, while the reaction temperature was 95 ± 1 °C. Reproduced with permission from [159]. Copyright © 2004, Elsevier

images of representative precipitates from the solutions with different yttrium ion concentrations are shown in Fig. 3.34.

The effect of the urea concentration is somehow opposite to that of the yttrium ion concentration. As the urea concentration was increased from 0.04 to 4.0 M, the average particle size of the precipitates gradually decreased from 220 to 100 nm. However, too high urea concentration, e.g., 7.0 M, led to serious interparticle agglomeration. The rate of precipitation was increased with increasing urea concentration up to 3.0 M. Above 3.0 M, the effect of the urea concentration was weakened. Reaction temperature only affected the kinetics of precipitation. Figure 3.35 shows TEM images of representative precipitates derived from the solutions with different concentrations of urea [159].

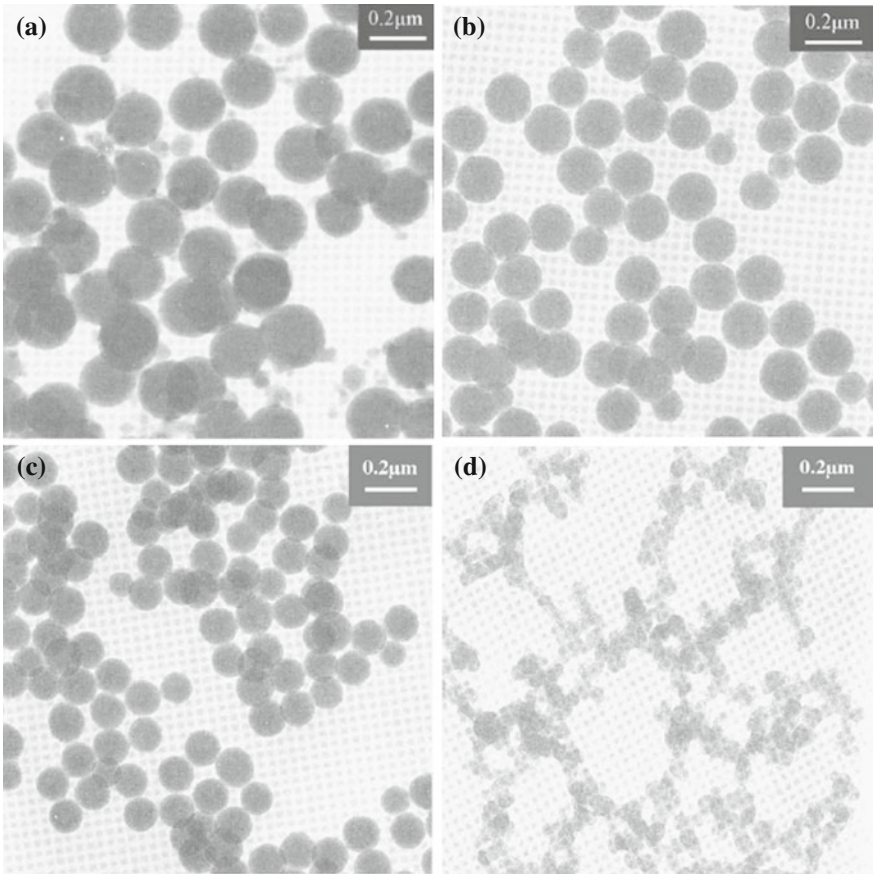

Fig. 3.35 TEM micrographs of yttrium compound prepared under different urea concentrations as **a** 0.04 M, **b** 0.5 M, **c** 2.0 M and **d** 7.0 M. The yttrium concentration and pH value were fixed at 0.02 and 6.0, while the reaction temperature was 95 ± 1 °C. Reproduced with permission from [159]. Copyright © 2004, Elsevier

Arrhenius-type reaction kinetics was used to estimate the activation energy of the precipitation reaction, resulting in a value of about 29 kcal mol^{-1}, which is comparable with the activation energies of urea decomposition, i.e., 28–32 kcal mol^{-1}. Therefore, the urea decomposition was a rate-determining step in the formation of the yttria particles for the homogeneous precipitation method. Particle morphology and the reaction kinetics were also influenced by pH value of the solutions. Low pH values, e.g., <2.0, particles showed severe agglomeration and the rate of precipitation reaction was slow. As the pH value was higher 3.0, near-monodisperse yttria particles could be achieved [159].

Complex oxides, such as YAG, spinel, mullite and ferroelectrics, contain more than one type of metallic element in their chemical formula [140, 160–175]. In this

case, chemical precipitation is also called coprecipitation. Chemical coprecipitation is also applicable to simple oxides with various dopants [138, 139, 142, 144, 145, 176, 177]. The solutions for coprecipitation can be formed with mixed salts (including chlorides, nitrates and acetates), mixed alkoxides, or combinations of salts and alkoxides. The types of the anions can be different, but in most cases, they are same. The co-precipitated precursors have high level homogeneity and thus can be converted to complex oxide powders at temperatures that are much lower than that required by the conventional solid-state reaction method. One of the problems encountered in coprecipitation is the difference in hydrolysis rate of the different reactants in the solution, which leads to segregation of the precipitated materials. However, this problem can be readily addressed by controlling the conditions to achieve homogeneous precipitation.

Monodispersed yttrium aluminum garnet (YAG) powders have been synthesized by using a homogeneous precipitation method, from mixed solutions of yttrium nitrate, aluminum nitrate and ammonium aluminum sulfate, with urea as precipitant [15]. The focus of this study was on the effect of the molar ratio of aluminum precursors, i.e., aluminum nitrate to ammonium aluminum sulfate. It was found this molar ratio showed a significant effect on morphology and particle size of the precipitated powders. Spherical precipitate particles could be obtained when the molar ratio was 1:1. During the homogeneous precipitation process, aluminum ions were precipitated first in the form of monodispersed spherical particles. After that, yttrium ions were precipitated on the surface of the aluminum sphere particles. Monodispersed spherical YAG particles with a diameter of 500 nm were obtained by calcining the precipitated powder at 1100 °C for 5 h. The monodispersed spherical Nd:YAG powders showed high sinterability. Transparent YAG ceramics have been obtained after vacuum sintering at 1650 °C for 3.5 h. Figure 3.36 shows SEM images of the precipitates from the solutions with different molar ratios of aluminum nitrate to ammonium aluminum sulfate.

Hydrothermal Synthesis

Precipitation from solution under hydrothermal conditions has been widely used for the synthesis of fine crystalline particles of various oxides [178–180]. The process involves heating reactants, such as metal salts, oxide, hydroxide, or even metal powder, in the form of solution or suspension, at certain temperatures. Water is the most widely used solvent. In this case, the precipitation temperatures are set between the boiling and critical points of water, i.e., 100–374 °C, while the pressures are up to 22.1 MPa, which is the vapor pressure of water at the critical point. Due to the presence of high pressures, hardened steel autoclaves are usually used to carry out hydrothermal reactions. The autoclaves have inner surfaces of which are lined with a plastic, such as Teflon, to prevent corrosion of the vessels. Similar to chemical precipitation method, hydrothermal synthesis also offers almost unlimited flexibility in combination of types and concentrations of starting reactants, additives, pH levels, temperatures, time durations, and so on.

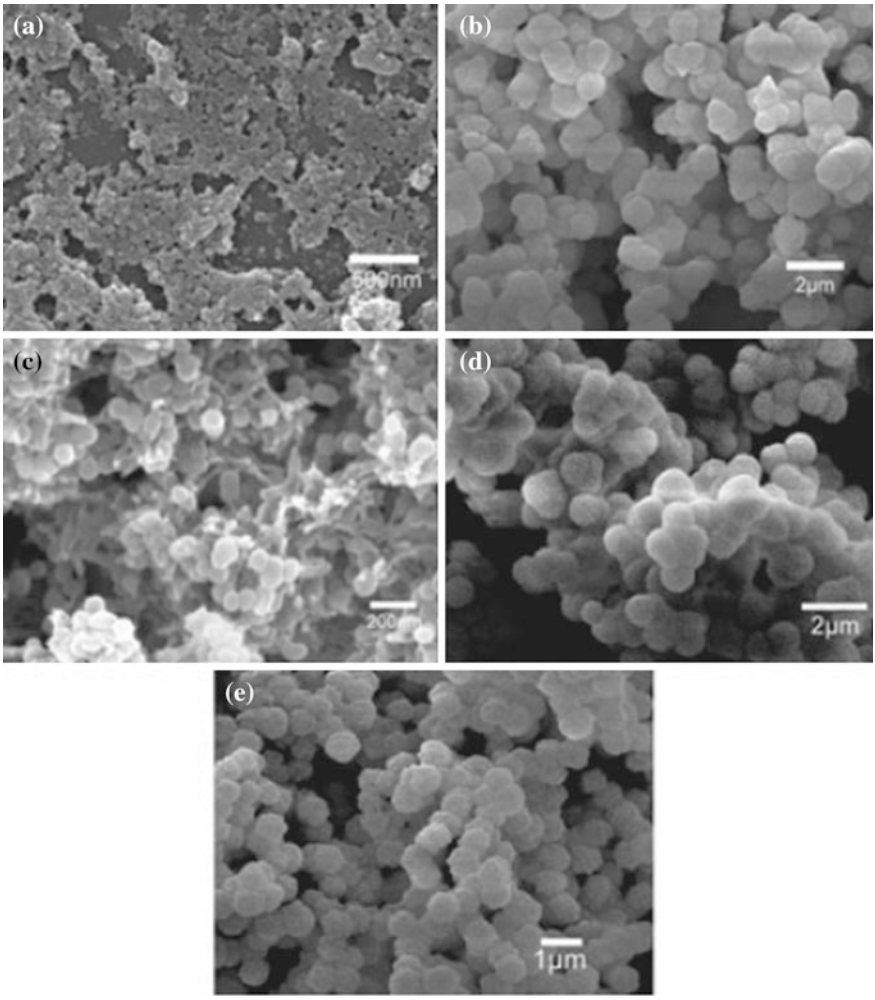

Fig. 3.36 SEM images of the precipitates from the solutions with different molar ratios of aluminum nitrate and ammonium aluminum sulfate: **a** 0.005:0, **b** 0:0.005, **c** 0.0033:0.0017, **d** 0.0017:0.0033 and **e** 0.0025:0.0025. Reproduced with permission from [15]. Copyright © 2012, John Wiley & Sons

Hydrothermal synthesis of $BaTiO_3$ powders has been extensively studied [181–186]. One example is to use the reaction between TiO_2 gels or fine anatase particles and $Ba(OH)_2$ in a strongly alkaline solution (pH 12–13) at 150–200 °C. The reaction mechanisms have been discussed in detail [187]. Depending on the reaction time and temperature, particles with average sizes in the range of 50–200 nm can be obtained. An alternative method is the crystallization of an amorphous gel of barium titanium acetate in a strongly alkaline solution of tetramethyl-ammonium

hydroxide at 150 °C for 10–15 h. The process involves dissolution of the gel and precipitation of crystalline $BaTiO_3$ particles, coupled with Ostwald ripening of the particles, leading to $BaTiO_3$ with weak agglomeration and average particle sizes of 200–300 nm.

Powders synthesized by hydrothermal synthesis are crystallized phases, so that the calcination step is not required, which is different from the normal solution precipitation. The powders also have very fine particle/grain size (10–100 nm), narrow size distribution, single crystal particles, high purity, and good chemical homogeneity. However, the application of hydrothermal precipitation to synthesize transparent ceramic powders is still not very popular, which deserves further exploration. Several examples are presented as follows [188–192].

One example of hydrothermal synthesis is the preparation of Al_2O_3 powders [147, 188]. α-Al_2O_3 powders and α-Al_2O_3/γ-AlOOH mixtures with controlled contents of γ-AlOOH have been synthesized by using a hydrothermal synthesis [188]. This is a very comprehensive study. First, the hydrothermal reactions were conducted under alkaline or acidic conditions at 380–435 °C for 1–10 days, at pressures of 6.9–14.5 MPa, with concentrated precursors without stirring. Second, the precursors were formed by mixing various types of aluminum hydroxides with water, and optionally with α-Al_2O_3 seeds, hydrogen peroxide, sulfuric acid, dopants (i.e., $KMnO_4$), and/or other additives. Third, all the experiments were performed at industrial scale by using large production autoclaves.

Furthermore, the synthesized α-Al_2O_3 powders possessed up to 100 % phase purity, 99.98 % chemical purity, equiaxed morphology, low aggregation levels, narrow crystallite size distributions, with primary particle sizes ranging between 100 and 40 μm, as well as high reproducibility. It was clarified that, various parameters, including types of precursors, the use and properties of seeds, chemical additives, as well as reaction temperature and time duration of the hydrothermal synthesis, could be used to govern the properties of the final powders.

Different growth mechanisms for the growth of nanosized and rough powders were observed. The rough α-Al_2O_3 was developed by vapor phase transport and/or surface diffusion from the γ-AlOOH intermediate particles, while the submicrometer α-Al_2O_3 was formed by assembly of nanosized building blocks, resulting in crystallographically ideal mesocrystals. Figure 3.37 shows SEM images of representative samples derived from the hydrothermal synthesis under different conditions. It is believed that α-Al_2O_3 powders prepared through optimization of the hydrothermal synthesis should be suitable for fabrication of high quality transparent alumina ceramics.

Hydrothermal synthesis has also been used to prepare rare earth oxides, (Y_2O_3–Gd_2O_3):Eu^{3+} and Y_2O_3:(Yb^{3+}/Er^{3+}), which were used for phosphors applications [189]. The simple hydrothermal method can be used to control the 1D and 2D nanostructures of the oxides. The reaction was a conversion of nitrates mixture into carbonate hydrate phase, with the presence of ammonium hydrogen carbonate solution, at a reaction temperature of 200 °C for 3 h. Morphological architectures of the rare earth oxides obtained were controlled by the thermal treatment at

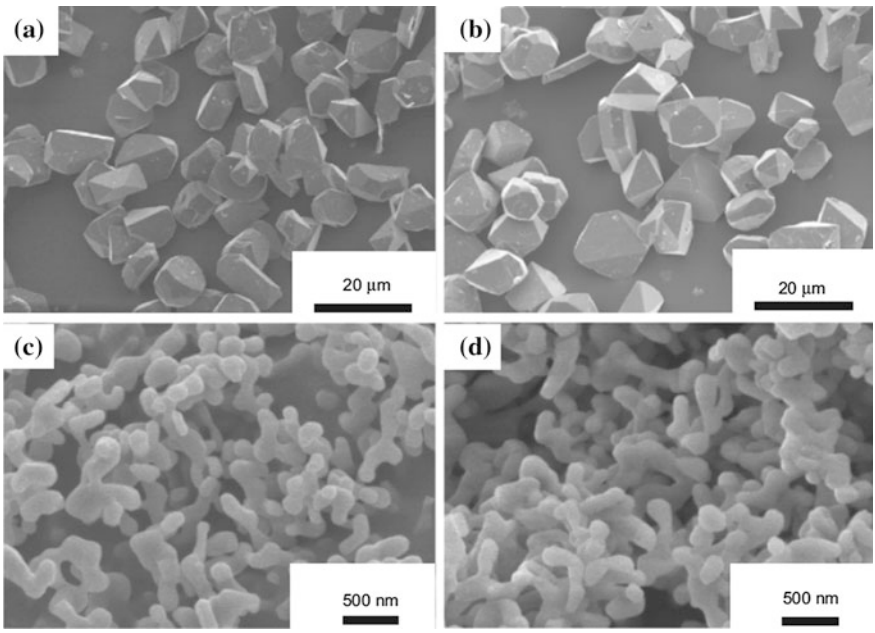

Fig. 3.37 SEM images of the hydrothermally synthesized phase-pure α-Al_2O_3 powders: **a** undoped 10 mm (Exp. No. 3), **b** Mn-doped 10 mm (Exp. No. 6), **c** undoped 250 nm (Exp. No. 9), **d** Mn-doped 250 nm (Exp. No. 11). All powders were in as-synthesized form. The Exp. Nos. can be found in the original reference. Reproduced with permission from [188]. Copyright © 2010, John Wiley & Sons

temperatures of 600–1100 °C and time durations of 3–12 h. The obtained powders exhibited high purity and homogeneous dopants distribution.

Another example is the synthesis of YAG:Ce (5 %) phosphors [190]. The hydrothermal reaction was carried out at 360 °C for various time durations, 6–26 h. Single-phase YAG:Ce (5 %) was obtained. The powder with reaction time of 22 h was treated by using spark plasma sintering (SPS) in vacuum and in air. No attempt was made to prepare transparent ceramics with the hydrothermally synthesized powders. However, these data could be used as a reference, if one wishes to employ hydrothermal synthesis to produce powders for transparent ceramics.

Core–Shell Structures

Coated particles, known as composite particles, are comprised of particles of one solid that are coated uniformly with a layer of another material, which have varying thickness, depending on composition requirement and other properties of the coated and coating phases [193–196]. Coated particles have several interesting advantages in terms of ceramic powder processing. For example, the presence of thin coatings

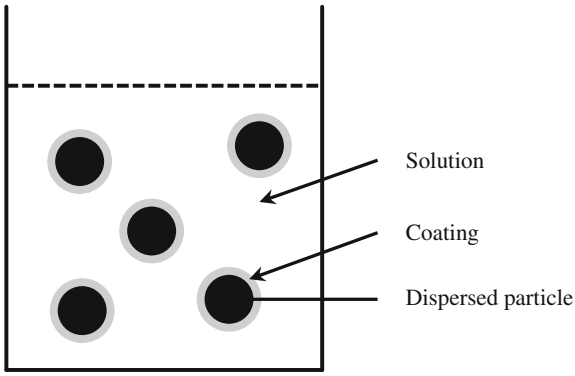

Fig. 3.38 Schematic of the preparation of coated particles by the precipitation from solution onto dispersed particles. Produced with permission from [5]. Copyright © 2003, CRC Press

is able to modify surface characteristics of colloidal dispersions, which allow for uniform incorporation of additives such as sintering aids and dopants. Particles coated with thick layers have significantly enhanced sintering behavior. This is particularly useful to fabrication of ceramic composites and synthesis of complex oxides.

There are several techniques that have been used to prepare coated particles, with a schematic shown in Fig. 3.38 [5]. Desirable coatings on particles can be achieved by controlling several parameters to facilitate proper interaction between the particulate suspension (A) and the material (B) that is to be precipitated on it from the solution [197].

Four types of A–B interactions could be observed in experiments. (i) B nuclei are formed homogeneously in the solution and then grow to form particles that have no interaction with A, which thus leads to particles of simple mixtures of A and B. (ii) Particles of B are homogeneously nucleated, which have weak interaction with particles of A and then deposit on A particles, but with rough and nonuniform morphology, especially when the B particles have large sizes. (iii) Homogeneously nucleated particles of B have weak interaction with particles of A at an early stage to form aggregates, on which the particles of B continuously grow, thus producing a particulate coating of B on A. The coating could be more homogeneous than that in case (ii), especially when the B particles are much smaller than the A particles. (iv) B particles are nucleated heterogeneously on surface of A particles, so that a uniform layer of B on A due to the growth of the B nuclei. This is the most desirable case, because smooth and uniform coatings can be formed.

There are several requirements that should be satisfied, in order to produce coated particles with uniform and smooth coating layers in the above case (iv). First, the nucleation and growth steps must be separated. Figure 3.39 shows a modified LaMer diagram for homogeneous precipitation of monodispersed particles [5]. The curve "a" in Fig. 3.39 is the case of a single burst of homogeneous nucleation followed by growth. When the A particles are present in the solution, heterogeneous nucleation of B can be triggered on their surfaces, when the solute concentration reaches C_h, which is the critical concentration for heterogeneous

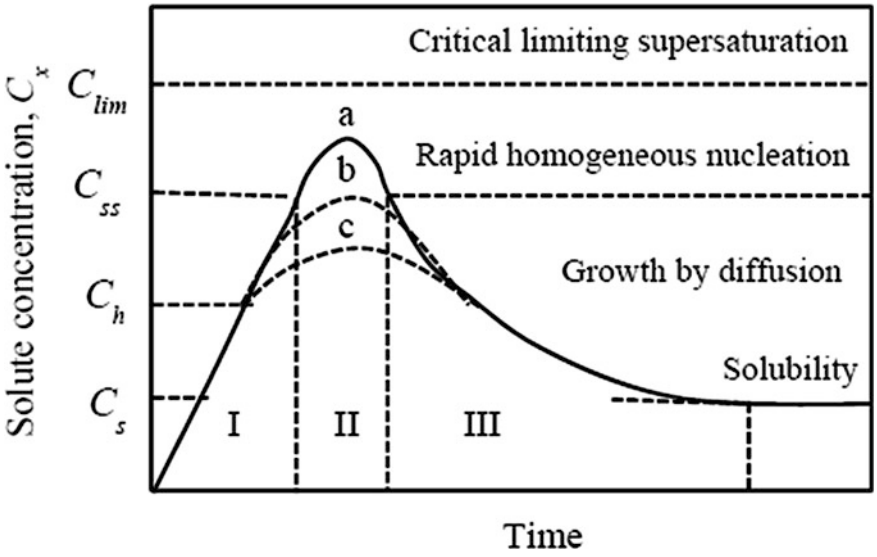

Fig. 3.39 Modified LaMer diagram for the formation of coated particles by precipitation from solution. Produced with permission from [5]. Copyright © 2003, CRC Press

nucleation. To produce coated particles with uniform coating layers, the presence of one rapid burst of heterogeneous nucleation, i.e., curve "c" in the figure, without reaching C_{ss} is a critical requirement.

Second, colloidal stability of the dispersion is important. During the nucleation and growth, the dispersion must be stable against flocculation and settling, in order to obtain well-dispersed and uniformly coated particles. The newly formed surface layers during this stage are likely to act as binder to form agglomerates, which once formed will have destroy the stability of the dispersion system.

Third, surface area of the core particles must be sufficiently large, so that the concentration of the solute will never reach C_{ss}. Otherwise, free particles of B will be precipitated, besides the coated particles, which is corresponding to curve "b" in Fig. 3.39. The surface area of the core particles has a direct influence on the rate of generation of the solute (r_g) by the reaction (nucleation) and the rate of removal of the solute (r_r) by precipitation/coating. The minimum surface area of the core particles that is available for deposition, A_{min}, is closely related to the maximum concentration of the solute, C_{max}. For a given r_g and assuming that the suspensions are sufficiently concentrated so that the interface reaction is rate-controlling step, A_{min} is defined as:

$$r_g = KA_{min}(C_{ss} - C_s), \tag{3.41}$$

where K is a constant and $C_{max} = C_{ss}$. The maximum surface area for deposition, A_{max}, means that the concentration of the solute should exceed C_h, otherwise only

partial coating will be realized. As a result, the following equation must also be satisfied:

$$r_g = KA_{max}(C_h - C_s). \tag{3.42}$$

The maximum production rate and the latitude of the experimental conditions are then related to the maximum value of the ratio A_{max}/A_{min}. By equating Eqs. (3.41) and (3.42), there is:

$$\frac{A_{max}}{A_{min}} = 1 + \frac{C_{ss} - C_h}{C_h - C_s}. \tag{3.43}$$

In order to optimize the conditions, so that coating is formed in suspensions with high particle concentration, high production rates, and ease of processing, C_h should be as close as possible to C_s and C_{ss} and C_h should be separated as far as possible. This is because (i) C_h is close to C_s so that heterogeneous nucleation can start immediately after C_s is passed and (ii) C_{ss} is much greater than C_s so that homogeneous precipitation is far remote away from the onset of heterogeneous precipitation.

In practice, A_{min} is experimentally determined for a given r_g and for particles with a known size by decreasing the concentration of the particles in the suspension until precipitation occurs. For a low A_{min}, coating of the particles in a suspension should be highly possible, because $C_{ss} - C_s$ is relatively large, according to Eq. (3.41). If the conditions to prevent homogeneous precipitation cannot be achieves, it is possible to use catalyst to pretreat the surface of the particles. Various coated particles by using precipitation from solution have been reported in the literature [195, 198–205].

The degree of crystallinity of the deposited material can have a remarkable effect on morphology of the coating layers. In theory, the coatings can be amorphous, polycrystalline or even single crystal. Generally, smooth and uniform coatings are achieved more easily for amorphous coatings [194, 195], while polycrystalline deposits lead to rough layers [206]. However, even for amorphous layers, the morphology of the coatings can be controlled through adjusting experimental conditions. For example, when SiO_2 was coated on $Y(OH)CO_3$ particles at room temperature and at 80 °C, the coating was smooth and rough, respectively [207]. It means that precipitation temperature can be used as a factor that can affect morphology of the coatings.

Coated particle technique has been well employed to synthesize powders for transparent ceramics, especially for YAG. YAG powder retaining the morphology of Al_2O_3 powder has been synthesized by using a partial wet-chemical process, in order to form yttrium precipitate coated Al_2O_3 particles [208]. The formation of the so-called core–shell structure had two steps, including (i) direct precipitation of yttrium component at the surface of the Al_2O_3 particles and (ii) assembly of the yttrium precipitate. A spherical surface reaction process was illustrated. YAG phase

can be obtained at a temperature that was about 300 °C lower than those required by the traditional solid-state reaction process.

Y-containing colloidal precursor particles were first synthesized. $Y(NO_3)_3 \cdot 6H_2O$ (99.99 %) and urea were dissolved in distilled water to make a transparent solution, with Y^{3+} concentration of 0.015 M and urea concentration of 0.5 M. α-Al_2O_3 (99.99 %) powder was then added into the mixed solution, which was dispersed by using ultrasonication. The mixed turbid liquid with Y/Al = 3/5 was homogenized by agitation, which was then heated to 90 °C and kept at that temperature for 3 h. After cooling down, the resulting precursor was collected with suction filtration and thorough washing. After rinsing with anhydrous ethanol, the powder was dried at 100 °C for 24 h and then calcined at various temperatures for 3 h to form YAG.

Morphology of the α-Al_2O_3 powder and the as-obtained precipitated precursor were observed by suing TEM, as shown in Fig. 3.40 [208]. The pure α-Al_2O_3

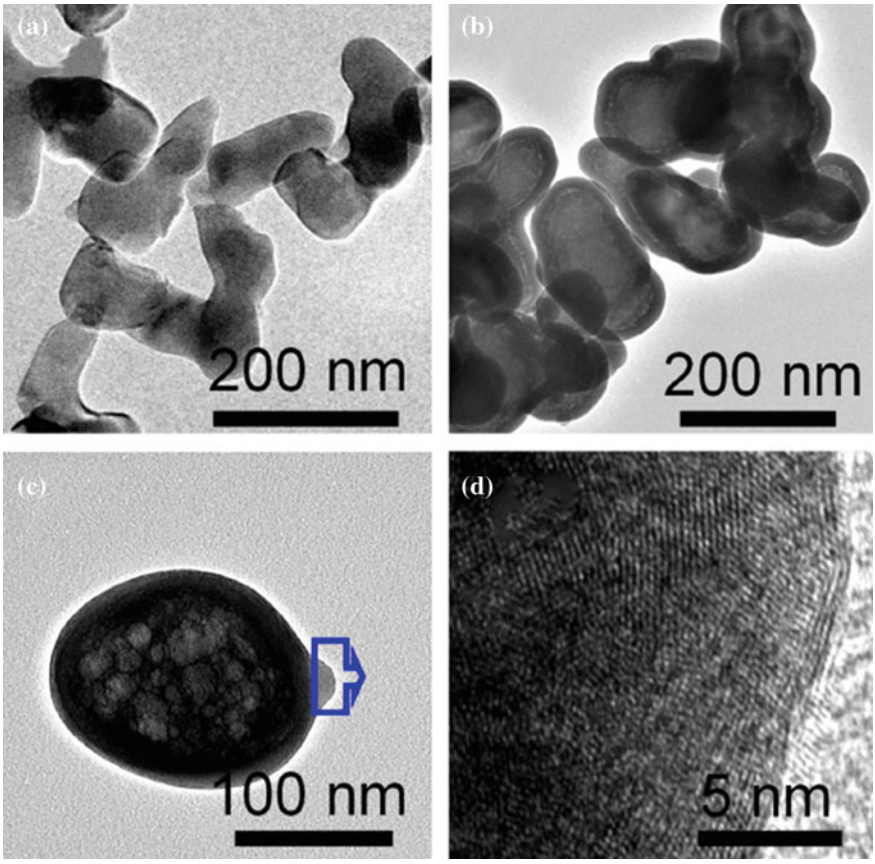

Fig. 3.40 TEM images of the precursors: **a** pure α-Al_2O_3, **b** Y-precipitate/Al_2O_3 with low electron exposure, **c** Y-precipitate/Al_2O_3 with high electron exposure and **d** the lattice image of the shell. Produced with permission from [208]. Copyright © 2013, Elsevier

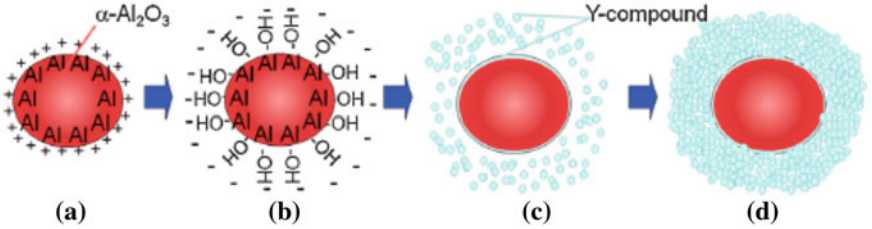

Fig. 3.41 Mechanism of the formation of the Y-precipitate/Al_2O_3 precursor in the urea solution. Produced with permission from [208]. Copyright © 2013, Elsevier

powder consisted of homogeneous particles with sizes of 100–200 nm. The powder was well crystallized with continuous and clear edges, as shown in Fig. 3.40a. The as-obtained precursor particles exhibited obvious interfaces between the core and the shell, as shown Fig. 3.40b. The Y-precipitate could be $Y(OH)CO_3$ or similar carbonate, which would decompose under the irradiation of the electrons. Figure 3.40d indicates that the compound of the shell had low crystallinity, consisting of tiny particles.

A potential mechanism for the formation process of the Y-precipitate/Al_2O_3 is shown in Fig. 3.41. Two stages were involved. At the initial stage, a thin layer of Y-compound was precipitated at the surface of the Al_2O_3 particles, so that the surface was modifies. At the second stage, explosive nucleation and assembly onto the Y-compound pre-coated Al_2O_3 particles occurred. In the presence of urea, there would be negative ions, such as OH^-, HCO_3^-, etc., which were adsorbed at the surface α-Al_2O_3, leading to negative zeta potential. The Y^{3+} ions were hydrated and adhered to the hydrolyzed Al_2O_3 surface to form yttrium hydroxide. Finally, a thin shell was formed.

Similarly, a mixed precipitation method was developed to synthesize powder for transparent YAG ceramics [172]. The YAG powders were obtained through calcining the precursors at 1050 °C for 2 h. Particle size of the powders was in the range of 200–500 nm. Yttrium nitrate hydrate ($Y(NO_3)_3{\cdot}H_2O$, purity >99.9 %), aluminum nitrate hydrate ($Al(NO_3)_3{\cdot}H_2O$, purity >99.9 %) and ammonium hydrogen carbonate (NH_4HCO_3, analytical reagent) were used as raw materials.

Flow chart of the mixed precipitation method is shown in Fig. 3.42. Briefly, alumina precursor powder was first synthesized by adding aluminum nitrate solution (0.15 M) dropwisely into the ammonium bicarbonate solution (1.5 M) under vigorous stirring. The as-prepared alumina precursor powder was then dispersed in yttrium nitrate solution to form uniform suspension. After that, ammonium bicarbonate solution (0.5 M) was added dropwisely into the suspension, so that yttrium precipitate was coated on the alumina precursor powder. The mixed precursor was aged, washed, dried, and then calcined to form yttrium aluminum garnet, with a phase formation temperature about 300 °C lower than that required by the traditional solid-state reaction process. Alternatively, it is also worth trying to coat yttria with alumina.

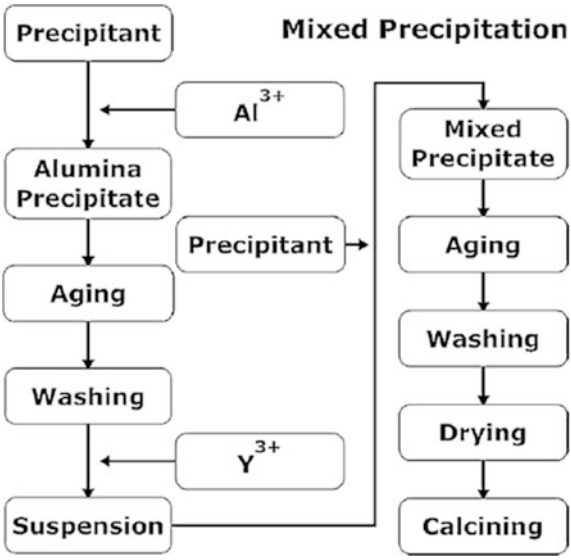

Fig. 3.42 Flow chart of the mixed precipitation process. Produced with permission from [172]. Copyright © 2012, Elsevier

3.2.2.2 Liquid Evaporation Methods

Evaporation of liquid is another method to make a solution to be supersaturated, so as to produce particles through the nucleation and growth. To synthesize powders with fine particles, nucleation must be fast and the growth is sufficiently slow. To achieve this, the supersaturation state must be reached in a very short time, so that a large number of nuclei are formed almost at the same time, without growing. Therefore, if a solution is broken into very tiny droplets, the surface area over which evaporation takes place can be increased tremendously. For solutions of two or more salts, the differences in concentration and solubility must be taken into account. This is because evaporation of such liquid solutions will cause different rates of precipitation for different salts, which will result in segregation of the final powders. The formation of very small droplets can be used to address this problem, because there is no mass transfer between individual droplets. Moreover, for a given size, the lower the concentration of the solutions, the smaller the particle size will be in the final powders. This means that the degree of segregation can be further decreased by using diluted solutions. Various techniques have been used to produce ceramic powders through the evaporation of liquid solutions.

Spray Drying

In spray drying, a solution is broken up into fine droplets by a fluid atomizer and sprayed into a drying chamber, as shown schematically in Fig. 3.43 [47]. Moisture is evaporated at the contacts between the spray and drying medium that is usually

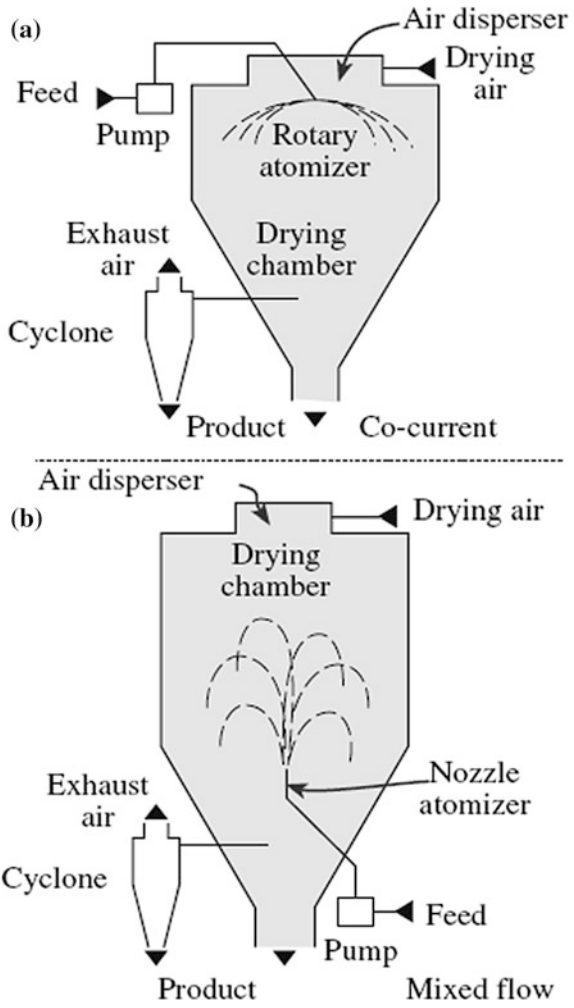

Fig. 3.43 Schematics of spray dryers: **a** centrifugal atomizer with concurrent air flow and **b** nozzle atomizer using mixed flow conditions. Reproduced with permission from [47]. Copyright © 2007, Springer

hot air. The products are dry particles of the metal salts, which are carried by the air stream to leave the chamber and are then collected by using bag collectors or cyclones. Various atomizers are available, which are usually categorized according to the manner in which energy is supplied to produce the droplets [209–211].

For example, in rotary atomization, also known as centrifugal atomization, the liquid is centrifugally accelerated to a high velocity through a spinning disk that is located at the top of the drying chamber, before it is discharged into the chamber. In pressure atomization, pressure nozzles atomize the solution by accelerating it through a large pressure difference and injecting the liquid into the chamber. Pneumatic atomization is to impact the solution by using a stream of high-speed gas from a nozzle. Ultrasonic atomization is to pass the solution over a piezoelectric

vibrator that is vibrating at ultrasonic frequencies. Droplet sizes ranging from less than 10 μm to >100 μm can be produced by these atomizers.

Solutions for spray drying are usually aqueous solutions of metal salts, such as sulfates, chlorides and nitrides, due to their high water solubility. The evaporation rate of moisture from the droplet and the maximum temperature of generally >300 °C that the particles will experience in the drying chamber are determined by the temperature and flow pattern of the hot air, as well as the configuration of the chamber. Important solution parameters include the size of the droplets and the concentration and composition of the metal salts, which are dominant factors in controlling the size of the primary particles and the size and morphology of possible agglomerates. Morphology of the agglomerate is not very critical in spray drying of solutions, because the particle characteristics are mainly determined by the subsequent calcination and milling steps. With suitable conditions, the agglomerates are usually spherical, with primary particle sizes of <100 nm. The temperature in the drying chamber of spray is generally not sufficiently high to cause decomposition or solid-state chemical reaction, so spray-dried salt powders must be calcined to form designed compounds [211–215].

A simple strategy has been reported to prepare dense spherical Y_2O_3:Eu^{3+} phosphor particles with a narrow size distribution, by using a two-step spray drying, with a commercially available spray drying facility [216]. Hollow Y_2O_3:Eu^{3+} precursor particles were first prepared by spray drying an aqueous precursor solution containing citric acid. Nanosized particles were obtained from the precursor powders by using ball milling, which were then dispersed in water to form a colloidal suspension. The suspension was subjected to second-step spray drying, so that porous granules of dense spherical nanoparticles could be formed. Finally, highly crystalline Y_2O_3:Eu^{3+} powder was prepared by sintering the granules at temperatures of >1200 °C. The final Y_2O_3:Eu^{3+} particles were spherical and showed promising luminescence properties as a red phosphor. SEM images of representative samples are shown in Fig. 3.44.

Spray Pyrolysis

If a higher temperature and a reactive (e.g., oxidizing) atmosphere are used in the spray chamber, solutions of metal salts can be not only dried but also decomposed at the same time. This process is known as various names, such as spray pyrolysis, spray roasting, spray reaction and evaporative decomposition of solutions, among which spray pyrolysis is the most commonly used [217–223].

Figure 3.45 shows a schematic demonstrating the idealized stages involved in the formation of a dense particle from a droplet of solution [224, 225]. The droplet experiences evaporation, when the solute concentration in the outer layer increases to a value of above the supersaturation limit, thus resulting in the precipitation of fine particles. Precipitation is followed by a drying stage, in which the vapor phase diffuses through the pores in the precipitated layer. Decomposition of the

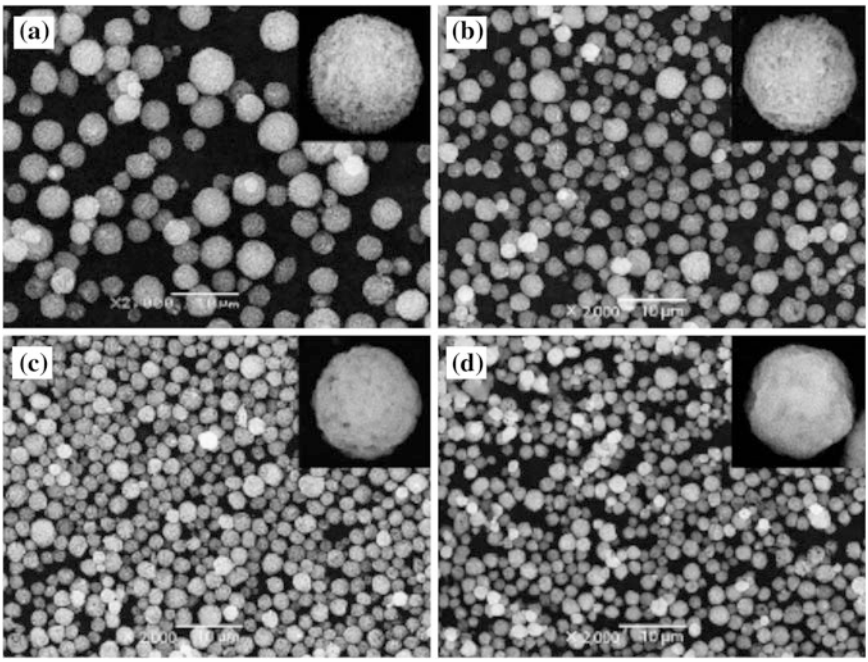

Fig. 3.44 SEM images of the **a** Y_2O_3:Eu^{3+} powders prepared by second-step spray drying process, and post-treated Y_2O_3:Eu^{3+} powders at the temperature of **b** 1200 °C, **c** 1300 °C, and **d** 1400 °C. Reproduced with permission from [216]. Copyright © 2014, The Royal Society of Chemistry

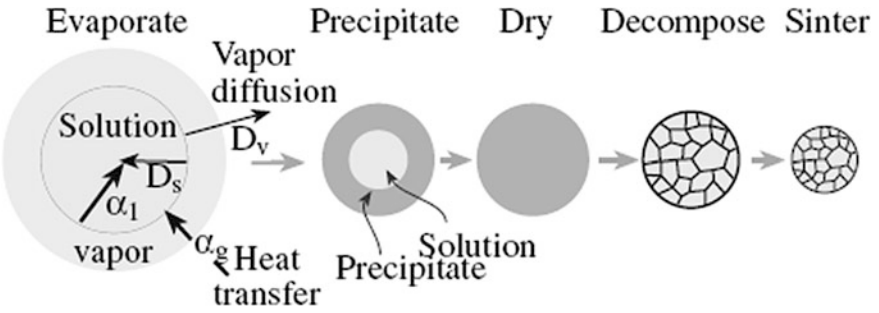

Fig. 3.45 Schematic of the stages in the spray pyrolysis process. Reproduced with permission from [224], Copyright © 1993, John Wiley & Sons. Reused with permission from [47]. Copyright © 2007, Springer

precipitated salts leads to a porous particle consisting of a certain number of very fine grains, which is finally heated to become a dense particle.

The spray pyrolysis process is able to produce particles with a variety of morphologies through controlling the experimental conditions. For the fabrication of

transparent ceramics, dense particles are superior to those with highly porous or hollow shell-like morphologies, because a subsequent milling step is normally unnecessary. As a result, there will be less chance to introduce possible contamination.

The effects of the conditions on precipitation in the droplet and the solution chemistry on the morphology and microstructure of the final particles have been well investigated [224]. In order to obtain dense particles, the first step is to achieve homogeneous nucleation and growth in the droplet, which is known as volume precipitation. The prerequisite is a small droplet size and a slow drying process, so as to reduce the gradients in solute concentration and temperature. As mentioned earlier, a large difference between the supersaturation concentration C_{ss} and the saturation concentration C_s of the solute in solution means a high nucleation rate, as demonstrated in Fig. 3.39 and Eq. (3.25). A high C_s, i.e., a high solute solubility, and a positive temperature coefficient of solute solubility are also important, because there will be sufficient solute available to form filled agglomerates of the touching primary particles in this case. In addition, the precipitated particles should not be thermoplastic or melt during the decomposition stage, otherwise, they will be deformed and morphology will be negatively affected.

It is also found that multicomponent and composite particles with a variety of microstructural characteristics can be synthesized by controlling the spray conditions. The drying of a droplet containing fine precipitates is quite different from that of a pure liquid droplet. The fine precipitates act a resistance to the mass transport of the solvent vapor. As the temperature of the drying chamber is too high, boiling of the solution might occur, which leads to inflation or disintegration of the droplets. Moreover, high capillary stresses and fracture of the particle could be observed, if the fine pores inside the precipitates are combined and the drying rate of the droplet is too fast.

The dried salts must be completely decomposed before they are brought to the final sintering process. For small scale laboratory experiments, decomposition times are relatively short, nitrates and acetates are preferable to sulfates, due to their lower decomposition temperatures. In addition, acetates have a low solubility, while nitrates, acetates, and sulfates are easy to introduce impurities into the final powder. On the other hand, chlorides and oxychlorides are more likely used for industrial productions, owing to their high solubilities. However, the corrosive nature of the gases produced during the decomposition and the deleterious effect of residual chlorine on subsequent sintering should be considered carefully. It is better to sinter the particles in situ, so as to take full advantage of the spray pyrolysis process. If the process in conducted at a sufficiently high temperature, the fine pores between the primary particles and the short interparticle collision time in the process are beneficial to the formation of dense individual particles.

Nano-sized MgO particles with well-crystallized structures have been prepared by using spray pyrolysis method with solutions of citric acid [219]. The optimum concentration of citric acid was 0.4 M, in order to obtain micrometer-sized MgO particles. The function of citric acid in the spray solution was to alter the thermal properties of the solution and thus to control the morphologies of the particles. The micrometer-sized precursor particles with hollow porous structures which were

obtained through the spray pyrolysis step could be broken into nano-sized MgO particles by using a post-treatment. Without the presence of critic acid, the average sizes of the MgO particles thermally treated at temperatures of 500 and 900 °C were 13 and 28 nm, respectively. If citric acid was added into the spray solutions, the average particle sized were decreased correspondingly to 9 and 22 nm.

A systematic study has been reported on the comparison between spray pyrolysis and solid-state reaction method to prepare YAG powders [222]. The influence of precursor characteristics and synthesis conditions on the formation of yttrium aluminum garnet, $Y_3Al_5O_{12}$(YAG), was investigated. Two types of sources were used in this study: (i) single-source precursors, i.e., cohydrolyzed yttrium and aluminum alkoxides and yttrium aluminum glycolates, and (ii) multiple-source precursors, i.e., mixtures of metal nitrates and mixtures of separately hydrolyzed yttrium and aluminum alkoxides. Phase-pure YAG was formed only in the solid-state thermal decomposition experiments. The lack of formation of YAG in all the spray pyrolysis experiments was ascribed to the short heating times and fast heating rates, which resulted in the formation of kinetic products. In the case of the metal nitrates, an additional factor that influenced product formation was the difference in thermal reactivity of the precursors. It was concluded that the formation of complex metal oxide materials by conventional or aerosol routes is not necessarily achieved by the use of a chemically homogeneous precursor, such as a single-source precursor. It also was necessary to ensure that the precursors and intermediates have similar thermal decomposition temperatures to avoid phase segregation in the initial stages of thermal decomposition.

A series of works have been reported on preparation of YAG based phosphor powders by using spray pyrolysis method, with spray solutions of different fluxes [226–229]. It has been demonstrated that spray pyrolysis method can be used to control the morphologies and sizes of the YAG based phosphor powders in a very feasible way. Highly spherical particles with well controlled size distribution can be readily synthesized by optimizing the processing parameters.

Another example is the synthesis of YAG:Ce phosphor powders, with a composition of $Y_{2.965}Al_5O_{12}$:$Ce_{0.035}$, by using spray pyrolysis, from spray solutions with BaF_2 flux [228]. The BaF_2 flux has been show feasible control in morphology and improvement in optical properties of the YAG:Ce phosphor powders. The optimal concentration was 9 wt% BaF_2 flux, which resulted in powders with regular morphology and without aggregation. The average size of the YAG:Ce phosphor powders was 1.73 μm.

A 1.7 MHz ultrasonic spray generator having six vibrators was used to generate sufficient droplets. The spray pyrolysis was carried out with flowing air as carrier gas at a flow rate of 40 L min^{-1}, at reaction temperature of 900 °C. The powders were stayed inside the reactor for 0.6 s. The overall solution concentration was 0.5 M, while concentrations of the BaF_2 flux were in the range of 3–15 wt% of YAG:Ce. All the as-prepared powders were post-treated at temperatures of 1300–1600 °C for 5 h in 10 % H_2/N_2 gas mixture. Figure 3.46 shows SEM images of representative samples. All the as-prepared powders showed a spherical shape and a dense structure, with an average particle size in the range of several micron meters,

which was not significantly affected by the concentration of the BaF_2 flux. After thermally annealed at 1500 °C, the spherical shape of the powders was deformed. However, the powders derived from the solution without BaF_2 flux demonstrated higher agglomeration, while the particle size of the powders increased with increasing concentration of BaF_2. In terms of powder morphology, the optimal concentration of BaF_2 was 9 wt%.

Freeze-Drying

Similar to that in spray drying, in freeze-drying, a solution of metal salt is also broken up by an atomizer into fine droplets in the first step [230–232]. In contrast to spray dry or spray pyrolysis, in which high temperature is used, in freeze-drying, the droplets are frozen rapidly, by spraying them into a cold bath of immiscible liquid, such as hexane and dry ice or liquid nitrogen. The frozen droplets are then transferred into a cooled vacuum chamber, where the solvent is removed through vacuum evaporation. In some cases, the system needs to be heated slightly to aid the sublimation. Generally, spherical agglomerates of fine primary particles can be produced, with the agglomerate size to be the same as that of the frozen droplets. The size of the primary particles, in the range of 10–500 nm, is determined by the processing parameters, including the rate of freezing, the concentration of the metal salt in the solution, and the chemical composition of the salt. After the drying process, the powder of the salt is heated at high temperatures to obtain oxides.

Generally, the solubility of most salts decreases with decreasing temperature, so that the supersaturation state can be rapidly reached during the rapid cooling of the droplets in freeze-drying. In this case, particle nucleation is very fast while growth is very slow. As a result, freeze-drying is able to produce powder with very fine particle sizes. In this respect, freeze-drying is more efficient in producing fine particles than the other spray drying techniques, as demonstrated in various materials, including Al_2O_3 [233], Y_2O_3 [234], ZrO_2 [235–237], $MgAl_2O_4$ [238–241], YAG [7, 140, 242, 243] and mullite [244]. Selected examples are discussed in a more detailed way as follows.

High sinterability $MgAl_2O_4$ powder has been produced from alkoxide precursors by using a freeze-drying method, with clear alumina sol and magnesium methoxide as starting materials [241]. The tap density and sinterability of the spinel power are affected by the ball milling step. Highly dense transparent polycrystalline $MgAl_20_4$ ceramics were prepared from the powders by sintering and hot isostatic pressing (HIP).

The alumina sol was prepared from aluminum isopropoxide through hydrolysis and peptization, while magnesium methoxide was prepared through the reaction of magnesium pieces (99.99 %) in excessive methanol under reflux in an N_2 atmosphere for 24 h. The spinel sol was prepared by slowly mixing the alumina sol into a methanol solution of magnesium methoxide in stoichiometric composition so as to form spinel $MgAl_2O_4$. The spinel sol was then heated at 85 °C for 2 days to evaporate excessive water and organic solvents, which was then sprayed into a tray

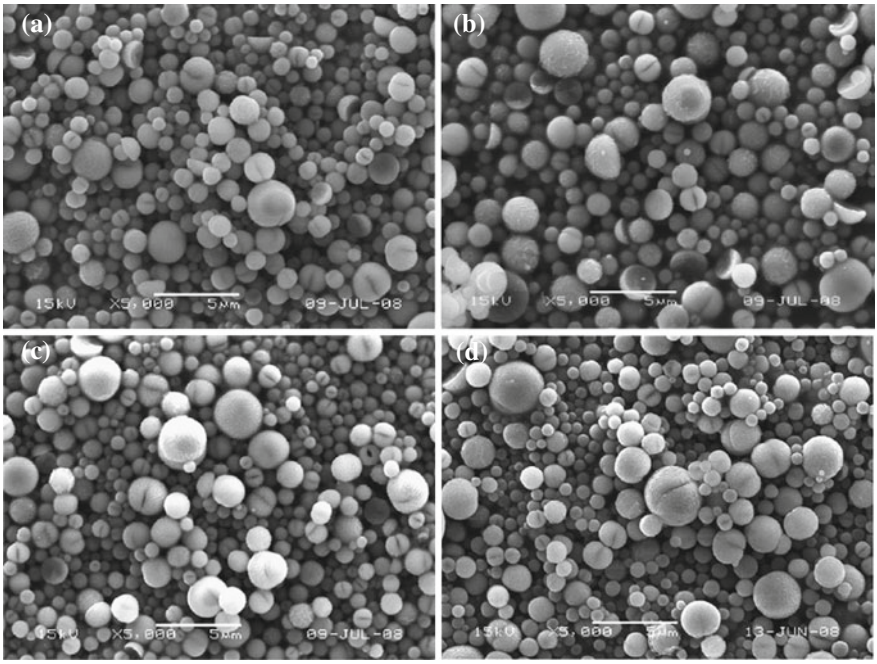

Fig. 3.46 SEM images of the precursor powders prepared by using the spray pyrolysis with and without the use of BaF_2 flux: **a** no flux, **b** BaF_2 = 3 wt%, **c** BaF_2 = 9 wt% and **d** BaF_2 = 15 wt%. Reproduced with permission from [228]. Copyright © 2009, Elsevier

containing liquid nitrogen through a two-fluid nozzle. After the freeze spraying, the frozen beads of spinel sol were loaded into a laboratory freeze-dryer with a tray dryer attachment, which was then gradually heated to 50 °C under 60 mTorr, i.e., ~8.0 Pa, until all the ice sublimed. The freeze-dried powder was calcined to for spinel phase. The spinel powders were then deagglomerated by wet- and dry milling steps with plastic bottles and yttria-stabilized-zirconia (YSZ) ceramic balls for 24 h.

Figure 3.47 shows XRD patterns of the as-freeze-dried powder and those calcined at different temperatures for 2 h are [241]. The as-freeze-dried powder consisted of a mixture of AlO(OH) and $MgAl_2(OH)_8$. Calcination at 900 °C resulted in the formation of spinel phase, while complete crystallization was observed after calcination at 1200 °C. The powder calcined at 1100 °C had an average particle size of about 50 nm.

Another example is the synthesis of Nd:Y_2O_3 nanosized powder by using freeze-drying, which was then mixed with commercial Al_2O_3 power to fabricate Nd:YAG transparent ceramics [7]. Yttrium nitrate hexahydrate, $Y(NO_3)_3{\cdot}6H_2O$, and neodymium nitrate hexahydrate, $Nd(NO_3)_3{\cdot}6H_2O$, both with purity of ≥99.99 %, were used as starting materials, while ammonium hydrogen carbonate, NH_4HCO_3, was used as precipitant. Aqueous solution with 0.25 M Y^{3+} and 2 at.% Nd^{3+} was

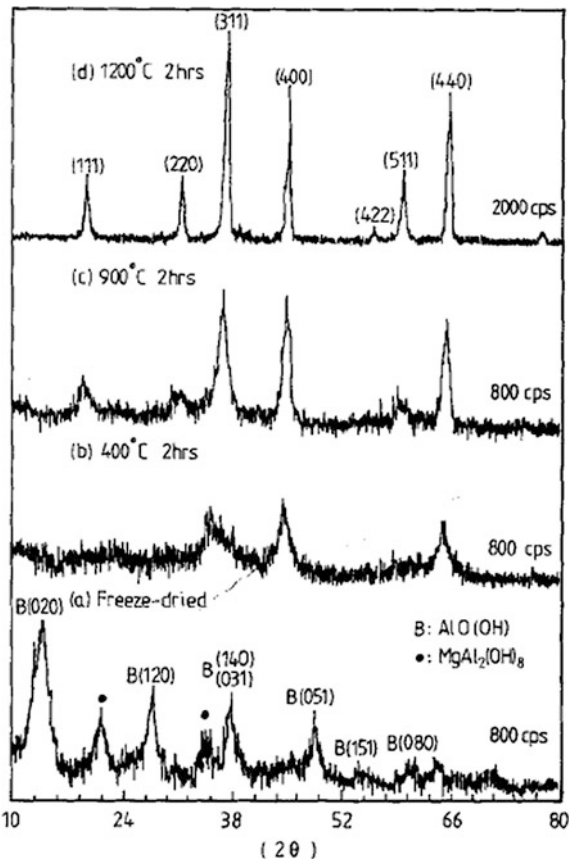

Fig. 3.47 XRD patterns of the as-prepared powder and the powders calcined at different temperatures. Reproduced with permission from [241]. Copyright © 1992, John Wiley & Sons

prepared by dissolving the metal nitrates in deionized water. After that, 2 M NH_4HCO_3 aqueous solution was added dropwisely into the metallic ion solution under mild agitation at room temperature. White precipitate was formed during the mixing. After aging for 2 days, the precipitate was washed thoroughly with deionized water, which was then frozen and dried through freeze-drying at −80 °C and 0.03 Torr. Nd:Y_2O_3 ultrafine powders were obtained by calcining the freeze-dried precipitates in air at temperatures of 500–1,100 °C for 4 h at a heating rate of 3 °C min^{-1}. Figure 3.48 shows SEM images of the powders after calcining at different temperatures. As the calcination temperature was increased from 900 to 1100 °C, the average particle size increased from ∼25 to ∼40 nm, without the presence of severe agglomeration. In contrast, the powders calcined by using normal furnace were heavily agglomerated. Highly transparent 2 at.% Nd:YAG ceramics were obtained from the freeze-drying derived Nd:Y_2O_3 powders and commercial Al_2O_3 powders by using vacuum sintering at 1750 °C for 5 h. Similar freeze-drying process was used to synthesis nanosized Nd:YAG powder to prepared transparent Nd:YAG ceramics [242, 243].

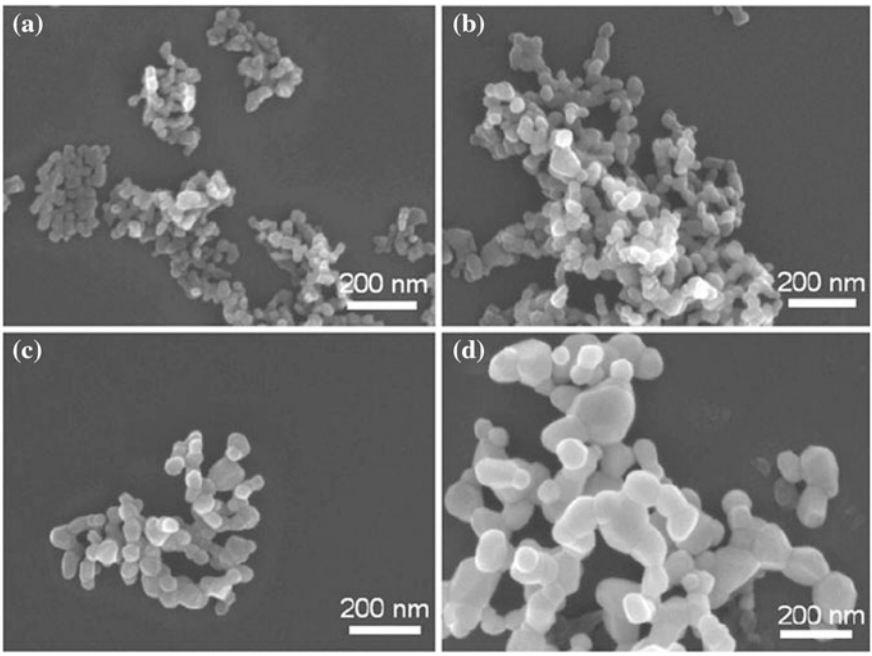

Fig. 3.48 SEM images of the freeze-dried power calcined at different temperatures: **a** 900 °C, **b** 1000°, **c** 1100 °C and **d** 1200 °C. Reproduced with permission from [7]. Copyright © 2011, Springer

Spray Drying of Suspensions

Spray drying is also applicable to suspensions of fine particles, which is usually knows as slurries, when they have relatively high concentrations. The key of this process is to limit the agglomeration of the dried powder to a scale that is equal to or less than the size of the droplet. Minimizing the degree of the agglomeration is required by the subsequent compaction and sintering steps [25, 245–250]. Spray drying of suspensions is used on a large scale industrially for granulating fine powders to control their flow and compaction characteristics during die pressing. Therefore, if large scale fabrication of transparent ceramics is considered, this technique will be very useful.

One earlier example is regard to Al_2O_3 transparent ceramics [251]. Both spray drying and freeze-drying processes were used and compared. The starting raw materials were reagent grade α- and γ- Al_2O_3 and magnesium sulfate as dopants. The impurities detected, such as copper, silicon, sodium and calcium, were less than 10 ppm. The α- Al_2O_3 had a surface area of 2 $m^2\ g^{-1}$ with an average grain size of 8 μm, while the γ- Al_2O_3 a possessed a surface area of 94 $m^2\ g^{-1}$ with an average grain size of 0.2 μm. The powders contained 0.25 wt% of MgO. The Al_2O_3 colloidal dispersions were made with Al_2O_3 contents of 10 wt%, required amount of

magnesium sulfate for 0.25 wt% MgO. Stable colloidal dispersions could be obtained at pH = 2.5–3. Experimental results indicated that both types of powders, which were processed by both spray drying and freeze-drying, could be sintered to near theoretical density, with high optical transparency.

A study has been conducted to optimize the spray drying parameters in order to prepare transparent Yb:YAG ceramics [215]. Commercial oxides were used as the starting materials, with compositions of $Yb_{0.03}Y_{2.97}Al_5O_{12}$ and $Yb_{0.294}Y_{2.706}Al_5O_{12}$, corresponding to YAG doped with 1.0 and 9.8 at.% of Yb, respectively. The effects, of solid content in the spray solutions, drying medium flux, temperature and aspiration rate of the spray drying process, on optical properties of the final sintered ceramics, were systematically investigated. The samples were sintered by using vacuum sintering at temperatures in the range of 1650–1735 °C 16 h. Aspiration rate of 70 % and solid concentration of 16–24 wt% should be used in order to obtain well granulated powders without obstruction of the nozzles. Optimal processing parameters include inlet temperature of 70 °C and flux of 40 % of the drying medium, in terms of the optimization of optical transparency.

3.2.2.3 Gel Methods

Gel methods involve the formation of semirigid gels or highly viscous resins from liquid precursors, which appear as an intermediate step toward ceramic powders. This type of methods is particularly useful for the synthesis of complex oxides, due to the high level chemical homogeneity that can be achieved. Oxide powders are usually obtained by decomposing the gels or resins, followed by calcination and milling to control the particle characteristics. To form the gels or resins, the starting constituents are mixed at the atomic scale through polymerization process. If no constituent is volatilized during the decomposition and calcination steps, the cation composition of the powder will be identical to that in the original solution. Therefore, these methods are able to achieve good chemical homogeneity and controllable stoichiometry. Different gel processes are discussed as follows.

Sol–Gel Process

Sol–gel process involves the formation of polymeric gels by hydrolysis, condensation and gelation, which are then dried and ground into powders [252–255]. Dried gels with lower viscosity are easier to grind, so that the extent of contamination introduced during the milling is relatively low. If the liquid content is removed under supercritical conditions, there is no shrinkage for the dried gels, which have therefore low viscosity. Preferably, metal alkoxides are used for sol–gel process, because they have strong hydrolysis reactions. However, in some cases, metal salts also have hydrolysis behaviors.

Metal alkoxides have a general formula of $M(OR)_z$, where z is an integer equal to the valence of the metal M, and R is an alkyl chain. They can be considered as

derivatives of either an alcohol, ROH, in which the hydrogen is replaced by the metal M, or a metal hydroxide, $M(OH)_z$, in which the hydrogen is replaced by an alkyl group. The reactions involve hydrolysis, which can be described by using the following equation:

$$M(OR)_z + xH_2O \rightarrow M(OR)_{z-x}(OH)_x + xROH, \tag{3.44}$$

which is followed by condensation and polymerization through dehydration reaction, as follows:

$$-M-OH + HO-M- \rightarrow -M-O-M- + H_2O. \tag{3.45}$$

Uniform particles have also been obtained through the hydrolysis of metal salt solutions [22, 23, 103, 127]. Comparatively, this method can produce powders with a wider range of chemical compositions. Besides oxides, hydrous oxides, sulfates, carbonates, phosphates, and sulfides can be prepared by using this method. However, more experimental parameters must be controlled in order to produce uniform particles, such as concentration of the metal salts, chemical composition of the starting materials, temperature, pH of the solution, and the concentrations of anions and cations that form intermediate complexes.

Metal ions are usually hydrated in aqueous solutions. The conditions for homogeneous precipitation of uniform particles can be realized by using a technique called forced hydrolysis. The key of this technique is to promote the deprotonation of hydrated cations by heating the solution at elevated temperatures (90–100 °C).

The soluble hydroxylated complexes produced by the hydrolysis reaction serve as the precursors of the nucleation. Nucleation and growth of uniform particles can be achieved by generating the precursors at proper rate, through the adjustment of temperature and pH value. A general approach is to age the solutions at elevated temperatures. It has been found that the process is very sensitive to a minor change in various conditions. Also, anions could play a decisive role in determining the outcome of the reaction. The conditions for precipitation of uniform particles should be specifically studied case by case. It is found that slow release of anions from organic molecules such as urea or formamide can be used provide the conditions for nucleation and growth of uniform particles in solution. Various oxides have been synthesized by using sol–gel process [253, 256–262].

A sol–gel process was developed to synthesize nanosized Y_2O_3 powders [256]. Various organic acids, including acetic acid, oxalic acid, malonic acid, tartaric acid and citric acid, were used as chelating agents, while yttrium nitrate hexahydrated was used as the source of yttrium, which was dissolved in water so that yttrium ion concentration was 0.5 mol L^{-1}. Organic acids were then slowly added in the form of aqueous solution with desired [chelating agent]/[Y] ratio. pH value was then adjusted to 2 with 30 % ammonia solution. The mixed solution was then heated at 115 °C for 12 h to form gels. For oxalic and tartaric acids, the gels should be filtrated and washed, because rigid gels could not be formed, due to the low

viscosity of their sols. All the filtrated and chelated gels were calcined at two temperatures, i.e., 800 and 1100 °C, in a flowing oxygen atmosphere, at a heating rate of 200 °C h^{-1} for 4 h. Two [chelating agent]/[Y] ratios were studied, i.e., 2 and 20.

It was found the powders derived from acetic, oxalic, malonic and tartaric acids exhibited crystalline grains, while amorphous phase was obtained for citric acid. Y_2O_3 powders could be readily formed in the precursor gels at heating temperatures of >700 °C. The chelating agent had no effect on composition of the Y_2O_3 powders. Average grain sizes of the Y_2O_3 powders, sintered at 800 and 1100 °C, were about 30 and 60 nm, respectively. However, chelating agent has a significant effect on morphologies of the Y_2O_3 grains, which simply follow the morphologies of the precursor gels. This study provided a reference on selection of chelating agent when the morphology of the powder is important. As stated earlier, spherical shapes with narrow particle size distribution are desired.

Nano-sized cerium-doped lutetium aluminum garnet (LuAG:Ce) powders were prepared by using a sol–gel combustion process, which was started from a mixed solution of metal nitrates, with an organic glycine as fuel [263]. The obtained precursor was agglomerated and had a foamy-like morphology, consisting of porous crystallites with a uniform size of about 40 nm. High purity crystalline LuAG:Ce powder was achieved by calcining the combustion precursor at 1000 °C for 2 h. Using the prepared powder, LuAG:Ce transparent ceramics have been fabricated by using vacuum sintering at 1850 °C for 10 h, followed by post-annealing at 1450 °C for 20 h in air. The transparent ceramics exhibited an in-line light transmittance of about 50 % in the visible wavelength range and had a uniform microstructure with an average grain size of about 8 μm.

Crystalline LuAG:Ce powders doped with 1.0 mol% CeO_2 ($Lu_{2.97}Ce_{0.03}Al_5O_{12}$) were prepared by a sol–gel combustion process, using glycine as a fuel. The process involves the exothermic reaction between metal nitrates and organic fuel, e.g., glycine. The typical stoichiometric synthesis reaction is:

$$\begin{aligned} 6M(NO_3)_3 + 10NH_2CH_2COOH + 18O_2 \rightarrow 3M_2O_3 \\ + 5N_2 + 18NO_2 + 20CO_2 + 25H_2O, \end{aligned} \tag{3.46}$$

where M represents Lu, Ce, and Al. The characteristics of the prepared powders are greatly influenced by the reaction temperature, which can be controlled by adjusting the molar ratio of glycine to metal nitrates. In the current study, a stoichiometric molar ratio of nitrate to glycine, i.e. 1.67, was adopted to prepare LuAG:Ce powders.

Lutetium oxide (Lu_2O_3, 99.99 %), aluminum nitrate hydrate ($Al(NO_3)_3{\cdot}9H_2O$, analytical grade), cerium nitrate hydrate ($Ce(NO_3)_3{\cdot}6H_2O$, 99.99 %), nitric acid (HNO_3, excellent grade), glycine (NH_2CH_2COOH, analytical grade), and deionized water were used as starting materials in the present work. High purity Lu_2O_3 powders were first dissolved in nitric acid to form lutetium nitrate solution. After completely dissolving, according to the general formula composition

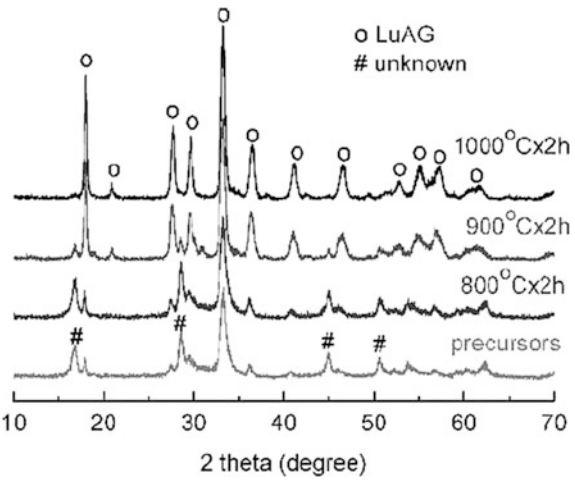

Fig. 3.49 XRD patterns of the as-prepared precursors and powders calcined at various temperatures. Reproduced with permission from [263]. Copyright © 2006, Materials Research Society

$Lu_{2.97}Ce_{0.03}Al_5O_{12}$, a stoichiometric cerium nitrate and aluminum nitrate were introduced to the resultant lutetium nitrate solution with appropriate dosage of glycine. The mixed solution was heated and continuously stirred using a magnetic agitator until a transparent sticky gel formed. Then the gel was rapidly heated, and an acute auto-combustion process took place at about 700 °C accompanied by the evolution of brown fumes. As a result, a brown and fluffy precursor was yielded. The precursor was then heat treated at 800–1000 °C for 2 h in a muffle furnace in air. The calcined powders were ball milled in a polyurethane container using 6 mm diameter ZrO_2 balls and ethanol as media for 2 h.

XRD patterns of the precursors prepared by the sol–gel combustion process and the powders calcined at various temperatures are shown in Fig. 3.49. It was unexpected that the precursors prepared by the present sol–gel combustion process using glycine as fuel were crystalline instead of amorphous, consisting of cubic LuAG and some unknown phase. Additionally, no distinct difference can be observed between the diffraction patterns of the resultant precursors and the powders calcined at 800 °C for 2 h. At 900 °C, the characteristic peaks of LuAG phase appeared with rather intense peaks and the unknown phase showed very weak peaks, indicating that mostly LuAG phase is produced at this temperature. At 1000 °C, continuing refinement of peak shapes and intensity was observed, indicating that crystalline LuAG grew with increasing calcination temperature.

Figure 3.50 shows typical EPMA and TEM micrographs of the as-prepared precursors and powders calcined at 1000 °C for 2 h, respectively. It can be seen that the precursors have a foamy-like and porous morphology (Fig. 3.50a), very similar to the one observed for the previously studied $(Gd,Y)_2O_3$ powders. The TEM micrograph of the precursors, shown in Fig. 3.50b, reveals the shape and size of primary particles. The as-prepared powders are agglomerated and consist of near-spherical crystallites of about 30-nm particle size estimated from TEM images. The TEM micrograph of the powders calcined at 1000 °C for 2 h, shown in Fig. 3.50c,

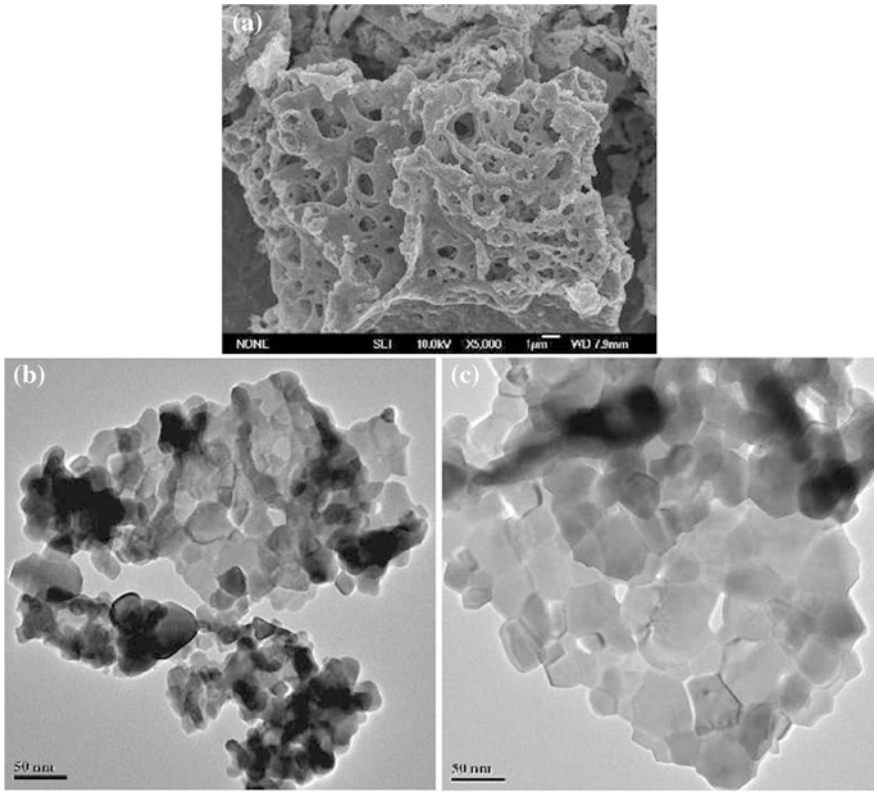

Fig. 3.50 EPMA and TEM micrographs of the precursors and powders calcined at 1000 °C for 2 h: **a** EPMA, precursors, **b** TEM, precursors and **c** TEM, powders calcined at 1000 °C for 2 h. Reproduced with permission from [263]. Copyright © 2006, Materials Research Society

reveals that the powders consist of pointed crystallites with fairly uniform size of about 40 nm.

Highly sinterable yttrium aluminum garnet (YAG) nanopowders have been synthesized by a sol–gel combustion method with various chelating agents and fuels, namely citric acid, tartaric acid, glycine, and ethylene diamine tetraacetic acid (EDTA) [260]. The preparation involved the thermal decomposition of a chelating agent (fuel)-nitrate gel and the formation of amorphous precursors. The as-synthesized precursors were studied by infrared spectroscopy (IR), thermogravimetric (TG) and differential scanning calorimetric (DSC) analyses. The nanopowders calcined at 1000 °C were characterized by X-ray powder diffraction (XRD) and transmission electron microscopy (TEM). It was found that the chelating agents and fuels used had a significant influence on the average grain size and agglomeration of YAG nanopowders. The rate of combustion reaction between chelating agent (fuel) and nitrate was responsible for the growth of the grains. Nanoparticles with the smallest size and high sinterability were obtained when using EDTA, which derived

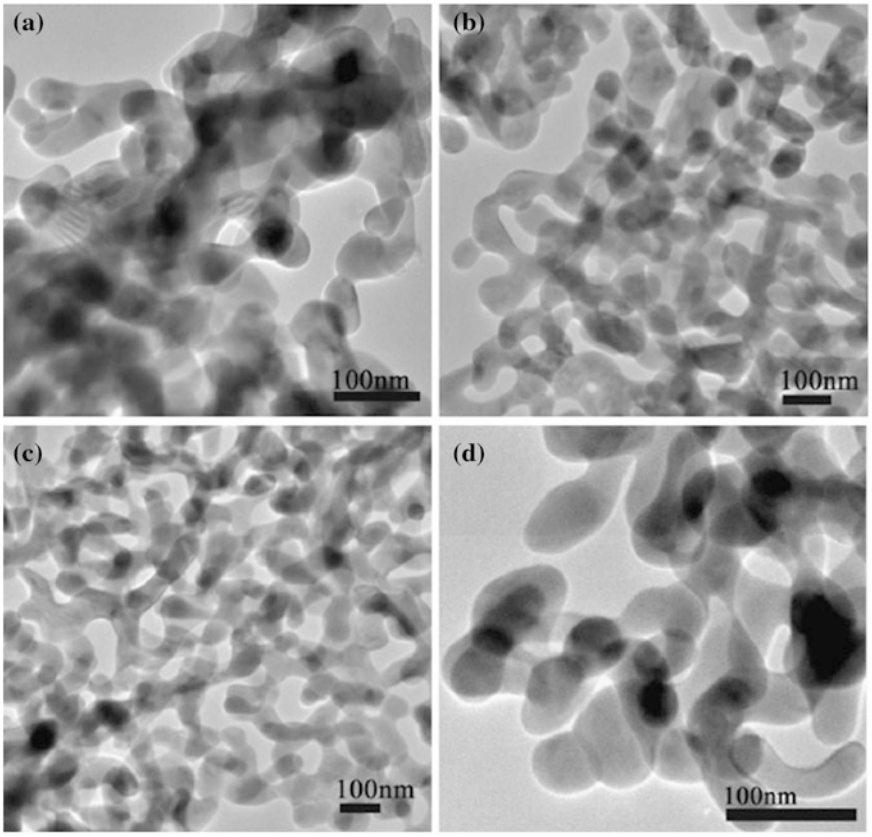

Fig. 3.51 TEM images of the YAG powders using chelating agents: **a** citric acid, **b** tartaric acid, **c** glycine and **d** EDTA. Reproduced with permission from [260]. Copyright © 2010, Elsevier

from the significant blocking of the diffusion path associated with the lowest combustion reaction rate.

Figure 3.51 shows TEM images of the YAG powders calcined at 1000 °C. Most particles had a semispherical shape with a relatively high porosity. Such porosity could be caused by the release of gas during the combustion process. By adjusting the content of the organic compounds, specific surface areas of the powders could be controlled. Average sizes of the nanopowders were 60, 80, 60 and 40 nm, corresponding to the chelating agents and fuels of citric acid, tartaric acid, glycine and EDTA, respectively. Citric acid and tartaric acid that showed the faster reaction led to larger average particle sizes. In contrast, smaller grains were observed when using EDTA. The faster the reaction, the fewer the residues would be in reaction process, which made the cations to diffuse more easily. Additionally, all the YAG nanopowders calcined at 1000 °C exhibited high crystallinity. Therefore, EDTA

was most suitable to synthesize YAG nanopowders with smallest grain size, which is beneficial for the preparation of transparent YAG ceramics.

Mullite ($3Al_2O_3{\cdot}2SiO_2$) powder has been prepared by supercritical drying the gels derived from sol–gel process, which has high sinterability with fully dense mullite ceramics to be obtained at a temperature of below 1200 °C [264–268]. This temperature is significantly lower than that required by the conventional solid-state reaction method from the precursors of mixed oxide. The high sinterability has been attributed to the amorphous structure, high surface area, and molecular level homogeneity of the gel-derived powders.

The Pechini Method

In the Pechini method, metal ions from starting materials, such as carbonates, nitrates, and alkoxides, are complexed in an aqueous solution with α-carboxylic acids, such as citric acid. When heated with a polyhydroxy alcohol, such as ethylene glycol, polyesterification takes place. Once excess liquid is removed, a transparent resin is formed. The resin is then heated to decompose the organic constituents. After milling and calcination, oxide powders can be obtained accordingly. Various oxide nanopowders have been synthesized by using Pechini or modified Pechini methods [269–276], although less information is available on the fabrication of transparent ceramics with these powders.

Cubic nanocrystalline Yb:Lu_2O_3 powders were synthesized by modified Pechini sol–gel method [277]. Lu_2O_3 nanocrystals doped with 50 % Yb were prepared using the modified Pechini method. Figure 3.52 shows the flow chart for the synthesis process. Lu_2O_3 (99.9 %) and Yb_2O_3 (99.9 %) were dissolved in concentrate HNO_3 ($\sim$65 %) under stirring, which was heated to form nitrates. With the moles of the EDTA, [EDTA], the moles of the metal cations, [metal], and the moles of ethylene glycol, [EG], two groups of molar ratios were used: [EDTA]/[Metal] = C_M and [EDTA]/[EG] = C_E. C_M measured the degree of the chelation process of the metal ions with the EDTA. For the solutions with low values of C_M, no homogeneous chelation of the metals occurred, due to insufficient EDTA molecules in the solutions. However, too high C_M meant that more organics had to be removed. Therefore, the value of C_M should be optimized. Experimental results indicated that molar ratio C_M = 1 was suitable the preparation of the metals–EDTA complexes. During mixing and heating, the esterification agent was added, ethylene glycol, with a molar ratio C_E equal to 2. By this way, the solution was transformed into precursor resin. On the other hand, C_E accounted the degree of esterification between the EDTA and the ethylene glycol. Finally, the viscous gel obtained was calcined at temperatures of 300–1000 °C for 1–5 h to form the nanocrystals of Yb:Lu_2O_3. Yb:Lu_2O_3 powders with sizes in the range of 50–100 nm could be obtained accordingly.

A Pechini-type sol–gel process was used to synthesize YAG nanophosphors, YAG:Ce,Pr system, with concentration of Pr^{3+} from 0.125 to 2 mol% while maintaining the content of Ce^{3+} constant at 2 mol%, for white light-emitting diode (LED) applications [278]. Yttrium and aluminum nitrates and acids were mixed

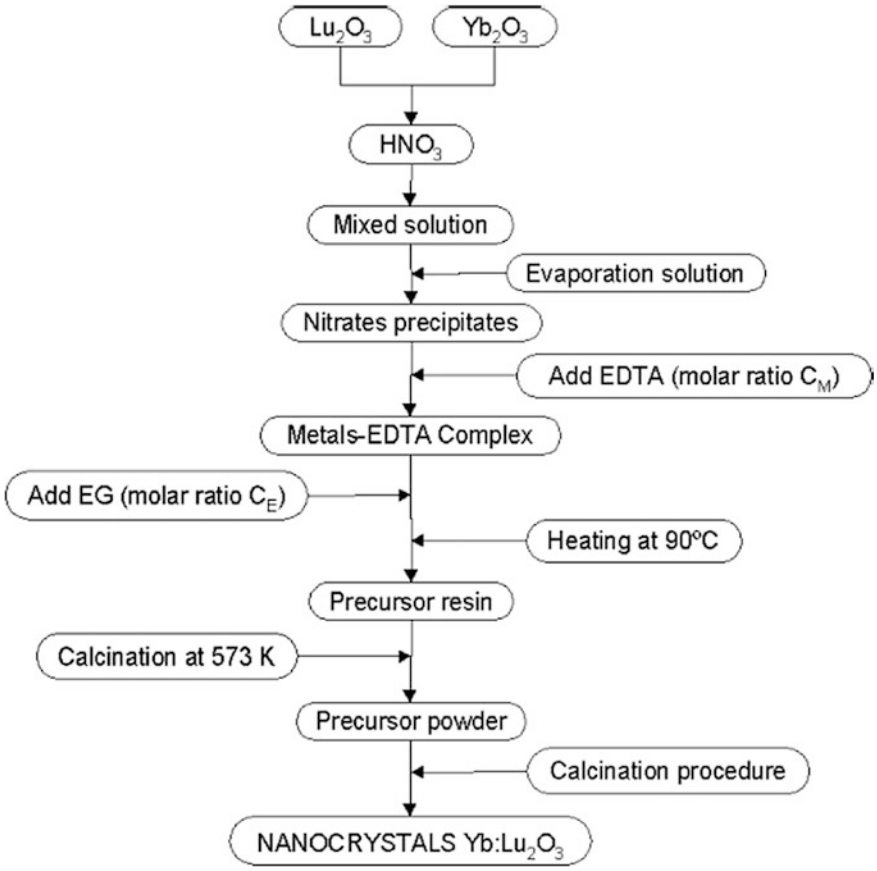

Fig. 3.52 Flow chart of synthesis of the Yb:Lu_2O_3 nanocrystals with a modified Pechini method. Reproduced with permission from [277]. Copyright © 2008, Elsevier

directly in a crucible at 100 °C. Solutions of lanthanides, with [Ce] = 24 mM and [Pr] = 6 mM, were prepared by dissolving the precursors in a mixture of HNO_3: H_2O = 1:1. After complete dissolution of the salts, EG was added and stirred until gels were formed. After that, the reaction mixtures were left on the hot plate overnight. Finally, the samples were calcined at 1000 °C for 4 h. The quantities of reagents were calculated according to the following reaction:

$$\begin{aligned} &xY(NO_3)_3 + 5Al(NO_3)_3 + yLn(NO_3)_3 + EG \\ &+ CA \longrightarrow HNO_3 : H_2OY_xAl_5O_{12} : Ln_y \end{aligned} \tag{3.47}$$

The molar ratio among all salts, CA and EG was 1:3:4.5, while 20 mL HNO_3: H_2O solution was used for every 10 mmol of salts. The obtained nanopowders had well crystalline structures.

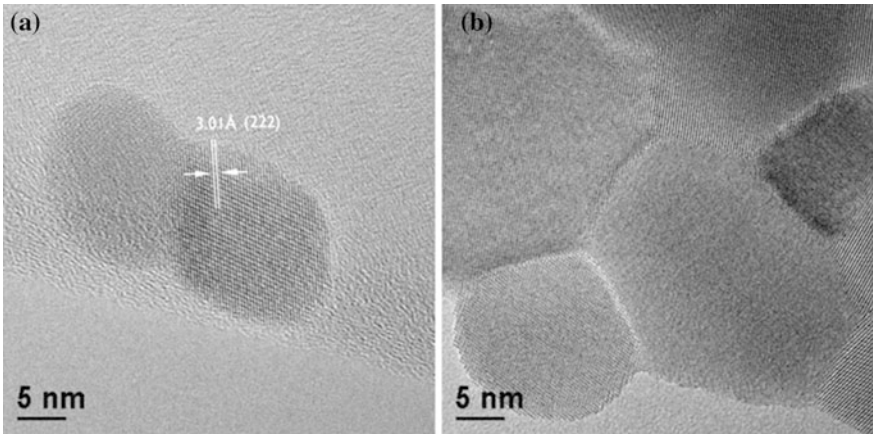

Fig. 3.53 HRTEM image showing single monocrystalline nanoparticles (sample Tb1Eu2, $Tb_{0.02}Eu_{0.04}Y_{1.94}O_3$) with crystal planes spacing of 3.01 Å, corresponding to the (222) crystal plane of Y_2O_3 (**a**), and TEM image of an agglomeration of the sample Y_2O_3 (**b**). Reproduced with permission from [279]. Copyright © 2013, Springer

Tb^{3+} and Eu^{3+} co-doped Y_2O_3 nanoparticles with a volume-weighted average size of about 30 nm have been synthesized by using a similar Pechini-type sol–gel process [279]. The nanopowders synthesized by using this method had an average particle size of about 35 nm. TEM images of representative samples are shown in Fig. 3.53.

A modified Pechini method was reported to synthesize nanosized $MgAl_2O_4$ spinel powders doped with Eu^{3+} ions [280]. XRD results indicated that the powders were single-phase spinel with high crystallinity. Concentration of the optically active Eu^{3+} ions has been set to 0.5–5 mol% in respect to the appropriate Mg^{2+} molar content. Starting materials used in the synthesis included high purity $Eu(NO_3)_3{\cdot}6H_2O$, $AlCl_3{\cdot}6H_2O$ and $Mg(NO_3)_2{\cdot}6H_2O$. Stoichiometric amounts of the three salts were dissolved in deionized water to for homogeneous solution. Required quantity of citric acid and ethylene glycol were added into the solution, which was then heated to 80 °C to increase its viscosity. The obtained resin was calcined at temperatures of 700–1000 °C for 3 h. White powders of $MgAl_2O_4$ and doped with Eu^{3+} were thus obtained. The average spinel particle sizes were about 15 nm for sample calcined at 700 °C and 20 nm at 1000 °C, respectively.

Citrate Gel Method

The citrate gel method involves the dissolving of solution of various nitrates in citric acid [257, 262, 281–289]. Through controlling the pH values, no precipitate is in the solutions. After the solution is heated at a suitable temperature in air for a period of time, it becomes more and more viscous liquid containing polybasic

chelates. Finally, amorphous solids are obtained, which are pyrolyzed in air to produce crystalline oxide powders.

A citrate gel combustion method has been reported to synthesize nanosized ytterbium doped yttria [290]. Nanocrystalline Yb^{3+}:Y_2O_3 powders single-phase cubic yttria crystal structure could be prepared by calcining the as-prepared precursors at 1100 °C for 3 h. Powders obtained were well dispersed with an average particle size of 60 nm. By using the obtained powders, nearly fully dense Yb^{3+}:Y_2O_3 ceramics, with promising optical properties, were produced by vacuum sintering at 1800 °C for 12 h.

Citrate gel combustion method is a modified sol–gel technique in which the gel is decomposed by a self-propagating high temperatures synthesis (SHS) process. It is a combination of sol–gel and SHS reaction processes. An aqueous nitrate solution of Y^{3+} and Yb^{3+} were prepared by dissolving Y_2O_3 (99.99 %) and Yb_2O_3 (99.99 %) in diluted nitric acid under stirring at 80 °C for 2 h. The metal nitrates were weighted according to the required proportion and mixed in a glass cylindrical beaker with doping of minor amount of ammonium sulfate ($(NH_4)_2SO_4$) as a dispersant. Double distilled water was used in the experiments for homogenous mixing of metal nitrates. Citric acid was added to the mixtures as a fuel and mixed thoroughly followed by a clear solution was obtained. It was calculated that 1.667 mol of citric acid was required to prepare 1 mol of yttria with complete combustion. The equivalence ratio, i.e., the ratio of the oxidizing valency to reducing valency (O/F) was maintained at unity (O/F = 1). The valency of nitrogen was not considered because of its conversion to molecular nitrogen (N_2) during combustion. The assumed complete combustion reactions can be written as:

$$\begin{aligned} &6RE(ON_3)_3 + 5CH_2COOHCOHCOOHCH_2COOH \\ &\rightarrow 3RE_2O_3 + 9N_2 \uparrow + 30CO_2 \uparrow + 20H_2O \uparrow \end{aligned} \tag{3.48}$$

The mixed solution in the glass beaker was kept in a water bath of 80 °C for 8 h until it transformed into a honey-like yellow transparent gel. The gel was dried at 120 °C for 24 h and became a deep yellow sticky gel. This gel was rapidly heated to 300 °C and at this stage an auto combustion process occurred accompanied with a brown fume, and finally yielded a fluffy precursor. The precursor was crushed and then heat treated at temperatures ranging from 600 to 1100 °C for 3 h in an oxygen atmosphere. For sintering, powders calcined at 1100 °C for 3 h were dry pressed into Ø15 mm pellets in a steel mold at 30 MPa and then cold isostatically pressed (CIP) at 200 MPa. The pellets were then sintered under vacuum at 1800 °C. The vacuum in the furnace was 10^{-3} Pa during the sintering period.

Figure 3.54 shows SEM morphologies of the Yb^{3+}:Y_2O_3 nanopowders calcined at 1100 °C for 3 h without (Fig. 3.54a) and with (Fig. 3.54b) ammonium sulfate doping. From Fig. 3.54b, it can be seen that particles with sulfate doping disperse uniformly, and have a relatively narrow size distribution. Most particles are spherical in shape with the average particle size of about 60 nm. The release of gas in the combustion process gave a significantly porous structure in the calcined

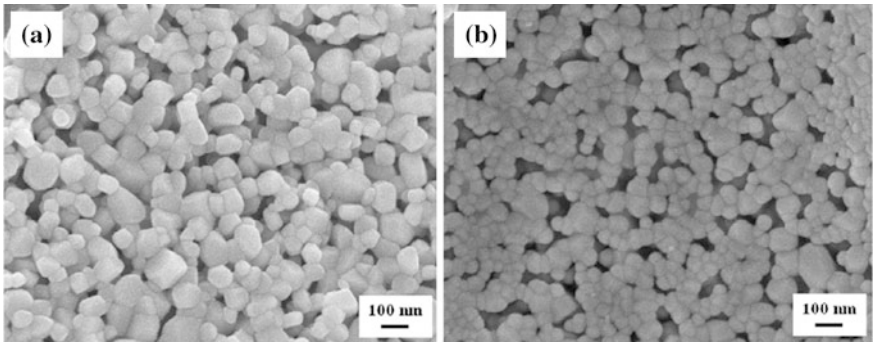

Fig. 3.54 SEM images of the Yb^{3+}:Y_2O_3 powders calcined at 1100 °C without sulfate ions doping (**a**) and doped with sulfate ions (**b**). Reproduced with permission from [290]. Copyright © 2011, Elsevier

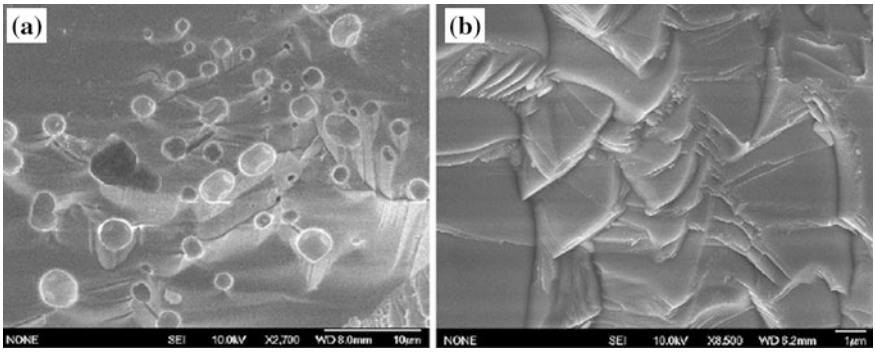

Fig. 3.55 Fracture surface SEM images of the Yb^{3+}:Y_2O_3 ceramics sintered at 1800 °C for: **a** 5 h and **b** 12 h. Reproduced with permission from [290]. Copyright © 2011, Elsevier

powders, and this is beneficial to the dispersion of powders. Compared with Fig. 3.54b, powder without sulfate doping has a lower dispersivity and a wide size distribution with a range from 50 to 90 nm, and is not so uniform with a mixture of spherical and rectangular in morphology.

Figure 3.55 is the SEM images of fracture surfaces of the sintered yttria ceramic samples by vacuum sintering process under 1800 °C for 5 h (Fig. 3.55a) and for 12 h (Fig. 3.55b). The presence of a great number of porosity at grain boundary junctions and as clusters in the grain interior can be seen in the sample sintered for 5 h. With the increase of sintering time, a significant grain growth and densification has occurred in the sample, it can be seen that nearly pore-free microstructure of the sample remained homogeneous without abnormal grain growth, and transgranular fracture indicates that no pore entrapment has occurred in the densified regions (Fig. 3.55b).

Glycine Nitrate Process

Glycine nitrate process is a combustion method for the preparation of ceramic powders [291–299]. A highly viscous mass is formed by evaporation of a solution of metal nitrates and glycine is ignited to produce powders. Glycine, an amino acid, is used to form complexes with the metal ions in the solution. It can increase the solubility of the nitrates and prevents the precipitation of the metal ions when water is evaporated. Because the thorough mixing of the starting constituents, the final powders have high chemical homogeneity. Glycine also serves fuel to enhance the ignition step, because it is oxidized by the nitrate ions. The reactions during the ignition are highly explosive, so that extreme care must be taken during this step. Large quantity production should be avoided at lab research scale. The final products are usually loose mass of extremely fine and crystalline powders. As compared with the Pechini method, milling and calcination of the products are not necessary. The ultrafine size and crystalline nature of the powders are attributed to the rapid reaction during the ignition at high temperatures.

Nanosized cubic yttria-stabilized zirconia (ZrO_2–8 mol% Y_2O_3) powder was synthesized by using a glycine–nitrate process, which was combined with high-energy ball milling [300]. Effect of calcination temperature on sintering activity of the powders was studied to identify the optimized calcination temperature, which was 900 °C, in terms of sinterability. Sintering of the nanopowder was carried out by using spark plasma sintering at 1200–1350 °C for 5 min. Transparent ceramics could be achieved at 1300 °C.

High purity $Zr(NO_3)_4{\cdot}5H_2O$ and $Y(NO_3)_3{\cdot}6H_2O$ were used as starting materials for synthesis. They were mixed according to the composition of 92 mol% ZrO_2 + 8 mol% Y_2O_3 and dissolved in deionized water. After that, glycine was added into the solution as a fuel, with a molar ratio of glycine to total metal ions (Zr + Y) of 2.5:1. Precursors were formed by adding ammonia water to the solution at a rate of 3 mL/min, until to pH = 8. Then, ethylene glycol (EG), with a molar ratio of glycine:EG to be 1:1, was added into the solution to trigger the esterification reaction. The resultant solution was heated at 75 °C with stirring to form gel precursors. After aging for 12 h, the gel was filtered and thoroughly washed with ethanol. Finally, the gel was dried at 150 °C and ignited to brown powders.

The brown powder was first ball milled with high purity zirconia balls for 12 h at a rotational speed of 200 rpm, in isopropyl alcohol with 3 wt% polyethylene glycol. The ball milled mixture was dispersed supersonically for 30 min and then dried by using a rotary evaporator. The dried powder was further calcined at different temperatures for 2 h. Finally, the calcined powders were ball milled for second time with zirconia balls for 12 h in isopropyl alcohol. The milled powders were dried and then sintered by using SPS, with graphite dies with an inner diameter of 15 mm at 50 MPa uniaxial pressure. The temperature was increased to 600 °C within 10 min, from where and onwards the pressure was increased to 100 MPa. The samples were sintered at 1200–1350 °C for 5 min at a heating rate of 100 °C min^{-1}.

Figure 3.56 shows SEM images of the powders in form of pellets, which were calcined 700 and 900 °C first and then annealed at 1100 °C for 1 h [300]. The

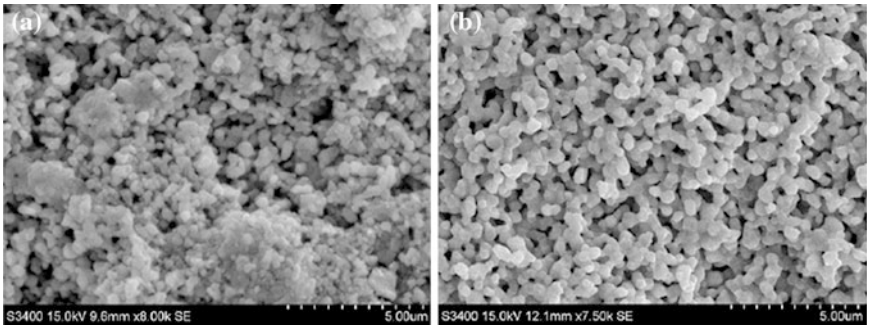

Fig. 3.56 SEM images of the powders calcined in air at **a** 700 °C and **b** 900 °C. Reproduced with permission from [300]. Copyright © 2012, Elsevier

sample from the 700 °C-calcined powder was still powder-like without obvious sign of sintering, while the one from the 900 °C-calcined powder was a porous ceramics, with obvious grain growth, as shown in Fig. 3.56b. It has been well known that low calcination temperature leads to porous powders, which cannot be compacted densely and uniformly. However, too high calcination temperature results in powder with reduced specific surface area and thus poor sinterability. Therefore, there is an optimized calcination temperature for different nanopowders, which was 900 °C for the 8YSZ nanopowder.

Figure 3.57 shows SEM images of the 8YSZ ceramics sintered at different temperatures [300]. The samples sintered at 1200 and 1250 °C had grain sizes still at the nanometric scale, with pores were mainly located at grain boundaries. At the early and intermediate stages of SPS process, creeping and sliding of grains are the dominating mechanism of densification, which is beneficial to break hard agglomerates and destroy large pores, without the occurrence of grain growth. Significant grain growth was observed as the sintering temperature was above 1250 °C. At the final stage of sintering at high temperatures, densification is dominated by grain boundary diffusion. It is well accepted that the grain growth of YSZ is closely related to the diffusion of oxygen vacancy, which is enhanced with increasing temperature. Therefore, at high temperatures, pores could be entrapped due to fast grain boundary migration, thus leading to pores that were changed to be from intergranular to intragranular, as shown in Fig. 3.57d.

3.2.2.4 Nonaqueous Liquid Reactions

Reactions in nonaqueous liquids are mainly used to synthesize nonoxide powders, such as Si_3N_4. One of the advantages of these methods is the high purity and fine particle size of the powder. There are at least four such reactions: (i) vapor phase reactions, (ii) gas–solid reactions, (iii) gas–liquid reactions and (iv) gas–gas reactions.

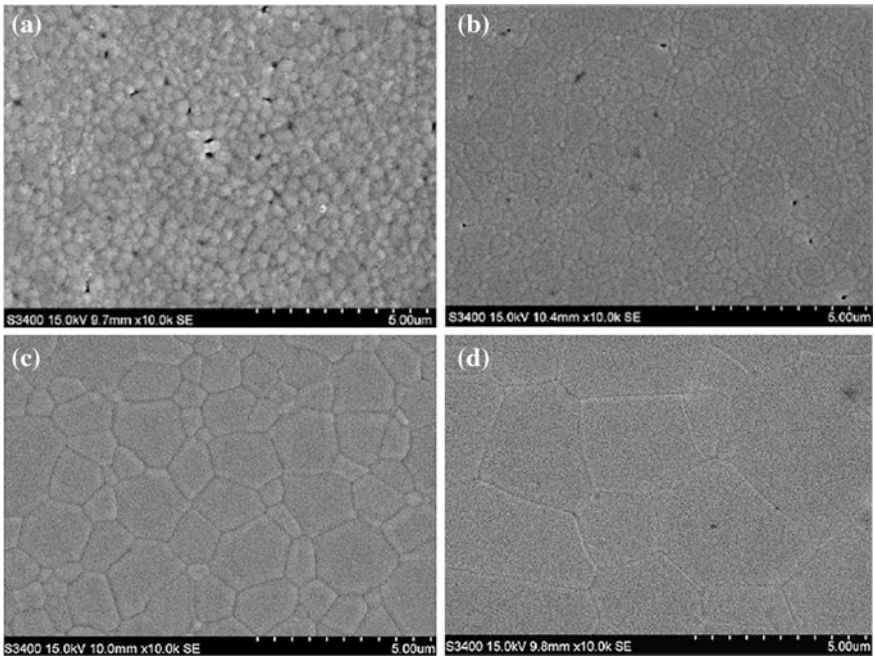

Fig. 3.57 SEM images of thermally etched surfaces of the samples sintered by using SPS at different temperatures: **a** 1200 °C, **b** 1250 °C, **c** 1300 °C and **d**1350 °C. Reproduced with permission from [300]. Copyright © 2012, Elsevier

Vapor phase reactions can be used synthesize oxide and nonoxide powders. The synthesis of Si_3N_4 and SiC powders will be used as examples to discuss these reactions [301–308]. Si_3N_4 has two hexagonal polymorphs, α-phase and β-phase, with the α-phase having slightly higher free energy at the formation temperature. Powders of α-Si_3N_4 have a more equiaxial particle shape and higher sinterability than β-Si_3N_4, because the particles of the latter grow into more elongated shape. Therefore, α-Si_3N_4 is more preferred.

One example of gas–solid reactions is nitridation. Direct nitridation of Si is a widely used method to synthesize Si_3N_4 powders, in which Si powder with particle sizes in the range of 5–20 μm is reacted with N_2 at temperatures of 1200–1400 °C for 10–30 h [309–314]. The Si_3N_4 powder is usually a mixture of α and β phases. The relative quantities of the two phases can be controlled by selecting the reaction temperature, the partial pressure of the N_2 gas in the nitriding atmosphere, and the purity of the Si powder. Si_3N_4 powder can also be produced through the carbothermic reduction of SiO_2 in a mixture of fine SiO_2 and C powders, which is followed by nitridation at 1200–1400 °C in N_2 [315]. Due to the widespread availability of pure fine SiO_2 and C, this method has become an attractive alternative to the direct nitridation of Si.

As a gas–liquid reaction, it has been showed that the reaction between liquid silicon tetrachloride ($SiCl_4$) and NH_3 gas in dry hexane at 0 °C can be used to prepare fine Si_3N_4 powder with very low levels of metallic impurities (<0.03 wt%) [316]. The powder synthesized through this reaction is amorphous, which can be crystallized to α-Si_3N_4 by heating at 1200–1400 °C for a prolonged time.

An example of gas–gas reactions is the formation of particles through the homogeneous nucleation and growth in the gas phase and is governed by the same equations for the nucleation of liquid droplets from a supersaturated vapor described above, i.e., Eqs. (3.18)–(3.24). Gas-phase reactions have been used to produce ceramic powders at both industrial scale and laboratory scale. Various heating techniques, including flame, furnace, plasma, and laser, are being used to the reactant gases for gas–gas reactions. Among these, flame synthesis, especially flame spray pyrolysis, has been emerged as a newly developed technique used to synthesize various oxide powders [317–326].

Figure 3.58 shows a schematic diagram of a representative flame assisted spray pyrolysis (FASP) reactor, which has been used to synthesize oxide nanoparticles [317]. Fuel, consisting of 1–12 mL min^{-1} of C_2H_2 of ⩾99.5 % or 12–30 mL min^{-1} of H_2 of ⩾99.999 %, was delivered through 12 holes (i.d. = 0.5 mm) equidistantly placed at the inner perimeter of a cylindrical torus ring (i.d. = 1.6 cm) coaxially to and at 1 cm above the nozzle issuing the precursor solution spray. A stainless steel tube (i.d. = 1.6 cm) was placed between ring and nozzle to shield the spray from air entrainment. Precursor solutions were fed through the central nozzle by a syringe pump at 2 mL min^{-1} and atomized by co-flowing 6 mL min^{-1} of oxygen (⩾99.5 %) through the surrounding annulus at 1.5–1.7 bar pressure drop. Additional sheath oxygen was supplied through 32 holes of 0.8 mm diameter each surrounding the nozzle at 1.5 cm radius. All gas flow rates were controlled by calibrated mass flow controllers. Using a vacuum pump, product particles were collected on water cooled glass microfiber filters (25.7 cm in diameter) placed at least 60 cm above the burner.

A flame spray pyrolysis (FSP) technique has been used to synthesize lutetium oxide (Lu_2O_3) nanoparticles from lutetium nitrate [323]. Optical quality transparent ceramics were prepared via hot pressing of the Lu_2O_3 nanoparticles formed using the FSP technique. A custom built flame spray pyrolysis system was used in this study. The system was composed of a two phase nozzle, consisting of a central capillary tube, surrounded by a ring of pilot flames, which were supplied with 1.5 L min^{-1} CH_4 and 3 L min^{-1} O_2. After ignition of the pilot flames, a co-flowing stream of O_2 and the liquid precursor are fed through the central capillary tube, where the oxygen was used as a dispersion gas to atomize the liquid precursor. All gases were supplied with flow rates regulated by using mass flow controllers.

The experiments were carried out by varying the O_2 dispersion gas flow rate from 2 to 5 L min^{-1}. The powders were collected on Whatman GF 6 glass fiber filter paper mounted in a water cooled stainless steel collection chimney equipped with a vacuum pump (Busch). The Lu_2O_3 samples were synthesized from a solution of $Lu(NO_3)_3 \cdot 6H_2O$ containing 100 g of the nitrate crystal dissolved in 500 ml DI water. The nitrate solution was then purified by crystallization and subsequent washes, followed by filtration through 0.8 μm filter media. Batches of 20 g of Lu

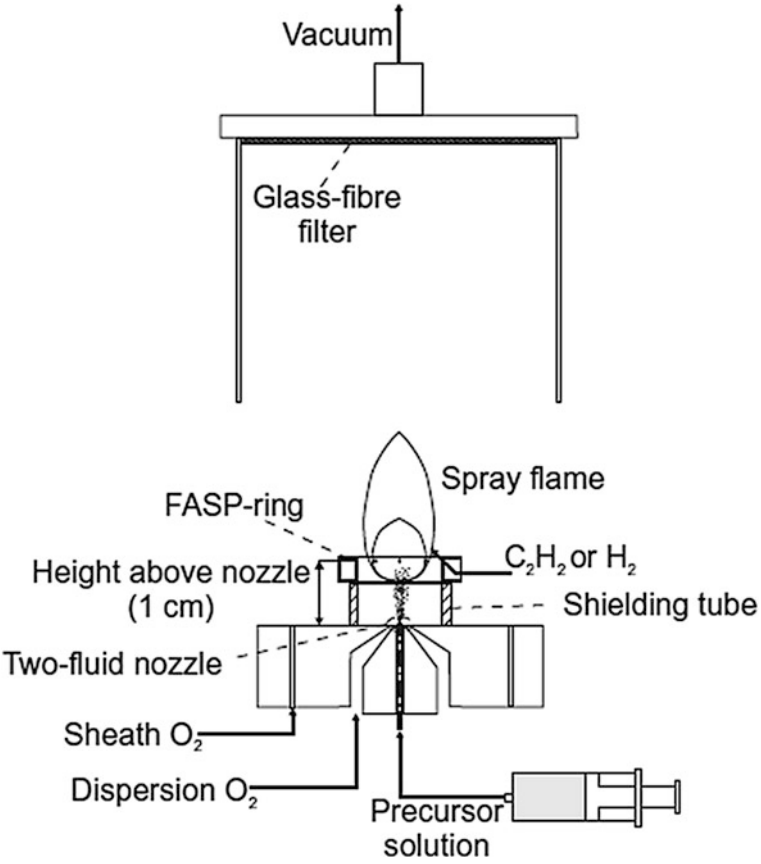

Fig. 3.58 Schematic of a flame assisted spray pyrolysis (FASP) reactor consisting of a two-fluid nozzle for atomizing the liquid precursor with oxygen and a cylindrical torus (FASP) ring with boreholes to inject and combust C_2H_2 with the precursor solution spray. The ring was located at 1 cm above the nozzle and the spray was shielded from air entrainment by a tube. Reproduced with permission from [317]. Copyright © 2013, Elsevier

$(NO_3)_3 \cdot 6H_2O$ were dissolved in 100 ml of ethanol to obtain the final FSP nanoparticle precursor solution.

Figure 3.59 is a transmission electron microscope image of a sample of cubic Lu_2O_3 nanoparticles, with the corresponding particle size distribution given in Fig. 3.59b. The mean particle diameter was found to be 15 nm. The sample was synthesized with an oxygen dispersion gas flow rate of 2 L min^{-1} and a precursor flow rate of 10 mL min^{-1}. It can be seen that the sample consists of agglomerates as well as primary particles that have been broken off during the sonication process. The BET surface area of the particles was found to be 28.9 m^2 g^{-1}, with an equivalent diameter of 22 nm. XRD indicated that the oxygen dispersion gas flow rate could be used control the phase content of the final Lu_2O_3 powders. For

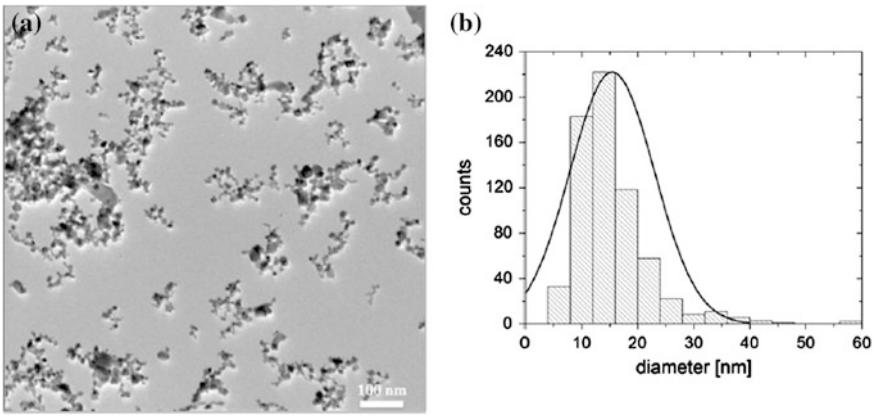

Fig. 3.59 **a** TEM image of the Lu_2O_3 nanoparticle and **b** its particle size distribution. Reproduced with permission from [323]. Copyright © 2012, Elsevier

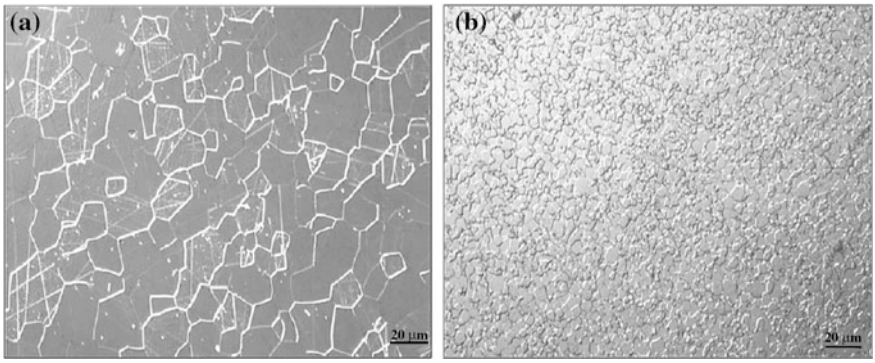

Fig. 3.60 SEM images of the cubic phase sample hot pressed at **a** 1625 °C and **b** the mixed phase hot pressed at 1450 °C. Reproduced with permission from [323]. Copyright © 2012, Elsevier

instance, the sample that was synthesized at 2 L min^{-1} was pure cubic Lu_2O_3, with space group of *Ia3*, whereas the one synthesized at 5 L min^{-1} contains a metastable monoclinic phase.

The powders were mixed with a sintering aid before sintering. Hot pressing densification was carried out in vacuum in a temperature range of 1450–1625 °C, at a pressure of ~8 kpsi, followed by hot isostatic pressing at 30 kpsi. The polished samples exhibited high transparency. Densification of ceramic powders is accomplished through atomic diffusion which is activated by thermal and shear energy in the case of hot pressing. Since hot pressing uses both thermal and mechanical energy sources, ceramics can be densified at lower temperatures which results in a finer grained microstructure.

Figure 3.60 shows SEM images of the samples made with the pure cubic phase powder that was hot pressed at 1625 °C and the mixed monoclinic phase pressed at

1450 °C [323]. The mixed phase sample had greatly reduced grain size, due to its lower sintering temperature. In other words, flame spray synthesis process offered an additional advantage to produce metastable phase, in this case (Lu_2O_3). The monoclinic Lu_2O_3 phase is a high free energy metastable phase, as compared with the cubic equilibrium phase. Because the high free energy, the presence of the monoclinic phase reduced the sintering temperature and pressure. The metastable phase was completely transferred to cubic phase during the hot pressing sintering.

3.3 Summary

A wide range of methods have been used to synthesize ceramic powders, with different compositions. Although most of these methods are applicable to transparent ceramic power synthesis, some of them have not been employed in the fabrication of transparent ceramics. Solid-state reaction is still the key method, while wet-chemical routes are increasingly used, whereas gas-phase reactions are only limited to nonoxide ceramics. For large scale applications, cost-effectiveness, environmental friendliness and less energy consumption, are all very important considerations, when selecting synthetic methods.

References

1. Biswas DR (1989) Development of novel ceramic processing. J Mater Sci 24:3791–3798
2. Kendall K (1989) Influence of powder structure on processing and properties of advanced ceramics. Powder Technol 58:151–161
3. Rice RW (1990) Ceramic processing—an overview. AIChE J 36:481–510
4. Sakai S, Ito S (1988) Problems on grinding process for ceramics. J Japan Soc Lubr Eng 33:509–513
5. Rahaman MN (2003) Ceramic processing and sintering, 2nd edn. CRC Press, New York
6. De Bonis A, Cultrone G, Grifa C, Langella A, Morra V (2014) Clays from the Bay of Naples (Italy): new insight on ancient and traditional ceramics. J Eur Ceram Soc 34:3229–3244
7. Gong H, Zhang J, Tang DY, Xie GQ, Huang H, Ma J (2011) Fabrication and laser performance of highly transparent Nd:YAG ceramics from well-dispersed Nd:Y_2O_3 nanopowders by freeze-drying. J Nanopart Res 13:3853–3860
8. Haruta M, Delmon B (1986) Preparation of homodisperse solids. J Chim Phys Phys Chim Biol 83:859–868
9. Hu S, Lu CH, Wang W, Ding MY, Ni YR, Xu ZZ (2013) Synthesis of monodisperse erbium aluminum garnet (EAG) nanoparticles via a microwave method. J Rare Earths 31:490–496
10. Huang YH, Jiang DL, Zhang JX, Lin QL, Huang ZR (2011) Synthesis of mono-dispersed spherical Nd:Y_2O_3 powder for transparent ceramics. Ceram Int 37:3523–3529
11. Li J, Li JP, Chen Q, Wu WJ, Xiao DQ, Zhu JG (2012) Effect of ammonium sulfate on the monodispersed $Y_3Al_5O_{12}$ nanopowders synthesized by co-precipitant method. Powder Technol 218:46–50
12. Li JS, Sun XD, Liu SH, Huo D, Li XD, Li JG et al (2013) Synthesis of dispersed Y_2O_3 nanopowder from yttrium stearate. In: Bao YW, Jiang DY, Gong JH (eds) Testing and evaluation of inorganic materials III. Trans Tech Publications Ltd, Stafa-Zurich, pp 3–7

13. Li XX, Wang WJ (2009) Preparation of uniformly dispersed YAG ultrafine powders by co-precipitation method with SDS treatment. Powder Technol 196:26–29
14. Xu GG, Zhang XD, He W, Liu H, Li H, Boughton RI (2006) Preparation of highly dispersed YAG nano-sized powder by co-precipitation method. Mater Lett 60:962–965
15. Xu XJ, Sun XD, Liu H, Li JG, Li XD, Huo D et al (2012) Synthesis of monodispersed spherical yttrium aluminum garnet (YAG) powders by a homogeneous precipitation method. J Am Ceram Soc 95:3821–3826
16. Dudnik EV, Zaitseva ZA, Shevchenko AV, Lopato LM (1995) Sintering of ultradisperse powders based on zirconium dioxide (Rev). Powder Metall Met Ceram 34:263–271
17. Aiken B, Hsu WP, Matijevic E (1988) Preparation and properties of monodispersed colloidal particles of lanthanide compounds, 3. Yttrium (III) and mixed yttrium (III)—cerium (III) systems. J Am Ceram Soc 71:845–853
18. Bogush GH, Tracy MA, Zukoski CF (1988) Preparation of monodisperse silica particles—control of size and mass fraction. J Non-Cryst Solids 104:95–106
19. Hsu WP, Ronnquist L, Matijevic E (1988) Preparation and properties of monodispersed colloidal particles of lanthanide compounds, 2. Cerium (IV). Langmuir 4:31–37
20. Lamer VK (1948) Monodisperse colloids and higher-order Tyndall spectra. J Phys Colloid Chem 52:65–76
21. Li J, Wu YJ, Tanaka H, Yamamoto T, Kuwabara M (2004) Preparation of a monodispersed suspension of barium titanate nanoparticles and electrophoretic deposition of thin films. J Am Ceram Soc 87:1578–1581
22. Matijevic E (1985) Production of monodispersed colloidal particles. Annu Rev Mater Sci 15:483–516
23. Matijevic E (1986) Monodispersed colloids—art and science. Langmuir 2:12–20
24. Pizette P, Martin CL, Delette G, Sornay P, Sans F (2010) Compaction of aggregated ceramic powders: from contact laws to fracture and yield surfaces. Powder Technol 198:240–250
25. Lee HM, Huang CY, Wang CJ (2009) Forming and sintering behaviors of commercial α-Al_2O_3 powders with different particle size distribution and agglomeration. J Mater Process Technol 209:714–722
26. Staiger M, Bowen P, Ketterer J, Bohonek J (2002) Particle size distribution measurement and assessment of agglomeration of commercial nanosized ceramic particles. J Dispersion Sci Technol 23:619–630
27. Bouvard D, Carry C, Chaix JM, Martin CM, Missiaen JM, Perier-Camby L et al (2001) Compression and sintering of powder mixtures: experiments and modelling. Adv Eng Mater 3:593–597
28. Olmos L, Martin CL, Bouvard D (2009) Sintering of mixtures of powders: experiments and modelling. Powder Technol 190:134–140
29. Johnson DW (1981) Non-conventional powder preparation techniques. Am Ceram Soc Bull 60:221–224
30. Hlavacek V, Puszynski JA (1996) Chemical engineering aspects of advanced ceramic materials. Ind Eng Chem Res 35:349–377
31. Kwade A (2001) Ultrafine comminution of ceramic raw materials—part 2: application. CFI-Ceram Forum Int 78:E39–E44
32. Kwade A (2001) Ultrafine comminution of ceramic raw materials part 1: fundamentals. CFI-Ceram Forum Int 78:E37–E45
33. Eskandari A, Aminzare M, Hesabi ZR, Aboutalebi SH, Sadrnezhaad SK (2012) Effect of high energy ball milling on compressibility and sintering behavior of alumina nanoparticles. Ceram Int 38:2627–2632
34. Yu SH (2001) Hydrothermal/solvothermal processing of advanced ceramic materials. J Ceram Soc Jpn 109:S65–S75
35. Roy R (1998) The sol-gel process in ceramic science: early history of discovery and subsequent development. In: Komarneni S, Sakka S, Phule PP, Laine RM (eds) Sol-Gel synthesis and processing. pp 3–36

36. Kong LB, Ma J, Huang H (2002) Low temperature formation of yttrium aluminum garnet from oxides via a high-energy ball milling process. Mater Lett 56:344–348
37. Kong LB, Ma J, Huang H (2002) $MgAl_2O_4$ spinel phase derived from oxide mixture activated by a high-energy ball milling process. Mater Lett 56:238–243
38. Dominey DA, Morley H, Young DA (1965) Kinetics of decomposition of nickel oxalate. Trans Faraday Soc 61:1246–1255
39. Tompkins FC, Young DA (1965) Decomposition of calcium azide. Trans Faraday Soc 61:1470–1480
40. L'Vov BV (2001) The physical approach to the interpretation of the kinetics and mechanisms of thermal decomposition of solids: the state of the art. Thermochim Acta 373:97–124
41. L'Vov BV (2002) Mechanism and kinetics of thermal decomposition of carbonates. Thermochim Acta 386:1–16
42. Salem IA, El-Maazawi M, Zaki AB (2000) Kinetics and mechanisms of decomposition reaction of hydrogen peroxide in presence of metal complexes. Int J Chem Kinet 32:643–666
43. Drozdetskaya GV, Gropyanov VM (1977) Calculation of kinetics of $CaCO_3$ decomposition under nonisothermal conditions. J Appl Chem USSR 50:480–483
44. Gallagher PK, Johnson DW (1976) Kinetics of thermal-decomposition of $CaCO_3$ in CO_2 and some observation on kinetic compensation effect. Thermochim Acta 14:255–261
45. Koga N, Tanaka H (1988) Kinetics of thermal-decomposition of $CaCO_3$ to MO, $SrCO_3$ to MO, $BaCO_3$ to MO. J Therm Anal 34:177–188
46. Kingery WD, Bowen HK, Uhlmann DR (1976) Introduction to ceramics, 2nd edn. Wiley, New York
47. Carter CB, Norton MG (2007) Ceramics materials: science and engineering. Springer, Berlin
48. Ewing J, Beruto D, Searcy AW (1979) Nature of CaO produced by calcite powder decomposition in vacuum and in CO_2. J Am Ceram Soc 62:580–584
49. Jander W (1927) Reactions in solid states at room temperature, I. Announcement the rate of reaction in endothermic conversions. Z Anorg Allg Chem 163:1–30
50. Jander W (1934) The reaction process in solid states. Angew Chem 47:0235–0238
51. Carter RE (1961) Kinetic model for solid-state reactions. J Chem Phys 34:2010–2015
52. Carter RE (1961) Mechanism of solid-state reaction between magnesium oxide and aluminum oxide and between magnesium oxide and ferric oxide. J Am Ceram Soc 44:116–120
53. Ikesue A, Furusato I, Kamata K (1995) Fabrication of polycrystalline transparent YAG ceramics by a solid-state reaction method. J Am Ceram Soc 78:225–228
54. Wang JQ, Yue YL, Tao WH, Yu QH, Tao ZD, Sun XD (2003) Preparation of transparent yttrium aluminum garnet ceramics by relatively low temperature solid-state reaction. Trans Nonferrous Metals Soc China 13:1096–1101
55. Wen L, Sun XD, Ma WM (2004) Fabrication of transparent Nd :YAG ceramics by a solid-state reaction method. J Inorg Mater 19:295–301
56. Li HL, Liu XJ, Huang LP (2005) Fabrication of transparent cerium-doped lutetium aluminum garnet (LuAG:Ce) ceramics by a solid-state reaction method. J Am Ceram Soc 88:3226–3228
57. Li HL, Liu XJ, Huang LP (2006) Fabrication of transparent Ce:LuAG ceramics by a solid-state reaction method. J Inorg Mater 21:1161–1166
58. Wu YS, Li J, Qiu FG, Pan YB, Liu Q, Guo JK (2006) Fabrication of transparent Yb, Cr:YAG ceramics by a solid-state reaction method. Ceram Int 32:785–788
59. Li J, Chen Q, Yang LL, Feng GY, Wu WJ, Zheng FS et al (2011) High transmittance of Nd-doped YAG transparent ceramics prepared by solid-state reaction method. Ferroelectrics 411:62–68
60. You YL, Qi LH, Miao HZ, Pan W (2013) Preparation of transparent YAG ceramics via a modified solid-state reaction method. Rare Metal Mater Eng 42:348–350
61. Li JL, Xu J, Shi Y, Qi HF, Xie JJ, Lei F (2014) Fabrication and microstructure of cerium doped lutetium aluminum garnet (Ce:LuAG) transparent ceramics by solid-state reaction method. Mater Res Bull 55:161–167

62. Ganesh I, Srinivas B, Johnson R, Saha BP, Mahajan YR (2004) Microwave assisted solid state reaction synthesis of $MgAl_2O_4$ spinel powders. J Eur Ceram Soc 24:201–207
63. Zhan W, Wang ZF, Zhang BB, Wang XT (2009) $MgAl_2O_4$ spinel synthesized by solid state reaction at low-heating temperature. Rare Metal Mater Eng 38:34–37
64. Zargar HR, Bayati MR, Rezaie HR, Golestani-Fard F, Molaei R, Zanganeh S et al (2010) Influence of nano boehmite on solid state reaction of alumina and magnesia. J Alloy Compd 507:443–447
65. Su XH, Li JG, Zhou ZJ (2012) Solid-state reaction preparation and sintering behavior of $MgAl_2O_4$ nanopowders. J Inorg Mater 27:991–996
66. Wang ZF, Liu H, Wang XT, Zhan W (2013) Sintering behavior of $MgAl_2O_4$ spinel powders prepared by solid state reaction at low temperature. Rare Metal Mater Eng 42:670–672
67. Wang NL, Zhang XY, Jiang HT, Dong TT, Yang D (2012) Fabrication of Er^{3+}/Yb^{3+} co-doped Y_2O_3 transparent ceramics by solid-state reaction method and its up-conversion luminescence. Mater Chem Phys 135:709–713
68. Yuan XY, Zhang F, Liu XJ, Zhang Z, Wang SW (2011) Fabrication of transparent AlON ceramics by solid-state reaction sintering. J Inorg Mater 26:499–502
69. Yuan XY, Liu XJ, Zhang F, Wang SW (2010) Synthesis of γ-AlON powders by a combinational method of carbothermal reduction and solid-state reaction. J Am Ceram Soc 93:22–24
70. Liu BL, Li J, Ivanov M, Liu WB, Liu J, Xie TF et al (2014) Solid-state reactive sintering of Nd:YAG transparent ceramics: the effect of Y_2O_3 powders pretreatment. Opt Mater 36:1591–1597
71. Kong LB, Zhang TS, Ma J, Boey F (2008) Progress in synthesis of ferroelectric ceramic materials via high-energy mechanochemical technique. Prog Mater Sci 53:207–322
72. Sepelak V, Duevel A, Wilkening M, Becker K-D, Heitjans P (2013) Mechanochemical reactions and syntheses of oxides. Chem Soc Rev 42:7507–7520
73. Fang F, Zhu M (2002) Mechanical alloying in immiscible alloy systems. Prog Nat Sci 12:170–174
74. Murty BS, Ranganathan S (1998) Novel materials synthesis by mechanical alloying/milling. Int Mater Rev 43:101–141
75. Ruiz-Navas EM, da Costa CE, Lopez FV, Castello JMT (2000) Mechanical alloying: a method to obtain metallic powders and composite materials. Rev De Metal 36:279–286
76. Suryanarayana C (2001) Mechanical alloying and milling. Prog Mater Sci 46:1–184
77. Cheng L, Liu P, Qu SX, Cheng L, Zhang HW (2015) Microwave dielectric properties of Mg_2TiO_4 ceramics synthesized via high energy ball milling method. J Alloy Compd 623:238–242
78. Bafrooei HB, Ebadzadeh T (2013) $MgAl_2O_4$ nanopowder synthesis by microwave assisted high energy ball-milling. Ceram Int 39:8933–8940
79. Cedeno-Mattei Y, Perales-Perez O, Uwakweh ONC (2013) Effect of high-energy ball milling time on structural and magnetic properties of nanocrystalline cobalt ferrite powders. J Magn Magn Mater 341:17–24
80. Zakeri M, Rahimipour MR, Abbasi BJ (2013) Synthesis of nanostructure tetragonal ZrO_2 by high energy ball milling. Mater Technol 28:181–186
81. Aguilar-Garib JA, Sanchez-de-Jesus F, Bolarin-Miro AM, Ham-Hernandez S (2011) Synthesis of $NiMn_2O_4$ assisted by high-energy ball milling of NiO-MnO powders. J Ceram Process Res 12:721–726
82. Sepelak V, Begin-Colin S, Le Caer G (2012) Transformations in oxides induced by high-energy ball-milling. Dalton Trans 41:11927–11948
83. Kong LB, Zhang TS, Ma J, Boey FYC (2007) Anisotropic grain growth in mullite powders as a result of high-energy ball milling. J Am Ceram Soc 90:4055–4058
84. Parashar SKS, Choudhary RNP, Murty BS (2005) Size effect of $Pb_{0.92}Nd_{0.08}(Zr_{0.53}Ti_{0.47})_{0.98}O_3$ nanoceramic synthesized by high-energy ball milling. J Appl Phys 98:104305

85. Kong LB, Ma J, Huang H, Zhang TS, Boey F (2003) Anisotropic mullitization in CuO-doped oxide mixture activated by high-energy ball milling. Mater Lett 57:3660–3666
86. Kong LB, Zhang TS, Ma J, Boey F (2003) Anisotropic grain growth of mullite in high-energy ball milled powders doped with transition metal oxides. J Eur Ceram Soc 23:2247–2256
87. Meitl MA, Dellinger TM, Braun PV (2003) Bismuth-ceramic nanocomposites with unusual thermal stability via high-energy ball milling. Adv Funct Mater 13:795–799
88. Kong LB, Ma J, Zhu W, Tan OK (2002) Transparent PLZT8/65/35 ceramics from constituent oxides mechanically modified by high-energy ball milling. J Mater Sci Lett 21:197–199
89. Kong LB, Ma J, Zhu W, Tan OK (2002) Translucent PMN and PMN-PT ceramics from high-energy ball milling derived powders. Mater Res Bull 37:23–32
90. Kong LB, Ma J, Zhu W, Tan OK (2001) Preparation and characterization of translucent PLZT8/65/35 ceramics from nano-sized powders produced by a high-energy ball-milling process. Mater Res Bull 36:1675–1685
91. Kong LB, Ma J, Huang HT, Zhu W, Tan OK (2001) Lead zirconate titanate ceramics derived from oxide mixture treated by a high-energy ball milling process. Mater Lett 50:129–133
92. Kong LB, Ma J, Zhang RF, Zhang TS (2002) Fabrication and characterization of lead lanthanum zirconate titanate (PLZT7/60/40) ceramics from oxides. J Alloy Compd 339:167–174
93. Kong LB, Ma J, Zhu W, Tan OK (2001) Preparation and characterization of PLZT ceramics using high-energy ball milling. J Alloy Compd 322:290–297
94. Chen IW, Wang XH (2000) Sintering dense nanocrystalline ceramics without final-stage grain growth. Nature 404:168–171
95. Zhang QW, Saito F (2003) Mechanochemical solid reaction of yttrium oxide alumina leading to the synthesis of yttrium aluminum garnet. Powder Technol 129:86–91
96. Huang H, Gong H, Tang D, Tan OK (2009) Synthesis and characterization of yttrium aluminum garnet by high-energy ball milling. Opt Mater 31:716–719
97. Kim W, Baker C, Villalobos G, Frantz J, Shaw B, Sadowski B et al (2014) Highly transparent ceramics obtained from jet milled sesquioxide powders synthesized by co-precipitation method. Optical Mater Express 4:2497–2503
98. An LQ, Ito A, Goto T (2011) Effects of ball milling and post-annealing on the transparency of spark plasma sintered Lu_2O_3. Ceram Int 37:2263–2267
99. Liu J, Lin L, Li J, Liu J, Yuan Y, Ivanov M et al (2014) Effects of ball milling time on microstructure evolution and optical transparency of Nd:YAG ceramics. Ceram Int 40:9841–9851
100. Chen XT, Lu TC, Wei N, Lu ZW, Zhang W, Ma BY et al (2014) Effect of ball-milling granulation with PVB adhesive on the sinterability of co-precipitated Yb:YAG nanopowders. J Alloy Compd 589:448–454
101. Wang J, Zhang J, Luo DW, Yang H, Tang DY, Kong LB (2015) Densification and microstructural evolution of yttria transparent ceramics: the effect of ball milling conditions. J Eur Ceram Soc 35:1011–1019
102. Wilhelmy RB, Patel RC, Matijevic E (1985) Thermodynamics and kinetics of aqueous ferric phosphate complex-formation. Inorg Chem 24:3290–3297
103. Matijevic E, Simpson CM, Amin N, Arajs S (1986) Preparation and magnetic properties of well-defined colloidal chromium ferrites. Colloids Surf 21:101–108
104. Haruta M, Lemaitre J, Delannay F, Delmon B (1984) Preparation and properties of colloidal spherical particles of molybdenum and cobal sulfides. J Colloid Interface Sci 101:59–71
105. Overbeek JTG (1977) Recent developments in understanding of colloid stability. J Colloid Interface Sci 58:408–422
106. Overbeek JTG (1982) Mondisperse colloidal systems, fascinating and useful. Adv Colloid Interface Sci 15:251–277
107. Overbeek JTG (1984) Interparticle forces in colloid science. Powder Technol 37:195–208

108. McDonald JE (1962) Homogeneous nucleation of vapor condensation, 1, thermodynamic aspects. Am J Phys 30:870–876
109. McDonald JE (1963) Homogeneous nucleation of vapor condensation, 2. Kinetic aspects. Am J Phys 31:31–41
110. Atkins P, de Paula J (2006) Physical chemistry, 8th edn. Oxford University Press, Oxford
111. Lamer VK, Dinegar RH (1950) Theory, production and mechanism of formation of monodispersed hydrosols. J Am Chem Soc 72:4847–4854
112. Christian JW (1975) The theory of transformations in metals and alloys: pergamon. Oxford
113. Wood GR, Walton AG (1970) Homogeneous nucleation kinetics of ice from water. J Appl Phys 41:3027–3036
114. Hodgson AW (1984) Homogeneous nucleation. Adv Colloid Interface Sci 21:303–327
115. Oxtoby DW (1992) Homogeneous nucleation—theory and experiment. J Phys-Condens Matter 4:7627–7650
116. Roldugin VI (2000) Homogeneous nucleation theory. Russ J Phys Chem 74:S522–S532
117. Holmes HF, Mesmer RE (1986) Thermodynamics of aqueous solutions of alkali-metal sulfates. J Solution Chem 15:495–518
118. Wesolowski D, Drummond SE, Mesmer RE, Ohmoto H (1984) Hydrolysis equilibria of tungsetn (VI) in aqueous sodium chloride solutions to 300 °C. Inorg Chem 23:1120–1132
119. Reiss H (1951) The growth of uniform colloidal dispersions. J Chem Phys 19:482–487
120. Nielsen AE (1957) Nucleation in barium sulfate precipitation. Acta Chem Scand 11:1512–1515
121. Nielsen AE (1958) The kinetics of crystal growth in barium sulfate precipitation. Acta Chem Scand 12:951–958
122. Nielsen AE (1959) The kinetics of crystal growth in barium sulfate precipitation, 2. Temperature dependence and mechanism. Acta Chem Scand 13:784–802
123. Nielsen AE (1959) The kinetics of crystal growth in barium sulfate precipitation, 3. Mixed surface reaction and diffusion controlled rate of growth. Acta Chem Scand 13:1680–1686
124. Nielsen AE, Bindra PS (1973) Effect of curvature on interfacial tension in liquid systems measured by homogeneous nucleation. Croat Chem Acta 45:31–52
125. Smellie RH, Lamer VK (1954) The electrokinetic properties of dilute monodisperse sufur hydrosols. J Phys Chem 58:583–591
126. Zaiser EM, Lamer VK (1948) The kinetics of the formation and growth of monodispersed sulfur hydrosols. J Colloid Sci 3:571–598
127. Matijevic E, Hsu WP (1987) Preparation and properties of monodispersed colloidal particles of lanthanide compounds, 1. Gadolinium, europium, terbium, samarium and cerium (III). J Colloid Interface Sci 118:506–523
128. Hsu WP, Matijevic E (1985) Optical properties of monodispersed hetatite hydrosols. Appl Opt 24:1623–1630
129. Bogush GH, Zukoski CF (1991) Uniform silica particle precipitation—an aggregative growth model. J Colloid Interface Sci 142:19–34
130. Sugimoto T (1987) Preparation of monodispersed colloidal particles. Adv Colloid Interface Sci 28:65–108
131. Park J, Privman V, Matijevic E (2001) Model of formation of monodispersed colloids. J Phys Chem B. 105:11630–11635
132. Matijevic E (1993) Preparation and properties of uniform size colloids. Chem Mater 5:412–426
133. Enomoto Y, Kawasaki K, Tokuyama M (1987) The time-dependent behavior of the Ostwald ripening for the finite volume fraction. Acta Metall 35:915–922
134. Marqusee JA, Ross J (1984) Theory of Ostwald ripening—competitive growth and its dependence on volume fraction. J Chem Phys 80:536–543
135. Jain SC, Hughes AE (1978) Ostwald ripening and its application to precipitates and colloids in ionic crystals and glasses. J Mater Sci 13:1611–1631
136. Kabalnov A (2001) Ostwald ripening and related phenomena. J Dispersion Sci Technol 22:1–12

137. Vengrenovitch RD (1982) On the Ostwald ripening theory. Acta Metall 30:1079–1086
138. Chen JY, Shi Y, Shi JL (2004) Synthesis of (Y, Gd)2O3: Eu nanopowder by a novel co-precipitation processing. J Mater Res 19:3586–3591
139. Chen JY, Shi Y, Shi JL (2004) Preparation and luminescence property of (Y, Gd)2O3: Eu nanopowder by complex precipitation. J Inorg Mater 19:1260–1266
140. Gong H, Tang DY, Huang H, Ma J (2009) Fabrication of yttrium aluminum garnet transparent ceramics from yttria nanopowders synthesized by carbonate precipitation. J Electroceram 23:89–93
141. Gong H, Tang DY, Huang H, Zhang TS, Ma J (2008) Effect of grain size on the sinterability of yttria nanopowders synthesized by carbonate-precipitation process. Mater Chem Phys 112:423–426
142. Huang Z, Guo W, Fei BJ, Li JT, Cao YG (2013) Influence of sulphate on synthesis of Nd: Y_2O_3 powders via coprecipitation route and fabrication of transparent ceramics. Mater Res Innovations 17:73–79
143. Huang ZG, Sun XD, Xiu ZM, Chen SW, Tsai CT (2004) Precipitation synthesis and sintering of yttria nanopowders. Mater Lett 58:2137–2142
144. Luo JM, Li YX, Deng LP (2008) Synthesis of Yb^{3+}:Y_2O_3 nanocrystalline by co-precipitation method and the properties of transparent ceramics. Chin J Inorg Chem 24:260–264
145. Wang NL, Zhang XY, Bai ZH, Liu QS, Lu LP, Mi XY et al (2010) Carbonate-precipitation synthesis of Yb^{3+}:Y_2O_3 nanopowders and its characteristics. Powder Technol 203:458–461
146. Wang PH, Wang NL, Zhang XY (2012) Carbonate co-precipitation synthesis of Lu_2O_3:Er^{3+} nano-powders and its property characterization. Chin J Inorg Chem 28:2335–2340
147. Ghanizadeh S, Bao X, Vaidhyanathan B, Binner J (2014) Synthesis of nano α-alumina powders using hydrothermal and precipitation routes: a comparative study. Ceram Int 40:1311–1319
148. Kong J, Chao B, Wang T, Yan Y (2012) Preparation of ultrafine spherical AlOOH and Al_2O_3 powders by aqueous precipitation method with mixed surfactants. Powder Technol 229:7–16
149. Hassanzadeh-Tabrizi SA, Taheri-Nassaj E (2009) Economical synthesis of Al_2O_3 nanopowder using a precipitation method. Mater Lett 63:2274–2276
150. Du X, Zhao S, Liu Y, Li J, Chen W, Cui Y (2014) Facile synthesis of monodisperse alpha-alumina nanoparticles via an isolation-medium-assisted calcination method. Appl Phys A-Mater Sci Process 116:1963–1969
151. Shen L, Hu C, Sakka Y, Huang Q (2012) Study of phase transformation behaviour of alumina through precipitation method. J Phys D-Appl Phys 45:215302
152. Zamorategui A, Sugita S, Zarraga R, Tanaka S, Uematsu K (2012) Evaluation of dispersability of gamma alumina prepared by homogeneous precipitation. J Ceram Soc Jpn 120:290–294
153. Wang W, Qiao X, Chen J (2008) The role of acetic acid in magnesium oxide preparation via chemical precipitation. J Am Ceram Soc 91:1697–1699
154. Yan C, Xue D, Zou L (2006) Fabrication of hexagonal MgO and its precursors by a homogeneous precipitation method. Mater Res Bull 41:2341–2348
155. Guo M, Li Q, Ye X, Wu Z (2010) Magnesium carbonate precipitation under the influence of polyacrylamide. Powder Technol 200:46–51
156. Camtakan Z, Erenturk S, Yusan S (2012) Magnesium oxide nanoparticles: Preparation, characterization, and uranium sorption properties. Environ Progr Sustain Energy 31:536–543
157. Li JG, Sun XD (2000) Synthesis and sintering behavior of a nanocrystalline alpha-alumina powder. Acta Mater 48:3103–3112
158. Su X, Chen S, Zhou Z (2012) Synthesis and characterization of monodisperse porous α-Al_2O_3 nanoparticles. Appl Surf Sci 258:5712–5715
159. Sohn S, Kwon Y, Kim Y, Kim D (2004) Synthesis and characterization of near-monodisperse yttria particles by homogeneous precipitation method. Powder Technol 142:136–153

160. Arabgari S, Malekfar R, Motamedi K (2011) Parameters effects on the surface morphology and structure of Nd:YAG nanopowders synthesized by co-precipitation method. J Nanopart Res 13:597–611
161. Guo W, Lu TC, Tong SH (2007) Effect of phase of YAG powder synthesized by co-precipitation on transparent ceramic sintering. In: Pan W, Gong JH (eds) High-performance ceramics IV, Pts 1-3. Trans Tech Publications Ltd, Stafa-Zurich, pp 2054–2057
162. Ji XB, Deng JG, Kang B, Huang H, Wang X, Jing W et al (2013) Thermal decomposition of $Y_3Al_5O_{12}$ precursor synthesized by urea homogeneous co-precipitation. Js Anal Appl Pyrol 104:361–365
163. Jiang FH, Zhao DG, Wang JQ (2013) Synthesis of YAG nano-powders and transparent ceramic by microwave homogeneous precipitation. Asian J Chem 25:5487–5489
164. Li HL, Liu XJ, Xie RJ, Zeng Y, Huang LP (2006) Fabrication of transparent cerium-doped lutetium aluminum garnet ceramics by co-precipitation routes. J Am Ceram Soc 89:2356–2358
165. Li HL, Liu XJ, Xie RJ, Zhou GH, Hirosaki N, Pu XP et al (2008) Cerium-doped lutetium aluminum garnet phosphors and optically transparent ceramics prepared from powder precursors by a urea homogeneous precipitation method. Jpn J Appl Phys 47:1657–1661
166. Li J, Chen F, Liu WB, Zhang WX, Wang L, Ba XW et al (2012) Co-precipitation synthesis route to yttrium aluminum garnet (YAG) transparent ceramics. J Eur Ceram Soc 32:2971–2979
167. Li XX, Zheng BY, Odoom-Wubah T, Huang JL (2013) Co-precipitation synthesis and two-step sintering of YAG powders for transparent ceramics. Ceram Int 39:7983–7988
168. Liu JH, Piao XQ, Cui HX, Guan XX, Li JL (2003) Preparation of Yb:YAG transparent laser ceramics with urea co-precipitation method. J Rare Earths 21:113–116
169. Marlot C, Barraud E, Le Gallet S, Eichhorn M, Bernard F (2012) Synthesis of YAG nanopowder by the co-precipitation method: Influence of pH and study of the reaction mechanisms. J Solid State Chem 191:114–120
170. Serantoni M, Costa AL, Zanelli C, Esposito L (2014) Crystallization behaviour of Yb-doped and undoped YAG nanoceramics synthesized by microwave-assisted urea precipitation. Ceram Int 40:11837–11844
171. You YL, Qi LH, Li XL, Pan W (2013) Preparation of YAG nano-powders via an ultrasonic spray co-precipitation method. Ceram Int 39:3987–3992
172. Wang L, Kou HM, Zeng YP, Li J, Pan YB, Guo JK (2012) Preparation of YAG powders and ceramics through mixed precipitation method. Ceram Int 38:4401–4405
173. Su CH, Zhang HS, Hui H, Qiong S, Hu HD, Zhang HB et al (2005) Preparation of neodymium-doped yttrium aluminum garnet transparent ceramics by homogeneous precipitation method. J Rare Earths 23:716–720
174. Li JG, Ikegami T, Lee JH, Mori T, Yajima Y (2001) A wet-chemical process yielding reactive magnesium aluminate spinel ($MgAl_2O_4$) powder. Ceram Int 27:481–489
175. Li JG, Ikegami T, Lee JH, Mori T, Yajima Y (2001) Synthesis of Mg-Al spinel powder via precipitation using ammonium bicarbonate as the precipitant. J Eur Ceram Soc 21:139–148
176. Lv GZ, Li XD, Di H, Sun XD, Chen SW, Tsai CT et al (2008) Fabrication of transparent YAG ceramics from co-precipitation synthesized nanopowders. In: Hu X, Fillery B, Qasim T, Duan K (eds) Structural integrity and failure. Trans Tech Publications Ltd, Stafa-Zurich, pp 271–276
177. Huang YH, Jiang DL, Zhang JX, Lin QL (2009) Precipitation synthesis and sintering of lanthanum doped yttria transparent ceramics. Opt Mater 31:1448–1453
178. Kriechbaum GW, Kleinschmit P (1989) Superfine oxide powders—flame hydrolysis and hydrothermal synthesis. Angewandte Chemie-Int Ed Engl 28:1416–1423
179. Sahraneshin A, Takami S, Minami K, Hojo D, Arita T, Adschiri T (2012) Synthesis and morphology control of surface functionalized nanoscale yttrium aluminum garnet particles via supercritical hydrothermal method. Prog Cryst Growth Charact Mater 58:43–50

180. Yang Q, Lu Z, Liu J, Lei X, Chang Z, Luo L et al (2013) Metal oxide and hydroxide nanoarrays: Hydrothermal synthesis and applications as supercapacitors and nanocatalysts. Prog Nat Sci-Mater Int 23:351–366
181. Ahn KH, Lee Y-H, Kim M, H-s Lee, Youn Y-S, Kim J et al (2013) Effects of surface area of titanium dioxide precursors on the hydrothermal synthesis of barium titanate by dissolution-precipitation. Ind Eng Chem Res 52:13370–13376
182. Avila HA, Ramajo LA, Reboredo MM, Castro MS, Parra R (2011) Hydrothermal synthesis of $BaTiO_3$ from different Ti-precursors and microstructural and electrical properties of sintered samples with submicrometric grain size. Ceram Int 37:2383–2390
183. Han J-M, Joung M-R, Kim J-S, Lee Y-S, Nahm S, Choi Y-K et al (2014) Hydrothermal synthesis of $BaTiO_3$ nanopowders using TiO_2 nanoparticles. J Am Ceram Soc 97:346–349
184. Kaur J, Kotnala RK, Verma KC (2012) Surfactant free hydrothermal synthesis, electrical, optical and ferroelectric properties of $BaTiO_3$ nanoparticles. J Optoelectron Adv Mater 14:219–223
185. Ozen M, Mertens M, Luyten J, Snijkers F, D'Hondt H, Cool P (2012) Hydrothermal synthesis of carbonate-free submicron-sized barium titanate from an amorphous precursor: synthesis and characterization. Ceram Int 38:619–625
186. Wang W, Cao L, Liu W, Su G, Zhang W (2013) Low-temperature synthesis of $BaTiO_3$ powders by the sol-gel-hydrothermal method. Ceram Int 39:7127–7134
187. Eckert JO, HungHouston CC, Gersten BL, Lencka MM, Riman RE (1996) Kinetics and mechanisms of hydrothermal synthesis of barium titanate. J Am Ceram Soc 79:2929–2939
188. Suchanek WL (2010) Hydrothermal synthesis of α-alumina (α-Al_2O_3) powders: study of the processing variables and growth mechanisms. J Am Ceram Soc 93:399–412
189. Mancic L, Lojpur V, Marinkovic BA, Dramicanin MD, Milosevic O (2013) Hydrothermal synthesis of nanostructured Y_2O_3 and $(Y_{0.75}Gd_{0.25})_2O_3$ based phosphors. Opt Mater 35:1817–1823
190. Huang BT, Ma YQ, Qian SB, Zou D, Zheng GH, Dai ZX (2014) Luminescent properties of low-temperature-hydrothermally-synthesized and post-treated YAG: Ce (5 %) phosphors. Opt Mater 36:1561–1565
191. Moore CA, McMillen CD, Kolis JW (2013) Hydrothermal growth of single crystals of $Lu_3Al_5O_{12}$ (LuAG) and its doped analogues. Cryst Growth Des 13:2298–2306
192. Qian S, Ma Y, Zan F, Zou D, Dai Z, Zheng G et al (2013) Fine YAG:Ce^{3+} nanoparticles synthesised by supercritical hydrothermal reaction. Micro Nano Lett 8:201–205
193. Garg A, Matijevic E (1988) Preparation and properties of uniformly coated inorganic colloidal particles, 3. Zirconium hydrous oxide on hematite. J Colloid Interface Sci 126:243–250
194. Garg A, Matijevic E (1988) Preparation and properties of uniformly coated inorganic colloidal particles, 2. Chromium hydrous oxide on hematite. Langmuir 4:38–44
195. Kratohvil S, Matijevic E (1987) Prepration and properties of coated, uniform, inorganic colloidal particles, 1. Aluminum (hydrous) oxide on hematite, chromia and titania. Adv Ceram Mater 2:798–803
196. Ocana M, Hsu WP, Matijevic E (1991) Preparation and properties of uniform-coated colloidal particles, 6. Titania Zinc-oxide. Langmuir 7:2911–2916
197. Garg AK, Dejonghe LC (1990) Microencapsulation of silicon-nitride particles with yttria and yttria-alumina precursors. J Mater Res 5:136–142
198. Okamura H, Barringer EA, Bowen HK (1986) Preparation and sintering of monosized Al_2O_3-TiO_2 composite powder. J Am Ceram Soc 69:C22–C24
199. Okamura H, Barringer EA, Bowen HK (1989) Preparation and sintering of narrow-sized Al_2O_3-TiO_2 composite powders. J Mater Sci 24:1867–1880
200. Garg AK, Dejonghe LC (1993) Metal-coated colloidal particles. J Mater Sci 28:3427–3432
201. Rahaman MN, Dejonghe LC (1991) Sintering of ceramic particlulate composites—effect of matrix density. J Am Ceram Soc 74:433–436
202. Aiken B, Hsu WP, Matijevic E (1990) Preparation and properties of uniform mixed and coated colloidal particles, 5. Zirconium compounds. J Mater Sci 25:1886–1894

203. Aiken B, Matijevic E (1988) Preparation and properties of uniform coated inorganic colloidal particles, 4. Yttrium basic carbonate and yttrium-oxide on hematite. J Colloid Interface Sci 126:645–649
204. Hu CL, Rahaman MN (1992) Factors controlling the sintering of ceramic particulate composites, 2. Coated inclusion particles. J Am Ceram Soc 75:2066–2070
205. Hu CL, Rahaman MN (1994) Dense Al_2O_3/ZrO_2 particulate composites by free sintering of coated powders. J Am Ceram Soc 77:815–819
206. Gherardi P, Matijevic E (1986) Interactions of precipitated hematite with preformed colloidal titania dispersions. J Colloid Interface Sci 109:57–68
207. Giesche H, Matijevic E (1994) Preparation, characterization and sinterability of well-defined silica/yttria powders. J Mater Res 9:436–450
208. Sang YH, Qin HM, Liu H, Zhao LL, Wang YN, Jiang HD et al (2013) Partial wet route for YAG powders synthesis leading to transparent ceramic: a core-shell solid-state reaction process. J Eur Ceram Soc 33:2617–2623
209. Mezhericher M, Levy A, Borde I (2015) Multi-scale multiphase modeling of transport phenomena in spray-drying processes. Drying Technol 33:2–23
210. Nandiyanto ABD, Okuyama K (2011) Progress in developing spray-drying methods for the production of controlled morphology particles: from the nanometer to submicrometer size ranges. Adv Powder Technol 22:1–19
211. Okuyama K, Abdullah M, Lenggoro IW, Iskandar F (2006) Preparation of functional nanostructured particles by spray drying. Adv Powder Technol 17:587–611
212. Hein JC, Rafflenbeul R, Beckmann M (1982) Progress in the technology of spray drying. Chem Ing Tech 54:787–792
213. Melnyk IV, Zub YL, Veron E, Massiot D, Cacciaguerra T, Alonso B (2008) Spray-dried mesoporous silica microspheres with adjustable textures and pore surfaces homogenously covered by accessible thiol functions. J Mater Chem 18:1368–1382
214. Pilarska A, Markiewicz E, Ciesielczyk F, Jesionowski T (2011) The influence of spray drying on the dispersive and physicochemical properties of magnesium oxide. Drying Technol 29:1210–1218
215. Serantoni M, Piancastelli A, Costa AL, Esposito L (2012) Improvements in the production of Yb:YAG transparent ceramic materials: Spray drying optimisation. Opt Mater 34:995–1001
216. Cho JS, Jung KY, Son MY, Kang YC (2014) Large-scale production of spherical $Y_2O_3:Eu^{3+}$ phosphor powders with narrow size distribution using a two-step spray drying method. Rsc Adv 4:62965–62970
217. Jung DS, Bin Park S, Kang YC (2010) Design of particles by spray pyrolysis and recent progress in its application. Korean J Chem Eng 27:1621–1645
218. Patil PS (1999) Versatility of chemical spray pyrolysis technique. Mater Chem Phys 59:185–198
219. Han JM, Jung DS, Lee SH, Kang YC (2008) Nano-sized MgO particles ranging from 13 to 28 nm synthesized by spray pyrolysis. J Ceram Process Res 9:140–145
220. Sohn JR, Kang YC, Park HD (2002) Morphological control of Y_2O_3:Eu phosphor particles by adding polymeric precursors in spray pyrolysis. Jpn J Appl Phys Part 1-Regul Papers Short Notes Rev Papers 41:3006–9
221. Marchal J, John T, Baranwal R, Hinklin T, Laine RM (2004) Yttrium aluminum garnet nanopowders produced by liquid-feed flame spray pyrolysis (LF-FSP) of metalloorganic precursors. Chem Mater 16:822–831
222. Nyman M, Caruso J, HampdenSmith MJ (1997) Comparison of solid-state and spray-pyrolysis synthesis of yttrium aluminate powders. J Am Ceram Soc 80:1231–1238
223. Mooney JB, Radding SB (1982) Spray pyrolysis processing. Annu Rev Mater Sci 12:81–101
224. Messing GL, Zhang SC, Jayanthi GV (1993) Ceramic powder synthesis by spray-pyrolysis. J Am Ceram Soc 76:2707–2726
225. Zhang SC, Messing GL, Borden M (1990) Synthesis of solid, spherical zirconia particles by spray pyrolysis. J Am Ceram Soc 73:61–67

226. Jung KY, Lee DY, Kang YC (2005) Morphology control and luminescent property of Y3Al5O12: Tb particles prepared by spray pyrolysis. Mater Res Bull 40:2212–2218
227. Jung KY, Lee HW (2007) Enhanced luminescent properties of $Y_3Al_5O_{12}$:Tb^{3+}, Ce^{3+} phosphor prepared by spray pyrolysis. J Lumin 126:469–474
228. Lee SH, Jung DS, Han JM, Koo HY, Kang YC (2009) Fine-sized $Y_3Al_5O_{12}$: Ce phosphor powders prepared by spray pyrolysis from the spray solution with barium fluoride flux. J Alloy Compd 477:776–779
229. Lee SH, Koo HY, Lee SM, Kang YC (2010) Characteristics of $Y_3Al_5O_{12}$: Ce phosphor powders prepared by spray pyrolysis from ethylenediaminetetraacetic acid solution. Ceram Int 36:611–615
230. Claussen IC, Ustad TS, Strommen I, Waide PM (2007) Atmospheric freeze drying—a review. Drying Technol 25:947–957
231. Geidobler R, Winter G (2013) Controlled ice nucleation in the field of freeze-drying: Fundamentals and technology review. Eur J Pharm Biopharm 85:214–222
232. Qian L, Zhang H (2011) Controlled freezing and freeze drying: a versatile route for porous and micro-/nano-structured materials. J Chem Technol Biotechnol 86:172–184
233. Tallon C, Moreno R, Nieto MI (2006) Synthesis of gamma-Al_2O_3 nanopowders by freeze-drying. Mater Res Bull 41:1520–1529
234. Huang Y-H, Jiang D-L, Zhang J-X, Lin Q-L (2008) Fabrication of transparent yttria ceramics through gel-freezing dry method. J Inorg Mater 23:1135–1140
235. Li RX, Yin S, Chen L, Yu KN, Li SH, Liang HZ et al (2003) Microstructure evolution of ZrO_2-(Al_2O_3, Fe_2O_3) materials synthesized by frozen-drying. J Inorg Mater 18:373–378
236. Tallon C, Moreno R (2009) Isabel Nieto M. Synthesis of ZrO_2 nanoparticles by freeze drying. Int J Appl Ceram Technol 6:324–334
237. Zhao Z, Chen D, Jiao X (2007) Zirconia aerogels with high surface area derived from sols prepared by electrolyzing zirconium oxychloride solution: Comparison of aerogels prepared by freeze-drying and supercritical CO_2(l) extraction. J Phys Chem C 111:18738–18743
238. Zhang X, Zhao HZ, Ma Q, Li XW, Wang HZ, Zhang WJ (2005) Preparation of spinel nano-powder with vacuum freeze drying. Rare Metal Mater Eng 34:78–81
239. McHale JM, Navrotsky A, Kirkpatrick RJ (1998) Nanocrystalline spinel from freeze-dried nitrates: Synthesis, energetics of produce formation, and cation distribution. Chem Mater 10:1083–1090
240. Tao CS, Pask JA (1973) Correlation of sintered spinel microstructure with characteristics of powder prepared by freeze-drying. Am Ceram Soc Bull 52:708
241. Wang CT, Lin LS, Yang SJ (1992) Preparation of $MgAl_2O_4$ spinel powders via freeze-drying of alkoxide precursors. J Am Ceram Soc 75:2240–2243
242. Rabinovitch Y, Bogicevic C, Karolak F, Tetard D, Dammak H (2008) Freeze-dried nanometric neodymium-doped YAG powders for transparent ceramics. J Mater Process Technol 199:314–320
243. Gong H, Tang DY, Huang H, Ma J (2009) Agglomeration control of Nd:YAG nanoparticles via freeze drying for transparent Nd:YAG ceramics. J Am Ceram Soc 92:812–817
244. Ding SQ, Zeng YP, Jiang DL (2007) Fabrication of mullite ceramics with ultrahigh porosity by gel freeze drying. J Am Ceram Soc 90:2276–2279
245. Fonseca AT, Vieira JM, Baptista JL (1986) Dependence of the densification on grain-growth and on agglomeration in sintering of dolomite. J De Physique 47:435–440
246. Kurajica S, Tkalcec E, Matijasic G, Curkovic L, Schauperl Z, Sipusic J et al (2011) Influence of agglomeration and contamination in the course of amorphous powder grinding on structure and microstructure of sintered mullite. Croat Chem Acta 84:63–71
247. Liu DM, Lin JT, Tuan WH (1999) Interdependence between green compact property and powder agglomeration and their relation to the sintering behaviour of zirconia powder. Ceram Int 25:551–559
248. Sacks MD, Pask JA (1982) Sintering of mullite-containing materials, 2. Effect of agglomeration. J Am Ceram Soc 65:70–77

249. Wang C, Chen S-H (2012) Factors influencing particle agglomeration during solid-state sintering. Acta Mech Sin 28:711–719
250. Zych L, Lach R, Wajler A (2014) The influence of the agglomeration state of nanometric $MgAl_2O_4$ powders on their consolidation and sintering. Ceram Int 40:9783–9790
251. Amato I, Baudrocco F, Martorana D (1976) Evaluation of freeze-drying and spray drying processes for preparing transparent alumina. Mater Sci Eng 26:73–78
252. Komarneni S (1996) Some significant advances in sol-gel processing of dense structural ceramics. J Sol-Gel Sci Technol 6:127–138
253. Li DY, Hui Y, Lian JS, Xie TT (2005) Progress in research on nanometer Al_2O_3 fabricated by sol-gel method. J Rare Earths 23:600–605
254. Shojaie-Bahaabad M, Taheri-Nassaj E, Naghizadeh R (2008) An alumina-YAG nanostructured fiber prepared from an aqueous sol-gel precursor: preparation, rheological behavior and spinnability. Ceram Int 34:1893–1902
255. Saha D, Mistry KK, Giri R, Guha A, Sensgupta K (2005) Dependence of moisture absorption property on sol-gel process of transparent nano-structured γ-Al_2O_3 ceramics. Sens Actuators B-Chem 109:363–366
256. Dupont A, Parent C, Le Garrec B, Heintz JM (2003) Size and morphology control of Y_2O_3 nanopowders via a sol-gel route. J Solid State Chem 171:152–160
257. Maia AS, Stefani R, Kodaira CA, Felinto MCFC, Teotonio EES, Brito HF (2008) Luminescent nanoparticles of $MgAl_2O_4$:Eu, Dy prepared by citrate sol-gel method. Opt Mater 31:440–444
258. Zhang HJ, Jia XL, Liu ZJ, Li ZZ (2004) The low temperature preparation of nanocrystalline $MgAl_2O_4$ spinel by citrate sol-gel process. Mater Lett 58:1625–1628
259. Gong H, Tang D-Y, Huang H, Han M-D, Sun T, Zhang J et al (2013) Crystallization kinetics and characterization of nanosized Nd:YAG by a modified sol-gel combustion process. J Cryst Growth 362:52–57
260. Guo K, Chen HH, Guo XX, Yang XX, Xu FF, Zhao JT (2010) Morphology investigation of yttrium aluminum garnet nano-powders prepared by a sol-gel combustion method. J Alloy Compd 500:34–38
261. Sun J, Zeng FM, Li JL, Cao YI, Wan YC, Liu JH (2005) Synthesis of Nd: GGG ultrafine polycrystalline powders by sol-gel method. J Rare Earths 23:188–190
262. Yu F, Yuan D, Cheng X, Duan X, Wang X, Kong L et al (2007) Preparation and characterization of yttrium gallium garnet nanoparticles by citrate sol-gel method at low temperature. Mater Lett 61:2322–2324
263. Liu XJ, Li HL, Xie RJ, Hirosaki N, Xu X, Huang LP (2006) Cerium-doped lutetium aluminum garnet optically transparent ceramics fabricated by a sol-gel combustion process. J Mater Res 21:1519–1525
264. Guo XZ, Li WY, Nakanishi K, Kanamori K, Zhu Y, Yang H (2013) Preparation of mullite monoliths with well-defined macropores and mesostructured skeletons via the sol-gel process accompanied by phase separation. J Eur Ceram Soc 33:1967–1974
265. Ivankovic H, Tkalcec E, Rein R, Schmidt H (2006) Microstructure and high temperature 4-point bending creep of sol-gel derived mullite ceramics. J Eur Ceram Soc 26:1637–1646
266. Jin XH, Gao L, Guo JK (2001) Preparation of mullite powders by sol-gel methods. J Inorg Mater 16:555–558
267. Leivo J, Linden M, Teixeira CV, Puputti J, Rosenholm J, Levanen E et al (2006) Sol-gel synthesis of a nanoparticulate aluminosilicate precursor for homogeneous mullite ceramics. J Mater Res 21:1279–1285
268. Moallemi-Nejad M, Heshmati-Manesh S (2008) Synthesis of nano-structured mullite by sol-gel method with intermediate mechanical activation. Int J Mod Phys B 22:2947–2954
269. Bhattacharyya D, Hazra C, Gangwar P, Sivakumar S, Mahalingam V (2012) Microstructural, optical and cytotoxicity studies of Eu^{3+}-doped Y_2O_3 nanoparticles prepared by simple control of the chain length of cross-linkers via pechini method. Sci Adv Mater 4:656–662
270. Hajizadeh-Oghaz M, Razavi RS, Estarki ML (2014) Large-scale synthesis of YSZ nanopowder by Pechini method. Bull Mater Sci 37:969–973

271. Kodaira CA, Stefani R, Maia AS, Felinto MCFC, Brito HF (2007) Optical investigation of Y_2O_3:Sm^{3+} nanophosphor prepared by combustion and Pechini methods. J Lumin 127:616–622
272. Majid A, Tunney J, Argue S, Kingston D, Post M, Margeson J et al (2010) Characterization of CuO phase in SnO_2–CuO prepared by the modified Pechini method. J Sol-Gel Sci Technol 53:390–398
273. Saengkerdsub S, Im HJ, Willis C, Dai S (2004) Pechini-type in-situ polymerizable complex (IPC) method applied to the synthesis of Y2O3: Ln (Ln = Ce or Eu) nanocrystallites. J Mater Chem 14:1207–1211
274. Soisuwan P, Chambers DC, Trimm DL, Mekasuwandumrong O, Panpranot J, Praserthdam P (2005) Characteristics and catalytic properties of alumina-zirconia mixed oxides prepared by a modified Pechini method. Catal Lett 103:63–68
275. Zhang YW, Wang JJ, Yan ZG, Yan CH (2004) Effects of synthetic parameters in pechini method on the formation and properties of $(ZrO_2)_{0.92}(Sc_2O_3)_{0.08}$ solid solution. J Rare Earths 22:475–482
276. Zhang K, Hu W, Li J, Tang Y, Liu H (2009) Matrix induced synthesis of Y3Al5O12: Ce phosphor through the Pechini method. Int J Mater Res 100:238–242
277. Galceran M, Pujol MC, Aguilo M, Diaz F (2008) Synthesis and characterization of nanocrystalline Yb:Lu_2O_3 by modified Pechini method. Mater Sci Eng B-Solid State Mater Adv Technol 146:7–15
278. Marin R, Sponchia G, Riello P, Sulcis R, Enrichi F (2012) Photoluminescence properties of YAG:Ce^{3+},Pr^{3+} phosphors synthesized via the Pechini method for white LEDs. J Nanoparticle Res 14:1–13
279. Back M, Boffelli M, Massari A, Marin R, Enrichi F, Riello P (2013) Energy transfer between Tb^{3+} and Eu^{3+} in co-doped Y_2O_3 nanocrystals prepared by Pechini method. J Nanoparticle Res 15:1–14
280. Wiglusz RJ, Grzyb T, Lis S, Strek W (2009) Preparation and spectroscopy characterization of Eu:$MgAl_2O_4$ nanopowder prepared by modified Pechini method. J Nanosci Nanotechnol 9:5803–5810
281. Courty P, Ajot H, Marcilly C, Delmon B (1973) Oxides, mixed or in slid-solution, highly dispersed obtained by thermal decomposition of amorphous precursors. Powder Technol 7:21–38
282. Marcilly C, Courty P, Delmon B (1970) Preparation of highly dispersed mixed oxides and oxide solid solutions by pyrolysis of amporphous orangic precursors. J Am Ceram Soc 53:56–57
283. Batoo KM (2011) Structural and electrical properties of Cu doped $NiFe_2O_4$ nanoparticles prepared through modified citrate gel method. J Phys Chem Solids 72:1400–1407
284. Xie G-Q, Lu J-Q, Zheng H-Y, Liu X-J, Luo M-F, Li X-N (2010) Effect of carbonization temperature on the textural properties of $Ce_{0.8}Zr_{0.2}O_2$ solid solution by an improved citrate sol-gel method. J Alloy Compd 493:169–174
285. Bao A, Tao CY, Yang H (2008) Luminescent properties of nanoparticles $LaSrAl_3O_7$:RE^{3+} (RE = Eu, Tb) via the citrate sol-gel method. J Mater Sci-Mater Electron 19:476–481
286. Kim KM, Ryu JH, Mhin SW, Park GS, Shim KB (2008) Luminescence of nanocrystalline $Tb_3Al_5O_{12}$:Ce^{3+} phosphors synthesized by nitrate-citrate gel combustion method. J Electrochem Soc 155:J293–J296
287. Soo MS, Joon YP, Byung JC (2003) Synthesis of yttrium aluminum garnet powder by citrate gel method. J Ceram Process Res 4:145–150
288. Li J, Pan Y, Qiu F, Wu Y, Guo J (2008) Nanostructured Nd:YAG powders via gel combustion: the influence of citrate-to-nitrate ratio. Ceram Int 34:141–149
289. Jia XL, Zhang HJ, Yan YJ, Liu ZJ (2004) Effect of the citrate sol-gel synthesis on the formation of $MgAl_2O_4$ ultrafine powder. Mater Sci Eng A-Struct Mater Prop Microstruct Process 379:112–118

290. Wang NL, Zhang XY, Bai ZH, Sun HY, Liu QS, Lu LP et al (2011) Synthesis of nanocrystalline ytterbium-doped yttria by citrate gel combustion method and fabrication of ceramic materials. Ceram Int 37:3133–3138
291. Birol H, Rambo CR, Guiotoku M, Hotza D (2013) Preparation of ceramic nanoparticles via cellulose-assisted glycine nitrate process: a review. Rsc Adv 3:2873–2884
292. Hajarpour S, Raouf AH, Gheisari K (2014) Structural evolution and magnetic properties of nanocrystalline magnesium- zinc soft ferrites synthesized by glycine-nitrate combustion process. J Magn Magn Mater 363:21–25
293. Valefi M, Falamaki C, Ebadzadeh T, Hashjin MS (2007) New insights of the glycine-nitrate process for the synthesis of nano-crystalline 8YSZ. J Am Ceram Soc 90:2008–2014
294. He TM, He Q, Wang N (2005) Synthesis of nano-sized YSZ powders from glycine-nitrate process and optimization of their properties. J Alloy Compd 396:309–315
295. Kim GD, Park JA, Lee HL, Lee DA, Moon JW, Kim JD (1999) Synthesis and sintering of $BaTiO_3$ powders by the glycine-nitrate process using metal carbonate and alkoxide. J Ceram Soc Jpn 107:691–696
296. Toniolo JC, Lima MD, Takimi AS, Bergmann CP (2005) Synthesis of alumina powders by the glycine-nitrate combustion process. Mater Res Bull 40:561–571
297. Wang Z, Yang B, Fu Z, Dong W, Yang Y, Liu W (2005) UV-blue photoluminescence from ZrO_2 nanopowders prepared via glycine nitrate process. Appl Phys a-Mater Sci Process 81:691–694
298. Komlev AA, Vilezhaninov EF (2013) Glycin-nitrate combustion synthesis of nanopowders based on nonstroichiometric magnesium–aluminum spinel. Russ J Appl Chem 86:1344–1350
299. Zhukov AV, Chizhevskaya SV, Klimenko OM, Merkushkin AO (2014) Glycine-nitrate synthesis of partially yttrium-stablized zirconium nanopowders for hard ceramics. Glass Ceram 70:400–403
300. Lei LW, Fu ZY, Wang H, Lee SW, Niihara K (2012) Transparent yttria stabilized zirconia from glycine-nitrate process by spark plasma sintering. Ceram Int 38:23–28
301. Durham BG, Murtha MJ, Burnet G (1988) Si_3N_4 by the carbothermal ammonolysis of silica. Adv Ceram Mater 3:45–48
302. Lin DC, Kimura S (1996) Kinetics of silicon monoxide ammonolysis for nanophase silicon nitride synthesis. J Am Ceram Soc 79:2947–2955
303. Ziegenbalg G, Breuel U, Ebrecht E, Holldorf H, Brink R (2001) Synthesis of alpha-silicon nitride powder by gas-phase ammonolysis of CH_3SiCl_3. J Eur Ceram Soc 21:947–958
304. Deng J, Su K, Wang X, Zeng Q, Cheng L, Xu Y et al (2009) Thermodynamics of the gas-phase reactions in chemical vapor deposition of silicon carbide with methyltrichlorosilane precursor. Theoret Chem Acc 122:1–22
305. Kim HI, Choi JM, Kim DJ, So MG (2002) Synthesis and crystallization of fine SiC-Si_3N_4 composite powders by a vapor phase reaction. J Ceram Process Res 3:82–85
306. Ning XG, Ye HQ, Liang Y, Zheng F (1992) Structural characterization of ultrafine SiC powder made from laser-heated vapor-phase reactions. J Mater Sci Lett 11:59–62
307. Moshtaghioun BM, Monshi A, Abbasi MH, Karimzadeh F (2011) A study on the effects of silica particle size and milling time on synthesis of silicon carbide nanoparticles by carbothermic reduction. Int J Refract Metal Hard Mater 29:645–650
308. Narisawa M, Okabe Y, Iguchi M, Okamura K (1998) Synthesis of ultrafine SiC powders from carbon-silica hybridized precursors with carbothermic reduction. J Sol-Gel Sci Technol 12:143–152
309. Bendovskii EB (2013) Silicon nitridation at different nitrogen pressures. Glass Ceram 69:324–329
310. Chung S-L, Chang C-W (2009) Carbothermal reduction and nitridation synthesis of silicon nitride by using solution combustion synthesized precursors. J Mater Sci 44:3784–3792
311. Hu HL, Zeng YP, Xia YF, Yao DX, Zuo KH (2014) High-strength porous Si_3N_4 ceramics prepared by freeze casting and silicon powder nitridation process. Mater Lett 133:285–288

312. Liu S, Ji H, Liang H, Ma Y (2008) Preparation of Si_3N_4 powders by the direct nitridation of silicon. Rare Metal Mater Eng 37:378–381
313. Yao DX, Zeng YP (2011) High flexural strength porous silicon nitride prepared via nitridation of silicon powder. J Inorg Mater 26:422–426
314. Yin S-w, Wang L, Tong L-g, Yang F-m, Li Y-h (2013) Kinetic study on the direct nitridation of silicon powders diluted with alpha-Si_3N_4 at normal pressure. Int J Miner Metallurgy Mater 20:493–498
315. Suri J, Shaw LL, Zawrah MF (2012) Tailoring the relative Si_3N_4 and SiC contents in Si_3N_4/SiC nanopowders through carbothermic reduction and nitridation of silica fume. Int J Appl Ceram Technol 9:291–303
316. Mazdiyas Ks, Cooke CM (1973) Synthesis, characterization and consolidation of Si_3N_4 obtained from ammonolysis of $SiCl_4$. J Am Ceram Soc 56:628–633
317. Rudin T, Wegner K, Pratsinis SE (2013) Towards carbon-free flame spray synthesis of homogeneous oxide nanoparticles from aqueous solutions. Adv Powder Technol 24:632–642
318. Yeh CL, Yeh SH, Ma HK (2004) Flame synthesis of titania particles from titanium tetraisopropoxide in premixed flames. Powder Technol 145:1–9
319. Yeh CL, Zhao E, Ma HK (2001) An experimental investigation of combustion synthesis of silicon dioxide (SiO_2) particles in premixed flames. Combust Sci Technol 173:25–46
320. Kathirvel P, Chandrasekaran J, Manoharan D, Kumar S (2014) Preparation and characterization of alpha alumina nanoparticles by in-flight oxidation of flame synthesis. J Alloy Compd 590:341–345
321. Tok AIY, Boey FYC, Zhao XL (2006) Novel synthesis of Al_2O_3 nano-particles by flame spray pyrolysis. J Mater Process Technol 178:270–273
322. Varatharajan K, Dash S, Arunkumar A, Nithya R, Tyagi AK, Raj B (2003) Synthesis of nanocrystalline α-Al_2O_3 by ultrasonic flame pyrolysis. Mater Res Bull 38:577–583
323. Baker C, Kim W, Sanghera J, Goswami R, Villalobos G, Sadowski B et al (2012) Flame spray synthesis of Lu_2O_3 nanoparticles. Mater Lett 66:132–134
324. Goldstein A, Goldenberg A, Yeshurun Y, Hefetz M (2008) Transparent $MgAl_2O_4$ spinel from a powder prepared by flame spray prolysis. J Am Ceram Soc 91:4141–4144
325. Laine RM, Marchal JC, Sun HP, Pan XQ (2006) Nano-α-Al_2O_3 by liquid-feed flame spray pyrolysis. Nat Mater 5:710–712
326. Teoh WY, Amal R, Maedler L (2010) Flame spray pyrolysis: an enabling technology for nanoparticles design and fabrication. Nanoscale. 2:1324–1347